Analysis and Design of Application Specific Optical Fibres

Thirtieth Anniversary Edition

A thesis submitted for the degree of
Doctor of Philosophy
in July 1994

by

Donald Glenn Geers

Department of Theoretical Physics
The University of Sydney
Australia

July 2024

ACKNOWLEDGEMENTS

I would like to thank my supervisor Dr I. M. Basset for his support and guidance throughout the course of the research described in this thesis. Dr J. G. Lewis of Boeing Computer Services in Seattle provided much valued discussion on techniques for solving the sparse generalized eigenproblem. Special thanks also to Drs K. S. Chiang, S. J. Hewlett and J. D. Love for useful discussions on some of the finer details of optical fibre theory.

The Theoretical Physics Department provided a pleasant environment in which to perform research and I would like to thank all its members, both staff and students, for making it so. In particular David Dawes provided answers to many obscure questions concerning programming in a UNIX environment. My room mate Kai Ming Lo, and Drs Leon Poladian and Peter Robinson also deserve special thanks for useful discussions at various stages of the work.

Thanks are also due to the staff and students of the Optical Fibre Technology Centre and to the many co-workers involved with the Siemens GIRD Project.

I thank the Australian Telecommunication and Electronic Research Board and the Australian Photonics Cooperative Research Centre for financial support throughout the course of the research described in this thesis.

Finally, I would like to thank my parents for their support and understanding throughout all my years as a student.

Preface to the Thirtieth Anniversary Edition

During the thirty years since I submitted my dissertation much has changed in the field of numerical analysis. Not the least of which has been the continuing growth of computer power. The computer on which I'm typing is two orders of magnitude faster than the Cray Y-MP/EL on which I did my calculations. And it supported a whole department!

Referencing has become a whole lot easier. I rechecked all my references and added them to Zotero (a free referencing tool) using the 'digital object identifier' (DOI) which uniquely, and permanently idetifies each online paper—way easier than when I had to go to a library and enter the details manually! Thankfully, all the publishing houses have agreed on a standard, and have digitised papers that are decades or even centuries old.

LaTeX has also evolved to include hyperlinks within documents and via the DOI, to references on publishers' web sites. I have updated my dissertation to include these features where available.

Some of the Technical Reports I originally cited are now published papers and this is reflected in the new Bibliography.

All book references are to the editions I used when working on my dissertation.

On a personal level, my thesis advisor Dr Ian Masson Bassett passed away on 27 August 2021. And my room mate, for part of my PhD, Dr Leon Poladian passed away on 13 February 2018.

Both of them had a large impact on my career.

D. Glenn Geers, December 2024

Contents

Thesis Abstract

This thesis is concerned with the analysis and design of application specific optical fibres, that is, optical fibres in which the geometry and chemical composition is dictated to a large extent by the sensing or communication application in which they are intended to be used.

In Chapter 1 an overview of waveguide analysis from an historical perspective is given and some background material on sparse matrix methods presented.

Chapters 2 and 3 contain details of new finite difference based methods to solve the scalar and vector wave equations respectively. The methods presented are two-dimensional and may be used to solve a wide range of optical fibre and dielectric waveguide problems in which the core has an essentially arbitrary geometry and refractive index distribution. Multiple core problems are catered for. The vector wave equation solver is able to compute the modes of anisotropic waveguides including off-diagonal elements in the permittivity tensor.

The later chapters are used to demonstrate the applicability of the solvers to novel problems of practical importance.

Chapter 4 presents design considerations for circularly birefringent optical fibres and a new design based on readily available fibre fabrication technology is described. Circularly birefringent fibres have immediate applications in communications and sensing.

Chapter 5 discusses twin-core optical fibre wavelength demultiplexers providing a detailed design tolerance and sensitivity analysis and the theoretical design is compared with experimental results.

In Chapter 6 some extensions to the material presented previously are examined. In particular an alternative formulation of the vector wave equation is discussed, the scalar solver is extended to the nonlinear regime and an observation concerning the form of the minor field component in real optical fibres is discussed. This last item has possible applications in optical fibre characterization.

List of Figures

List of Tables

Chapter 1

Overview

1.1 Background

Optical fibres tailored for specific applications are required both for communication and sensing systems. The ability to design application specific optical fibres (ASOFs) requires the use of computer modelling techniques because it is far too time consuming and economically infeasible to manufacture optical fibres with novel geometries or dopants without a reasonable level of confidence that the fibre will have the design properties. There is a plethora of numerical methods available for solving the wave equation in an optical fibre (a brief survey is given in Section 1.3) but in order to be usable as design tools they must be numerically robust, unambiguous in their predictions, efficient and, above all, applicable to the widest class of practical problems.

Physically, an optical fibre consists of one or more guiding core regions, in which the majority of the transmitted light nominally resides, of essentially arbitrary shape embedded in a cladding which is sufficiently large in extent that the electromagnetic fields at the cladding boundary may be assumed to be zero. The refractive index, n_{co}, of the core regions must be greater than that of the cladding, n_{cl}, in order for the light to remain bound. The fibre is assumed uniform along its length. From the practical point of view most fibres have one or two centrally placed cores of circular cross-section and are manufactured from silica (SiO_2) with dopant materials (e.g., germanium) introduced in order to raise or lower the refractive index appropriately.

An optical fibre may be characterised in terms of the parameter Δ given by

$$\Delta = \frac{n_{co}^2 - n_{cl}^2}{2n_{co}^2}. \tag{1.1}$$

The majority of commercially available fibres have a Δ parameter of order 1%

and are said to be 'weakly guiding' which is somewhat of a misnomer because the light propagating in the fibre is still tightly bound.

A standard communications fibre has an overall diameter of 125μm and has a single core of diameter less than 10μm. With these dimensions the fibre will have one or, at most, a few bound modes at the telecommunications wavelengths 1.3 and 1.55μm, where the transmission loss is typically of the order of 0.2dB/km.

1.2 Brief Historical Overview of Waveguide Analysis

The development of optical fibre and waveguide theory and practice has been extremely rapid over the last thirty-five years yet little comment is to be found on work carried out before that time. The enormous interest in all dielectric waveguides was of course triggered by the manufacture of extremely low loss dielectrics—high quality silica glass—in the late 1950's yet the original theoretical analysis predates this development considerably.

1.2.1 The Early Years: 1897–1941

In 1897 Lord Rayleigh laid down the fundamental theoretical groundwork for the case of perfectly conducting dielectric filled cylindrical waveguides of arbitrary cross-section and presented detailed solutions for the particular (and analytically soluble) cases of square and circular cross-sections [1]. He correctly identified the two classes of solution now known as the transverse electric (TE) and transverse magnetic (TM) modes as well as determining the cutoff wavelengths stating that

> 'If the actual frequency ... is much less than [cutoff], the resulting disturbance is practically limited to a neighbouring finite length of the cylinder.'

This effect is put to practical use in optical fibre mode strippers.

Thirteen years after Rayleigh's paper Hondros and Debye presented the theory of guidance by a 'dielectric wire' [2], i.e., a dielectric rod in vacuum. The theory is identical to that of a fibre in which the cladding index is unity.

Interestingly, the first observations of bound waveguide modes were reported for the case of a dielectric wire as early as 1916 [3] and expanded upon after the First World War by Schriever in 1920 [4]. The wavelengths used were in the 10's of centimetres.

A further fourteen years were to pass before waveguides appeared in the literature again. Bergmann and Krügel [5] reported that they had measured the fields

within a short hollow cylindrical metal waveguide. They also observed that the open end radiated quite efficiently into the surrounding medium.

The first papers in English since Rayleigh's appeared in the *Bell Systems Technical Journal* in 1936 when a theoretical paper by Carson, *et. al.* [6] and an experimental paper by Southworth [7] were published. These papers focused primarily on the hollow metallic cylinder (including finite conductivity effects) although there is a short theoretical discussion of the dielectric wire in [6] where it is pointed out that 'guided waves are possible only if the dielectric constant of the guide is higher than that of the surrounding medium'. The fact that the modes are hybrid (HE or EH in modern notation) was also pointed out.

A paper by Barrow also in 1936 [8] dealt with both theoretical and experimental aspects of the hollow metallic waveguide problem and this together with the two *Bell* papers ushered in the extreme interest in waveguides that has persisted to this day. In fact, by 1941, the theory was appearing in advanced textbooks on electromagnetism [9].

The review of the early development of waveguides is essentially complete. The small number of papers being primarily due to the difficulty of producing microwave radiation prior to the development of the cavity magnetron in 1939. Theoretical interest was also limited due to the lack of experimental drive.

1.2.2 Optical Fibres

The early experimental work was, of course, performed at very high radio frequencies but during the 1950's several papers (both experimental and theoretical) on optical fibres (as opposed to dielectric waveguides) appeared firstly in *Nature* [10, 11] and then in the more usual optics journals [12, 13, 14]. Van Heel [11] noted that:

> 'A much better result was obtained when the fibres were coated with a layer of lower refractive index, which ensured total reflexion'.

Interest at this early stage focused more on what today would be termed light pipes with the application being image transmission in endoscopes for example. By 1959, however, true optical fibres consisting of core and cladding were being widely discussed in the literature (see, for example, the abstracts of the Spring and Annual meetings of the Optical Society of America, 1959).

In 1961, Snitzer [15] presented the first theoretical analysis of the clad optical fibre, which can be viewed as a straightforward extension of the work of Hondros and Debye.

The invention of the laser in 1960 created great interest in the possibility of optical communication systems using optical fibre as the guiding medium and in

1970 the first of many special issue journals on optical communication systems appeared [16].

Snyder, in a classic paper [17], presented the simplification that is now known as the 'weak guidance' approximation. By realizing that an optical fibre usually consists of a core with refractive index only very slightly greater than that of the cladding he was able to reduce the vector wave equation to the scalar wave equation by an intricate perturbation analysis. Gloge [18] refined Snyder's analysis and recast it in a more usable form. Together, these two papers provide the stepping off point for modern optical fibre and dielectric waveguide analysis.

1.3 Numerical Solution of the Wave Equation

The ability to calculate modal properties of waveguiding structures of arbitrary core geometry and permittivity distribution requires the use of numerical techniques. Some progress can be made using perturbation theory but for truly useful design tools higher accuracy than can be easily obtained through approximation methods is required. A brief survey of some current methods is presented below although no attempt at completeness of coverage is attempted due to the large number of papers that have appeared, and continue to appear in this area.

Not surprisingly the first numerical technique applied to waveguide type problems was the finite difference method [19] although this method seems to have fallen out of favour during the intervening fifty years.

From a purely theoretical viewpoint any numerical method for solving partial differential equations must transform the analytic equation into a set of one or more algebraic equations that may be solved on a computer system. The techniques for transforming the problem are extremely varied but amongst the most common are the finite difference method, the finite element method and the Galerkin method. In the finite difference method the analytic partial derivatives are replaced by algebraic approximations defined using a grid defined over the region in which the solution is desired. The finite element method uses low order polynomials to approximate the solution of the partial differential equation over small regions or 'elements' into which the domain of interest is subdivided. The Galerkin method, on the other hand, requires the solution to be expressed as a (truncated) series of orthogonal functions defined over the entire domain of interest and so is sometimes referred to as a global method. Of course, the partial differential equation can also be converted to an integral equation which can then be discretized for computer solution. All these methods have been applied to the dielectric waveguide problem. Both the finite element and finite difference approaches lead to sparse matrix problems and these are discussed in Section 1.4.

The numerical method described in this thesis is, to the author's knowledge,

applicable to the widest range of waveguide problems of any existing solver. The method also possesses internal criteria of accuracy that are lacking from other methods thus increasing confidence in the numerical predictions.

1.3.1 The Scalar Wave Equation

The electromagnetic properties of an optical fibre or dielectric waveguide that is weakly guiding are accurately described by the scalar wave equation [20],

$$\left(\nabla^2 + k^2 n^2\right) \psi = \beta^2 \psi, \tag{1.2}$$

and it is not surprising that much effort has gone into its numerical solution.

Efficient and accurate methods for solving the scalar wave equation in a cylindrically symmetric radially inhomogeneous fibre have been extant for some time [21, 22]. Cohen, *et. al.* [23] provides an interesting comparison between numerical computation and experimental measurements of fibre dispersion characteristics. Sammut and Pask [21] detail a 'shooting method' in which the field inside the core region is matched to a decaying Bessel function solution in the (infinite) cladding region. This method can be used with a large number of in-core points and provides high accuracy [24].

Finite element solution of the scalar wave equation extends back at least as far as Chiang [25]. Chiang's method is applicable to arbitrary two-dimensional guiding structures although only single core examples (of wide geometrical variety) are presented.

Recently Tamil and Aicklen [26] presented a finite difference method for the radial wave equation and considered the effects of a finite cladding on modal propagation constants and cutoff. Seki, *et. al.* [27] have reported a non-uniform finite difference grid method that they applied to the two-dimensional dielectric rectangular waveguide problem. It has been pointed out by Vassallo [28] that modifications to the finite difference formulae at curved boundaries can lead to higher accuracy for the step-index fibre. However, for the case of arbitrary core refractive index variation where there is no clear core-cladding interface the additional complexity does not appear to be warranted.

The Fourier method of Henry and Verbeek [29] first presented for purely step-index waveguides has recently been extended to waveguides with arbitrary refractive index variation through the use of an 'onion skin' approach in which the core region is represented by a large number of slices [30]. The method has the advantage that dense matrix techniques are used to solve the resulting algebraic eigenproblem.

The method presented in Chapter 2 is a full two-dimensional finite difference solver, applicable to guides with arbitrary refractive index variation, that uses a

nonlinear transformation to map all of real space into the unit square. The scaling enables the solver to function correctly down to modal cutoff and provides better handling of curved boundaries than conventional finite difference methods because the grid is non-uniform in real space. Interestingly, in a recent review article, Chiang [31] points out the difficulties that conventional finite difference methods have in handling the infinite cladding and curved core-cladding boundaries which, as stated above, are alleviated in the method described in this thesis. Finite cladding effects, although not considered, would be simple to introduce by forcing the field to zero at a finite distance from the centre of the guide.

1.3.2 The Vector Wave Equation

The vector wave equation for the electric field vector $\mathbf{E}$ may be written as

$$\nabla^2 \mathbf{E} - \nabla (\nabla \cdot \mathbf{E}) = k^2 \varepsilon \mathbf{E} \tag{1.3}$$

where k is the free space wavenumber, ε is the permittivity tensor and it has been assumed that $\mathbf{E} \sim \mathbf{e}(x,y) \exp[-i(\omega t - \beta z)]$. Numerical solution of Equation (1.3) presents some difficulties. The first of these stems from the fact that the free space wavenumber is the computed eigenvalue and the propagation constant is required as *á priori* input. This is somewhat unnatural because fibres are operated at specified wavelengths (i.e. k values) not propagation constants. The second is the presence of 'spurious' modes—solutions of equation (1.3) that do not satisfy the divergence condition

$$\nabla \cdot (\varepsilon \mathbf{E}) = 0. \tag{1.4}$$

Equivalent formulations may be made in terms of the magnetic field, $\mathbf{H}$.

There is no requirement that the waveguide be isotropic and so ε is a second rank tensor that is Hermitian for a lossless medium as considered in this thesis.

The dominant numerical technique for the vector dielectric waveguide problem has been the finite element method and much effort has gone into eliminating spurious modes [32, 33, 34] although the reason why they occur is not fully understood. The method is general but the leaning has been toward the slab waveguide problem with few results for the circular fibre being available. The methods are also applicable to anisotropic waveguides but little attention has been paid to the off-diagonal permittivity components [35] and then only in a perturbative way. This latter neglect may be due simply to the added numerical complexity involved.

The method of choice in removing the spurious modes has typically involved the use of 'penalty' functions [36]. These functions which involve a free positive parameter, called a penalty coefficient, are added to the functional used in a conventional finite element approach. The penalty coefficient is usually chosen using

a least squares technique and the overall accuracy of the method does depend on the choice of the penalty coefficient, a somewhat undesirable situation.

The latest vectorial finite element methods [34, 37] avoid spurious modes and permit direct computation of the propagation constant [37]. The penalty function approach is not used so these methods have somewhat enhanced accuracy because an *ad hoc* parameter is not required.

The finite difference method has also been used previously to solve the vector wave equation. Early methods [38] required the computation of Bessel functions and were applicable only to radially inhomogeneous fibres. Decotignie, *et. al.* [39] present a rather interesting non-uniform grid technique based on the vector potential **A** rather than on the **E** or **H** fields. The method is used to analyse the step-core ellipse and overlapping circular twin-core fibres. Accuracy of the computed propagation constants is typically in the range 1–5%. Because step-index fibres are examined explicit boundary conditions are enforced in the analysis and add an additional level of complexity.

Stern [40, 41] has applied a semi-vectorial finite difference method to a range of slab waveguide problems. In this method the vector wave equation (1.3) is simplified by assuming the modal field has a particular polarisation (e.g. x-polarised, $\mathbf{E} = (E_x, 0, E_z)$). The resulting algebraic eigenvalue problem is solved by standard sparse matrix techniques.

For the purely radial, inhomogeneous, isotropic waveguide the staircase approximation technique [42] which has the advantage of providing the propagation constant directly, has been widely used. In this technique the radially inhomogeneous refractive index profile is divided up into a number of layers that are homogeneous and form a stepped approximation to the true refractive index profile. In each of the homogeneous layers the longitudinal electric field E_z and magnetic field H_z are known to be a linear combination of Bessel functions. The field solution in each layer must match at the layer boundaries and this leads to a system of linear equations for the unknown coefficients of the linear combination in each layer. Typically a refractive index profile is subdivided into 50 or so layers providing around 6 significant figures in the propagation constant. Dense matrix techniques are used to solve the linear systems.

The Rayleigh method of Lo, *et. al.* [43] is also based on the longitudinal field components but is applicable to the important case of multiple uniform isotropic cylindrical core regions. The connection between the cylinders is achieved through the use of an algebraic identity (the 'Rayleigh' identity). Again, a series of Bessel functions are used to represent the fields and the coefficients determined as solutions of a dense linear system. Recently [44] the method has been extended to the arbitrarily inhomogeneous cylinders via a staircase-approximation to the refractive index distribution over each cylinder.

The method presented in Chapter 3 is a fully two-dimensional finite difference

method based on the full electric field vector. Nonlinear scaling is used to map the whole of the real plane into the unit square. Arbitrarily shaped core regions with practically arbitrary permittivity distributions are accommodated. The novelty of the method lies in its generality and unambiguous accuracy. In most optical fibres there is no clear core-cladding boundary and so no boundary conditions other than that at infinity need be applied. Spurious modes, although intrinsically present, have not proved problematic.

1.4 Sparse Matrix Methods

A sparse matrix is usually defined to be a matrix in which a significant number of the matrix elements are zero. Such matrices arise in a large number of applications. In particular, partial differential equations when discretized using either finite elements or finite differences give rise to sparse matrices. In addition to having many zero elements, matrices arising from the discretization of partial differential equations are also large, often with many thousands of rows. The two main algebraic problems associated with sparse matrices are the same as those for dense matrices namely solving inhomogeneous linear systems and eigenproblems.

Of particular interest in sparse matrix work are storage schemes. Clearly the conventional scheme of storing each matrix element in a two-dimensional array is wasteful of space and becomes impossible for matrices larger than about 2000×2000 on most common modern computer hardware. The storage scheme used throughout the codes written for this thesis is known as the compressed sparse row (CSR) format. The CSR format is a fully general matrix storage scheme using three one-dimensional arrays, two integer and one real, no zeros are stored, see [45] for details.

1.4.1 Inhomogeneous Linear Systems

The methods for solving sparse linear systems divide into two broad groups. **Direct solution methods** extend the standard techniques of Gaussian elimination and the various matrix factorizations to sparse matrices. Such methods complete in a necessarily finite number of computer operations. **Iterative solution methods** progressively refine an initial guess at the solution of a linear system so that after some finite number of steps the current solution estimate is a good approximation to the true solution. Such methods may not converge to the solution of the linear system after an arbitrarily large number of steps for a variety of reasons some of which are discussed below. Modern iterative methods, of which the best known is the conjugate gradient scheme [46], are all part of a class of methods based on the theory of Krylov spaces, see [47] for details.

A complete survey of sparse matrix solution methods is beyond the scope of this thesis, however, an attempt to provide reasonable entry points into the literature is made.

For definiteness the generic linear system

$$Ax = b \tag{1.5}$$

where A is an $n \times n$ matrix, the right hand side, b, is a column vector of length n and x is the desired solution vector also of length n is used throughout the following discussion. In addition, it is assumed that a unique solution exists, that is, A is of full rank. A useful measure of the difficulty of solving Equation (1.5) is given by the condition number, $\kappa_p(A)$, defined by

$$\kappa_p(A) = \|A\|_p \|A^{-1}\|_p \tag{1.6}$$

where $\|\cdot\|_p$ denotes any matrix norm. A condition number of unity indicates a perfectly conditioned system and the larger the condition number the greater the difficulty of solving the system.

Direct Solution Methods

Direct methods have dominated the sparse matrix field for the past thirty years. The methods rely on the usage of graph theoretic techniques [48] to minimize the bandwidth of the matrix A via permutations of its rows and columns. Such bandwidth reduction has great impact on the memory requirements, and hence the viability, of the solver. An excellent review of the most widely used ordering algorithm is to be found in [49].

Direct methods are extensively documented in the books by George and Liu [50] and Duff, *et. al.* [51]. Such methods are quite hard to implement because of the necessary data structure manipulations that occur in the various phases of the solution. Consequently, the best codes are proprietary (Harwell Subroutine Library and Boeing Computer Services Library Extension) although they may be available in source form.

State of the art direct solvers are of the multifrontal type [52, 53] a development of the frontal method [54, 55] initially designed as a technique for solving the linear systems that arise from the finite element discretization of partial differential equations. The advantage of multifrontal (and frontal) methods over conventional LU-factorization is that the solution can be carried out in a much smaller amount of memory. The amount of memory required for solution is usually provided to the user from subroutines used to set up the problem. In addition the matrix factors may be written to disk rather than stored in memory thus reducing the amount of physical memory required even further.

Iterative Solution Methods

Although direct solution methods are used to solve the linear systems that arise in Chapter 3 of this thesis initial attempts were made made with iterative techniques. These failed primarily due to the difficulty of constructing a preconditioner for systems in which the matrix A is nearly singular.

The efficacy of an iterative solver depends strongly on the disposition of the eigenvalues of A. In general a matrix B, called a preconditioning matrix or preconditioner, which is in some sense an approximation to A^{-1} must be found in the hope that the system

$$BAx = Bb \tag{1.7}$$

is better conditioned than the original. There are a wide array of techniques for constructing preconditioners of which the most widely used are the incomplete factorizations in which some truncated form of the LU or Cholesky factors (if A is positive definite) of A are used to implicitly construct B. Such an incomplete factorization is almost certain to give a bad approximation to A^{-1} when A is nearly singular.

Compared to direct methods iterative methods are much easier to implement usually requiring only scalar products and matrix-vector multiplication. Consequently the matrix A need not be formed explicitly. Such methods are extremely memory conserving and practical for the largest systems.

A good account of state of the art iterative methods may be found in the book by Barrett, *et. al.* [56] which also contains a considerable number of references to the original literature.

1.4.2 Eigenproblems

When a boundary value problem is discretized using finite differences or finite elements the result will be an algebraic eigenproblem. The resulting matrices will be large and sparse and the desired eigenvalues are usually the largest or smallest in the spectrum (for an exception see Chapter 3). Clearly it would be wasteful of computer time and memory, and indeed impossible in most cases, to use a method that returned all the eigenvalues and eigenvectors. For this reason iterative methods have dominated in sparse eigenanalysis.

The eigenproblems that arise in this thesis are of the form

$$Ax = \lambda Bx \tag{1.8}$$

where A and B are symmetric positive definite, λ is an eigenvalue and x the corresponding eigenvector. When taken together, λ and x, are referred to as eigenpair and a system of the form shown in Equation (1.8) is referred to as a generalized eigenproblem.

The classic technique for solving Equation (1.8) is to factor B into its Cholesky factors $B = LL^T$ and solve the equivalent standard eigenproblem

$$L^{-1}AL^{-T}\left(L^T x\right) = \lambda\left(L^T x\right) \tag{1.9}$$

using the Lanczos algorithm [57]. Indeed, the Lanczos algorithm can be recast so as to not require the factorization which may in practice be computationally time consuming.

Much effort has gone into the study of the symmetric and nonsymmetric Lanczos algorithms and the related Arnoldi algorithm [58] for both eigenanalysis and solving linear systems. The books by Parlett [59] and Saad [45] provide detailed discussions of the state of the art in sparse eigenanalysis.

1.5 Applications

The finite difference solvers described in Chapters 2 and 3 are applicable to a wide class of practical design problems. Two such applications are described in Chapters 4 and 5.

Chapter 4 deals with design considerations for practical circularly birefringent optical fibres. The calculations carried out show that the vector solutions to the wave equation are required in certain problems of practical importance. Another conclusion that can be drawn from Chapter 4 is that in order to make accurate predictions of complex fibre designs involving stress producing elements it is necessary to have full knowledge of the permittivity tensor, including off-diagonal elements, as opposed to simply the refractive index distribution. At this stage experimental determination of the permittivity tensor cannot be carried out so full agreement between numerical simulations using the partial information contained in the refractive index distribution and experiments with real fibres cannot be expected to be very good.

In Chapter 5 design tolerances and sensitivities of a twin-core fibre wavelength demultiplexer are computed. These calculations make use of experimentally measured refractive index distributions—both one- and two-dimensional. In this case the fibres are nominally stress free and agreement between numerical simulation and experiment is adequate.

Future applications of the solvers include integration into an online facility where experimentally measured refractive index profiles of fibres and preforms are used as input data. The role of the system is perceived as being both in design and quality control. Indeed, if the measurement of the refractive index distribution is accurate then the prediction from the solvers of the fibre's electromagnetic properties will be accurate to the same level as has already been noted by Jaunart, *et. al.* [60].

User documentation for programs written during the course of this thesis is provided in Appendix B.

Chapter 2

Numerical Solution of the Scalar Wave Equation

2.1 Introduction

In this chapter a finite difference method for the solution of Maxwell's equations for the bound modes of a dielectric waveguide or optical fibre in the scalar (or 'weak guidance') approximation is presented. The method is extended to the full vector equations in the next chapter.

The immediate aim is to develop and prove a method which is sufficiently general and which yields solutions of high and *unambiguous* accuracy. Given such accuracy, any disagreement between calculation and observation must be ascribed to inadequacy of the model. The waveguide is modelled as straight and uniform in the direction of propagation and defined otherwise by a dielectric tensor distribution over its cross-section.

The longer term aim is to establish a reliable predictive system for linking observed properties of waveguides to modal characteristics. Our main focus is optical fibres. The dielectric tensor distribution over the cross-section of an optical fibre is difficult to measure, particularly where there is significant stress birefringence, so that the information which the computational method uses as a starting point is not usually available using present techniques with an accuracy that matches the accuracy of the computation. This circumstance provides no justification for employing computational methods of low or ambiguous accuracy. The desired predictive system has two parts, first measurement and secondly calculation. If the computational part is beyond reproach, but predictions do not match observation, then the spotlight is clearly focussed on the prior measurements.

The present chapter calculates modal properties—propagation constants, fields, waveguide dispersion and cutoff—for a number of model refractive in-

dex cross-sections, employing the scalar approximation. The main purpose is to demonstrate the method, rather than make useful predictions about real fibres. The usefulness for fibre modelling is illustrated in Chapter 5.

Evidence for the accuracy of the results is largely *convergence* of the propagation constant estimates (as the numerical mesh size decreases) and *small residuals* and *low spatial noise* in the field estimate, especially those obtained on the finest meshes. Further evidence is provided by the agreement between the numerical results and analytic results where these are available, and by the consistency of the results provided by different forms of the current method (for example, different ways of mapping the infinite two dimensional cross-section of the fibre onto the finite rectangular configuration space used for the finite difference computation). Evidence that the propagation constants are typically correct (as solutions of the given mathematical problem) to 6 or more significant figures is presented. Some indication of the accuracy of the corresponding fields is provided by the fact that they satisfy the (finite difference form of) the field equations when substituted into it. A normalized mean square residual is calculated and indicates an average accuracy of better than 3 significant figures in typical cases. Methods based on expansion of the fields in terms of a (necessarily finite) series of analytic functions inevitably impose an upper bound on the spatial frequencies which can appear in the approximate representation of the field. It will look and be smooth, whether it is accurate or not. Finite difference methods, on the other hand, impose no upper bound on the spatial frequencies which can be represented, except those determined by the mesh size h. As the mesh size is reduced, new structures appear in the finite difference representation of the field. Before the mesh size is small enough to represent a given structure (because it is characterised by spatial frequencies which are large compared to $1/h$) the emerging structure appears as noise. The contention is that the fields are at least as accurate as they look.

The most conspicuous limitation of the method is that it cannot handle too complicated a refractive index distribution—because the mesh size required to adequately represent the distribution is so small that computation time becomes too long. With computing power represented by a Sun4/690MP a fibre with several cores, each with some internal structure can nevertheless be handled. In general, sharp boundaries in the refractive index distribution can be handled without concern because both the field and its derivative are continuous everywhere. However, the extrapolation technique described in Section 2.4 is ineffective.

2.2 Formulation

A dielectric waveguide is considered to consist of a uniform cladding medium with refractive index n_{cl} and a core medium with maximum refractive index n_{co}.

In order for such a structure to support bound propagating modes the core index must be larger than the cladding index. The modes of the waveguide may be obtained as solutions of the vector wave equation. However, it is well known that if the profile height parameter

$$\Delta = \frac{n_{co}^2 - n_{cl}^2}{2n_{co}^2} \tag{2.1}$$

is much less than unity then the vector fields may be constructed to sufficient accuracy from solutions of the scalar wave equation [20]

$$\left(\frac{\partial^2}{\partial x^2} + \frac{\partial^2}{\partial y^2}\right)\psi + (k^2 n^2(x,y) - \beta^2)\psi = 0, \tag{2.2}$$

where $k = \omega/c$ is the free space wave number and β is the modal propagation constant. A dielectric waveguide for which the replacement is valid is said to obey the weak guidance approximation which, despite the terminology, does not mean that the modes of the guide are weakly bound. All field polarisation information is lost in the scalar formalism. It is important to note that the scalar theory is only an approximation to the rigorous vector theory presented in Chapter 3. The discrepancy between scalar and vector theory may also be quantified by using the polarisation corrections given in [20].

The guiding structure is assumed to be uniform in the propagation direction (z-axis) and accordingly a complete set of solutions can be found in the form

$$\psi = \psi \exp(-i(\omega t - \beta z)) \tag{2.3}$$

The cladding is assumed to extend to infinity and all media are assumed to be lossless.

It is convenient to introduce dimensionless length variables

$$X = kx \tag{2.4}$$
$$Y = ky \tag{2.5}$$

whence Equation (2.2) becomes

$$\left(\frac{\partial^2}{\partial X^2} + \frac{\partial^2}{\partial Y^2}\right)\psi + (n^2(X,Y) - n_e^2)\psi = 0, \tag{2.6}$$

where k is the free space wavenumber and $n_e = \beta/k$ is the effective modal refractive index.

The infinite domain of X and Y is reduced to the unit square $(u_1, u_2) \in (-1/2, 1/2) \times (-1/2, 1/2)$ by means of a non-linear transformation $X = \varphi_1(u_1)$,

$Y = \varphi_2(u_2)$. The φ_i must increase monotonically from $-\infty$ to ∞ as the u_i increase from $-1/2$ to $1/2$. The functional form of the φ_i is constrained by the requirement that the features of the modal field be equitably represented in the (u_1, u_2) configuration space in which a uniform rectangular finite difference grid is used. Satisfactory results were obtained with φ_i of the form

$$\varphi_i(u_i) = P_1(u_i)\tan(\pi u_i) + P_2(u_i)\tanh(a u_i) \tag{2.7}$$

where $P_1(u_i)$ and $P_2(u_i)$ are low degree even polynomials with real coefficients. In particular, $P_2(u_i) = 0$ is suitable for central refractive index profiles. The P_i's and the parameter a are chosen so that the field distribution both inside and outside the core is equitably represented by the resulting finite difference mesh.

In order to maintain the self-adjoint property of the differential operator in Equation (2.6) it is convenient to express second order partial derivatives in configuration space as, for example,

$$\frac{\partial^2}{\partial X^2} = \frac{\partial \varphi_1}{\partial X}\frac{\partial}{\partial \varphi_1}\left(\frac{\partial \varphi_1}{\partial X}\frac{\partial}{\partial \varphi_1}\right) \tag{2.8}$$

where the usual liberty of using a function involved in a coordinate transformation as the symbol for that coordinate has been used. Carrying out the replacement of the partial derivatives and multiplying through by

$$J = \varphi_1'(u_1)\varphi_2'(u_2), \tag{2.9}$$

the Jacobian of the coordinate transformation, gives the final form of the scalar wave equation in configuration space

$$\left[\frac{\partial}{\partial u_1}\left(\frac{\varphi_2'(u_2)}{\varphi_1'(u_1)}\frac{\partial}{\partial u_1}\right) + \frac{\partial}{\partial u_2}\left(\frac{\varphi_1'(u_1)}{\varphi_2'(u_2)}\frac{\partial}{\partial u_2}\right)\right]\psi + (n^2(u_1,u_2) - n_e^2)J\psi = 0 \tag{2.10}$$

where $'$ denotes differentiation with respect to the function's argument. The only restriction placed on ψ is that it vanish on the boundary because it represents a guided mode.

2.3 Numerical Method

Equation (2.10) is discretized using first order forward and backward finite difference representations for the partial differential operators. The low order of the discretization is offset by the use of Richardson's 'deferred approach to the limit' [61] to obtain high order and (in most cases) accurate results. To this end, the resulting algebraic eigenvalue problem is solved on a sequence of increasingly

fine meshes. The finite difference representation is chosen in such a way that the resulting algebraic eigenvalue problem is real symmetric (or Hermitian).

Denote by Γ_1 the forward difference operator that acts only on functions of u_1,

$$\Gamma_1 = \frac{1}{h}\begin{bmatrix} -1 & 1 & 0 & 0 & & & \\ 0 & -1 & 1 & 0 & & \cdots & \\ & & -1 & 1 & & & \\ & & & & & & \\ & & & & -1 & 1 & 0 \\ & \cdots & & & 0 & -1 & 1 \\ & & & & 0 & 0 & -1 \end{bmatrix}. \tag{2.11}$$

where $h = 1/N$ is the mesh spacing and N an integer with the grid having $(N-1)\times(N-1)$ interior points.

It follows that $(-\Gamma_1)^T$ is the backward finite difference operator that acts only on functions of u_1. Similarly we define Γ_2 and $(-\Gamma_2)^T$ as the forward and backward finite difference operators acting on functions of u_2 only.

With the notation introduced above the differential operator in equation (2.10) may be written as the symmetric matrix

$$A_1 = \frac{1}{2}\left[(-\Gamma_1)^T g_1 \Gamma_1 + \Gamma_1^T g_1 (-\Gamma_1)\right] + \frac{1}{2}\left[(-\Gamma_2)^T g_2 \Gamma_2 + \Gamma_2^T g_2 (-\Gamma_2)\right] \tag{2.12}$$

where $g_1 = \mathrm{diag}(\varphi_2'/\varphi_1')$ and $g_2 = \mathrm{diag}(\varphi_1'/\varphi_2')$. It follows that the finite difference representation of Equation (2.10) is

$$A\psi = n_e^2 J\psi \tag{2.13}$$

where $A = A_1 + J\,\mathrm{diag}(n^2(u_1,u_2))$ is a large, sparse positive definite matrix. The positive definiteness of A follows by taking the product of Equation (2.13) on the left with ψ and noting that the right hand side, which represents an energy, is positive for all choices of ψ.

The structure of A_1 is identical to the matrix representation of the standard five point finite difference Laplacian stencil. However, even if the g_i's are identity mappings the actual elements of A_1 differ from the $(+1\ +1\ -4\ +1\ +1)$ pattern of the standard stencil. The reason for this is that the endpoints are handled more smoothly rather than by simple truncation. The rows of A_1 grade from $(-3\ +\ 1\ +1)$ at a corner point of the finite difference grid to $(+1\ +1\ -3.5\ +1\ +1)$ for points adjacent to the boundary and $(+1\ +1\ -4\ +1\ +1)$ for fully interior points.

Equation (2.13) is a symmetric generalized eigenproblem; both A and J are positive definite in all cases of physical interest. Reduction to a standard eigenproblem is accomplished by taking the square root of J. This is trivial because J

is diagonal and positive definite. The resulting standard eigenproblem is

$$\bar{A}\bar{\psi} = n_e^2\bar{\psi} \tag{2.14}$$

where $\bar{A} = J^{-\frac{1}{2}}AJ^{-\frac{1}{2}}$ and $\bar{\psi} = J^{\frac{1}{2}}\psi$. The reduction to standard form is not necessary but is desirable from the numerical point of view in that an overall reduction in operations per iteration is achieved.

The largest eigenvalue of Equation (2.14) corresponds to the square of the effective index of the fundamental bound mode of the guiding structure. The square of the effective indices of the higher order modes are available as the successively smaller eigenvalues.

The required eigenvalues of Equation (2.14) were found using the block Lanczos eigensolver provided as part of the BCSlib package from Boeing Computer Services. The Lanczos process [57], [47] is a method of transforming a symmetric positive definite matrix A into a tridiagonal matrix T. In exact arithmetic the Lanczos process produces an exact tridiagonalization in a finite number of steps but in practice the process will break down before the tridiagonalization is complete due to accumulation of roundoff errors. The remarkable property of the Lanczos process is that as the tridiagonalization proceeds in an iterative manner the largest (or smallest, depending on the how the problem is set up) eigenvalues of the successive partial tridiagonalizations are good approximations to the largest eigenvalues of A. Approximations of the eigenvectors corresponding to the largest eigenvalues of A are obtained by a back transformation of the eigenvectors of T_i (an $i \times i$ tridiagonal matrix), the partial tridiagonalization of A at the ith iterative step, using auxiliary vectors (the Lanczos vectors) produced by the iterative process.

In its basic form the Lanczos process does not handle the case of multiple eigenvalues particularly well. Several schemes have been proposed to alleviate this difficulty; the most robust of which is a block form of the Lanczos process in which a block size at least as great as the largest expected eigenvalue multiplicity is used [62]. This is the scheme used here. In addition to using a block form of the Lanczos algorithm the BCSlib eigensolver also uses a shift-and-invert strategy [45] to speed up overall convergence.

The BCSlib sparse eigensolver allows the user to specify an upper and lower bound between which eigenvalues will be sought. For the purpose of the present work this enables all bound modes to be found by restricting the search range to lie between the refractive index of the cladding and the maximum refractive index of the core. In particular, dispersion plots can be readily generated.

All fields are normalized in the J-norm, *vis.*

$$\psi\text{norm} = \frac{\psi}{\psi^T J\psi}. \tag{2.15}$$

2.4 Verification

The method presented has been found to work for a wide class of refractive index profiles whether analytical models or data obtained experimentally.

In order to provide a benchmark for the procedure the infinite parabolic profile was used:

$$n^2(R) = n_{\mathrm{CO}}^2(1 - 2\Delta R^2) \tag{2.16}$$

where $R = r/\rho$, $\rho = 1\mu\mathrm{m}$, $n_{\mathrm{CO}} = 1.5$ and $\Delta = 10^{-4}$. The operating wavelength was chosen to be 1.3μm. The analytically determined [20] value for the square of the effective index of the fundamental mode is 2.2412219159 compared to the numerical result (see Table 2.1) of 2.241221914. Table 2.1 is typical of the

N	n_e^2			
50	2.24123426604			
		2.24121161929		
60	2.24123049158		2.24122192173	
		2.24121456284		2.24122191435
70	2.24122821605		2.24122191896	
		2.24121640187		
80	2.24122673928			

Table 2.1: Extrapolation table for infinite parabolic profile

triangular extrapolation tables produced by the method. The first column is the number of mesh lines in the finite difference grid and the second column is the raw value of the square of the effective index calculated numerically on that mesh. Subsequent columns are obtained from the preceding column by eliminating the leading power of h remaining in the error series. To obtain the second column we eliminate terms linear in h; the third column is obtained from the second by eliminating terms quadratic in h and so on as we progress from left to right across the table.

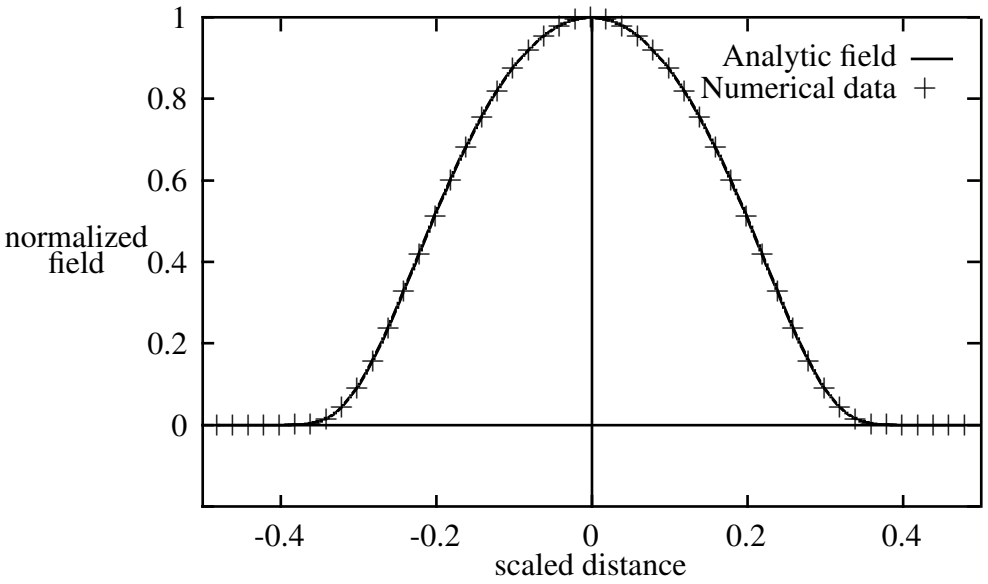

Figure 2.1: Numerical and analytic field for infinite parabolic profile

The entry $n_e^{2\,(r,s)}$ in the sth column is obtained from entries in the $(s-1)$th column by the rule

$$n_e^{2\,(r,s)} = \frac{N_{(r+3)} n_e^{2\,(r-1,s-1)} - N_{(r-1)} n_e^{2\,(r+2,s)}}{N_{(r+3)} - N_{(r-1)}} \tag{2.17}$$

where $N_{(r+3)}$ and $N_{(r-1)}$ are the mesh-sizes (in the first column) immediately above and below the desired new entry.

Notice that the entries in the $(s-1)$th column straddle the new entry in the sth column. The raw eigenvalues are needed to high accuracy (about 12 significant figures in this case) because any noise in the original data will be amplified by the extrapolation process. Convergence of the extrapolates is seen to be taking place in a two sided fashion towards the centre of the table and also towards the right. The right hand vertex of the triangle is the best approximation to the desired eigenvalue.

Refractive index profiles with discontinuities do not permit the use of extrapolation and in this situation it is necessary to revert to one run with a fine mesh. Numerical experiments have indicated that a mesh of 150×150 is sufficient to obtain 6 significant figures in the great majority of cases although the actual mesh size required for a given accuracy is somewhat scaling dependent.

The scalar field is also obtained to high accuracy as may be seen from Figure 2.4. The numerical data is that from the 50×50 mesh. The root mean square departure of the numerical data from the analytic field is 3.5×10^{-4}.

2.5 Example Applications

The technique presented in the previous sections cannot compete in speed with methods that integrate the radial form of the wave equation [22] or techniques that take advantage of core symmetry, for example finite element methods that discretize one quarter of a four-fold symmetric core geometry [25]. However, for refractive index distributions which lack radial or other obvious symmetries the general technique described here provides a rapid means of solution. No special triangularization or trial functions need to be chosen; merely an analytic or spline representation of the refractive index profile is required. Choice of the scaling parameters can be made rapidly by viewing the resulting field distributions on extremely coarse meshes and with some experience parameters can be chosen adequately from knowledge of the refractive index distribution without trial runs.

All surface plots are shown with the vertical axis labelled 'Electric Field Strength' and although this is not strictly correct because the true propagating fields are vectorial in nature, it is a valid description within the weak guidance approximation.

2.5.1 Twin-core Fibre

As a non-trivial application results for a model of a twin-core fibre manufactured at the Optical Fibre Technology Centre, University of Sydney are presented. The experimentally determined refractive index profile is shown in Figure 2.2. These data were obtained using a York Technologies S14 fibre refractive index profiler. Some discussion of this profile is worthwhile as it is not immediately clear how closely this resembles the *true* refractive index distribution of the fibre.

Notice that the experimentally measured cores are asymmetric. This is perhaps due to experimental technique—it is difficult to ensure measurement is carried out along the diameter of the fibre passing through the centre of both cores—or it may be genuine. We have assumed that, since the cores are both derived from the same precursor preform, they are identical and have modelled the profile analytically by the expression

$$n(x,y) = n_{cl} + \left(\Delta + \frac{r_+(x,y)^2}{a^2}\right)\exp\left(-\frac{r_+(x,y)^4}{b^4}\right) + \left(\Delta + \frac{r_-(x,y)^2}{a^2}\right)\exp\left(-\frac{r_-(x,y)^4}{b^4}\right) \tag{2.18}$$

where $r_\pm(x,y)^2 = (x \pm s)^2 + (y \pm s)^2$ with $n_{cl} = 1.457$, $\Delta = 0.005$, $a = 45\mu$m, $b = 3.7\mu$m and $s = 7.5\mu$m is half the core separation. The analytic profile is shown

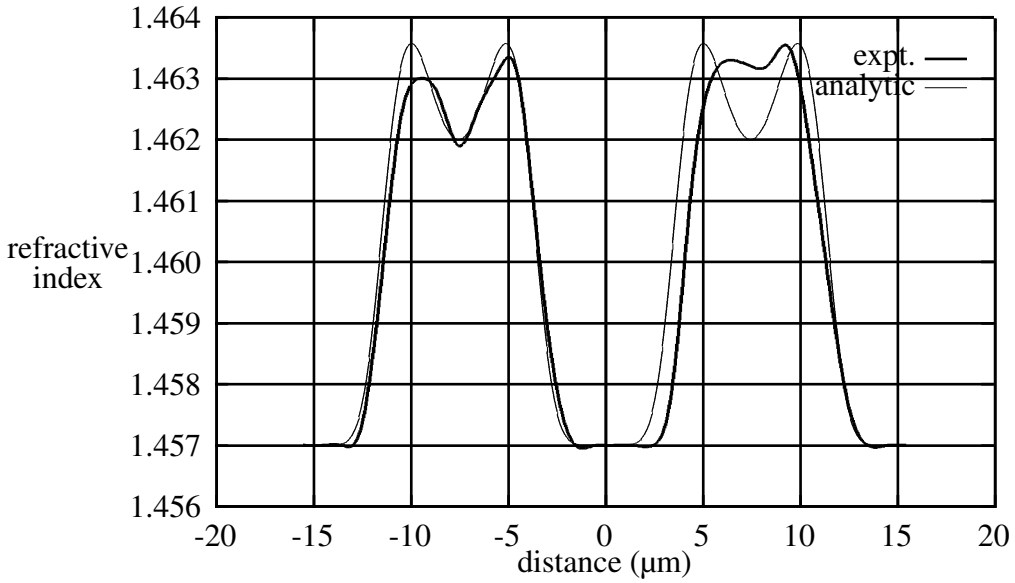

Figure 2.2: Experimental and model refractive index profiles

overlaid on the experimental profile in Figure 2.2 for comparison. The peak core-cladding refractive index difference of 0.0065 is small enough to ensure that the scalar approximation is valid. Tables 2.2 and 2.3 show the eigenvalue extrapola-

N	n_e^2				
80	2.132993567				
		2.132955637			
90	2.132989353		2.132973828		
		2.132959276		2.132973508	
100	2.132986345		2.132973741		2.132973595
		2.132961906		2.132973537	
110	2.132984123		2.132973690		
		2.132963870			
120	2.132982435				

Table 2.2: Extrapolation table for first even mode of twin-core fibre

tions for the even and odd supermodes of the twin core fibre. Calculations were carried out at a vacuum wavelength of 1.3μm. Convergence to 2.1329736 and 2.1329006 respectively is clearly seen. The corresponding effective index values are 1.4604703 and 1.4604453 respectively.

N	n_e^2				
80	2.132920900				
		2.132882453			
90	2.132916628		2.132900899		
		2.132886142		2.132900567	
100	2.132913580		2.132900809		2.132900666
		2.132888809		2.132900600	
110	2.132911328		2.132900756		
		2.132890800			
120	2.132909617				

Table 2.3: Extrapolation table for first odd mode of twin-core fibre

The modal coupling constant C is defined by [20]

$$C = 0.5(\beta_+ - \beta_-) \tag{2.19}$$

where β_+ and β_- are the modal propagation constants for the even and odd supermodes respectively. The beat length z_b (i.e. the distance required for complete power transfer from one core to the other and back again) is defined by

$$z_b = \frac{\pi}{C}. \tag{2.20}$$

Using the values of the effective indices stated above, the beat length for coupling between the even and odd supermodes of this fibre is 52.02mm. In fact the fibre used in this study was designed to have minimal coupling between cores and this is indicated by the relatively long beat length.

Representative field plots are shown in Figures 2.3 and 2.4. Note that the x- and y-axes are labelled in terms of scaled distance, that is, distance in the configuration space and that the electric field strength is normalized as specified above and displayed in arbitrary units. In general, transformation back to real Cartesian space must be carried out numerically due to the transcendental nature of the transformations. Calculations involving the fields are as easily performed in configuration space as in Cartesian space and so transformation back to real space is rarely carried out. Display of the back transformed data is also somewhat more difficult owing to the non-uniform grid spacing in real space.

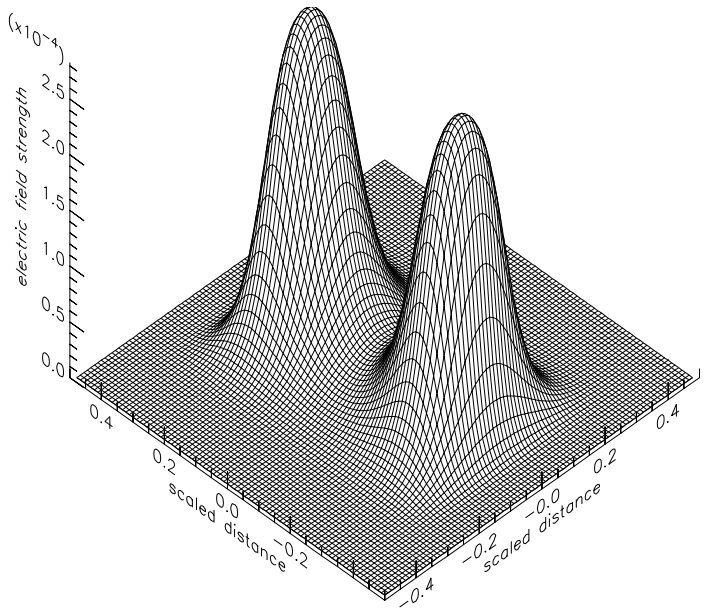

Figure 2.3: Even supermode of twin-core fibre

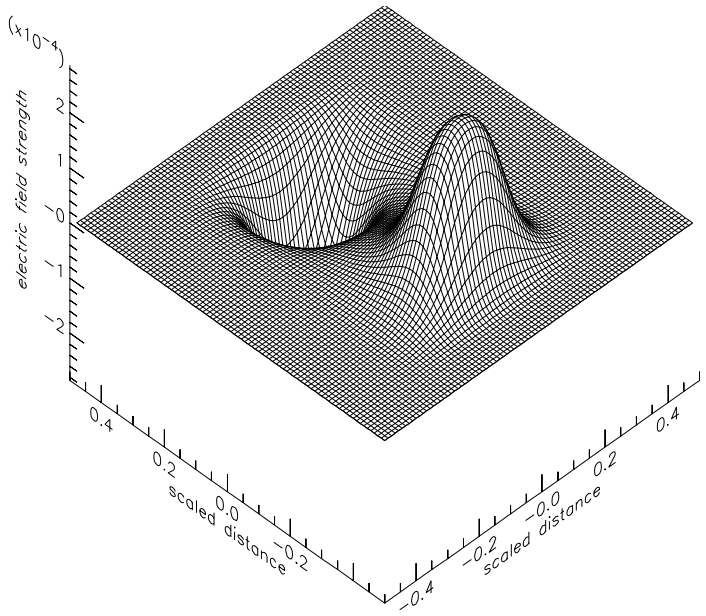

Figure 2.4: Odd supermode of twin-core fibre

2.5.2 Single-core—Preform data

The method described is robust enough to be used to analyse proposed fibre designs using scaled versions of preform data. It is then a relatively straightforward matter to predict the cut-off wavelength for the second mode, group delay and dispersion. Two-dimensional data from the preform or fibre profiler is also able to be used and some results will be shown in Chapter 5. The data were fitted using a natural cubic [63] or optionally a natural quintic spline [64].

Figure 2.5 shows the single core preform profile data that was used. No smoothing of the profile was carried out so extrapolation over a sequence of mesh sizes was not possible. The actual cladding index used was determined from the Sellmeier expansion

$$n^2(\lambda) = 1 + \sum_{i=1}^{3} \frac{A_i \lambda^2}{\lambda^2 - B_i^2} \tag{2.21}$$

using the coefficients for fused silica given in [65]. The core-cladding index difference was assumed to be independent of wavelength although inclusion of this effect would be straightforward. The wavelength used was 1.3μm.

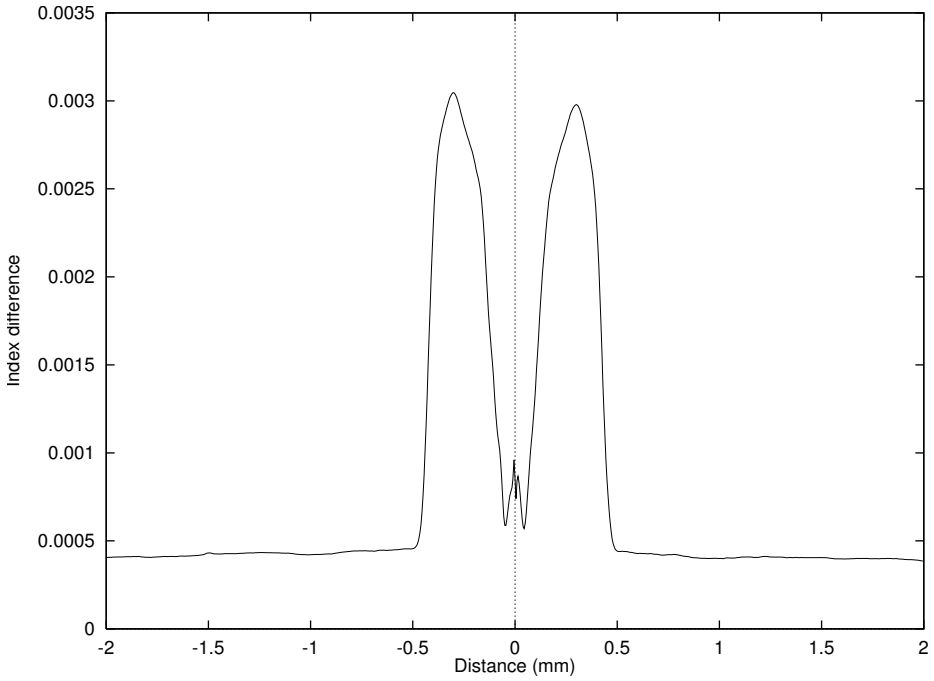

Figure 2.5: Preform profile data

The results are tabulated for a sequence of meshes in Table 2.4. These results indicate an eigenvalue of 2.095294 to 6 significant figures and a corresponding

effective index of 1.447513.

Grid size	Eigenvalue
50	2.0953001
100	2.0952946
150	2.0952940
200	2.0952936

Table 2.4: Eigenvalue data for real profile

A surface plot of the fundamental modal field is shown in Figure 2.6. The slight dip in the centre is characteristic of fibres with strong central dips in the refractive index distribution because the guiding region is tending to an annular shape rather than cylindrical. Physically, the dip in the refractive index distribution is due to germanium boil-off during fabrication and is a property of all fibres made using the modified chemical vapour deposition technique.

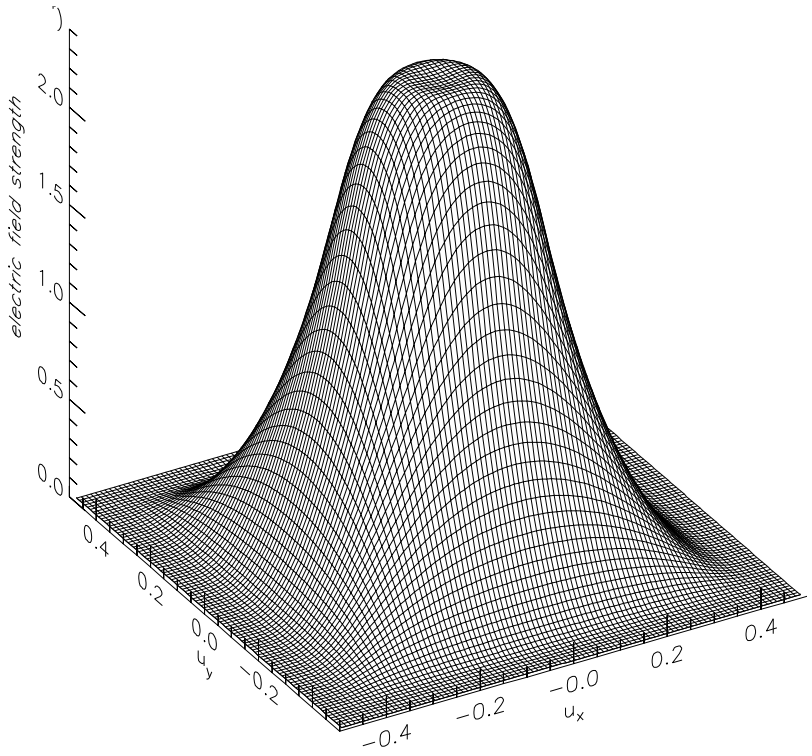

Figure 2.6: Fundamental mode of real profile

The dispersion curve for this fibre over the range $2 \times 10^6 \mathrm{m}^{-1} \leq k \leq 1 \times$

$10^7 \mathrm{m}^{-1}$ is shown in Figure 2.7. Cutoff of the second mode occurs at $\lambda = 0.9267\mu\mathrm{m}$.

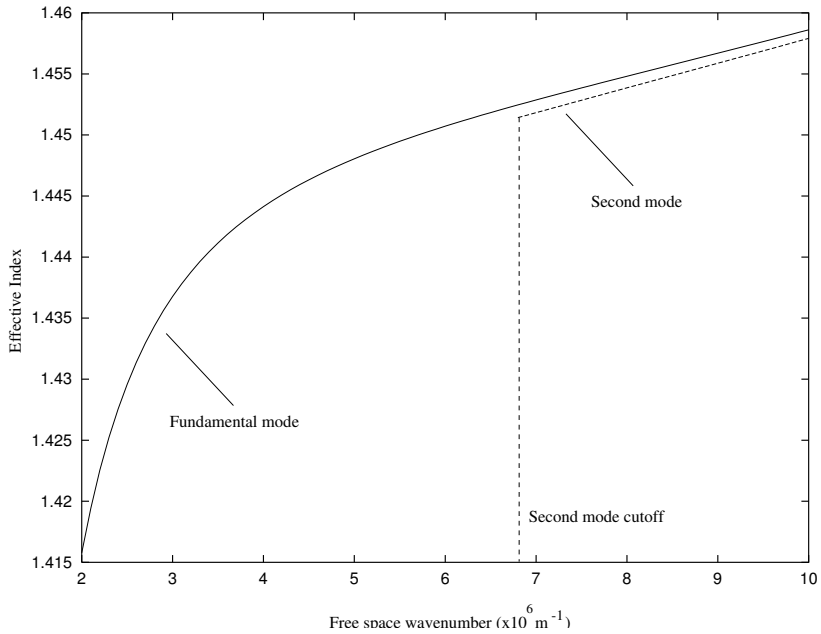

Figure 2.7: Dispersion curves

2.5.3 Group Delay and Chromatic Dispersion

The group delay and chromatic dispersion are two important related parameters that are often used in optical fibre work. An expression for the group delay can be rigorously derived from the Helmholtz equation using perturbation theory. The advantage of this approach is that numerical differentiation is avoided and the chromatic dispersion may then be computed via a single differentiation.

Consider an arbitrary Hermitian eigenproblem in which the left hand side operator is dependent on a parameter, η

$$A(\eta)\psi = \lambda\psi. \tag{2.22}$$

Differentiating both sides with respect to η gives

$$A(\eta)\frac{d\psi}{d\eta} + \frac{dA(\eta)}{d\eta}\psi = \lambda\frac{d\psi}{d\eta} + \frac{d\lambda}{d\eta}\psi \tag{2.23}$$

where

$$\frac{dA(\eta)}{d\eta}\psi \tag{2.24}$$

is to be interpreted as

$$\frac{d}{d\eta}\left(A(\eta)\psi\right). \tag{2.25}$$

Multiplying on the left by ψ^H, the Hermitian conjugate field, and noting that

$$\psi^H A = \psi^H \lambda \tag{2.26}$$

then we arrive at an expression for $\frac{d\lambda}{d\eta}$

$$\frac{d\lambda}{d\eta} = \frac{\int\int \psi^H \frac{dA}{d\eta}\psi\, dy\, dx}{\int\int \psi^H \psi\, dy\, dx} \tag{2.27}$$

where the integration is over all the real plane. Comparing Equation (2.22) with the Helmholtz Equation (2.2) and identifying

$$\begin{aligned} \eta &= k^2 \\ \lambda &= \beta^2 \\ A &= \frac{\partial^2}{\partial x^2} + \frac{\partial^2}{\partial y^2} + k^2 n^2 \end{aligned}$$

and noting that $\frac{\partial^2}{\partial x^2} + \frac{\partial^2}{\partial y^2}$ commutes with $d/d(k^2)$ it follows that

$$\begin{aligned} \frac{dA}{d\eta} &= \frac{dA}{d(k^2)} \\ &= \frac{d}{d(k^2)}(k^2 n^2) \end{aligned}$$

and so

$$\frac{d(\beta^2)}{d(k^2)} = \frac{\int\int \psi^H [\frac{d}{d(k^2)}(k^2 n^2)]\psi\, dy\, dx}{\int\int \psi^H \psi\, dy\, dx} \tag{2.28}$$

or

$$\frac{d(\beta^2)}{d(k^2)} = \frac{\int\int \psi^H J[\frac{d}{d(k^2)}(k^2 n^2)]\psi\, du_1\, du_2}{\int\int \psi^H \psi J\, du_1\, du_2} \tag{2.29}$$

in configuration space. The derivative in the numerator can be calculated analytically from the Sellmeier expansion so numerical differentiation is not required.

Numerically, the integrals may be replaced by inner products, giving

$$\frac{d(\beta^2)}{d(k^2)} = \frac{\psi^T J[\frac{d}{d(k^2)}(k^2 n^2)]\psi}{\psi^T J \psi} \tag{2.30}$$

The group delay is given by

$$\tau_g = L\frac{d\beta}{d\omega} \tag{2.31}$$

where L is the fibre length, is readily expressible in terms of $\frac{d(\beta^2)}{d(k^2)}$ by simple application of the chain rule

$$\tau_g = \frac{L}{cn_e}\frac{d(\beta^2)}{d(k^2)} \tag{2.32}$$

where c is the velocity of light in free space. The group velocity is the reciprocal of the group delay

$$v_g = \frac{1}{\tau_g}. \tag{2.33}$$

The chromatic dispersion, C, is defined by

$$C = \frac{d\tau_g}{d\lambda} \tag{2.34}$$

where λ is the free space wavelength and is of particular importance in optical communication systems because it is directly related to the broadening of a light pulse as it propagates along the fibre [66].

C may be easily re-expressed as

$$C = \frac{\lambda}{c}\frac{d^2n_e}{d\lambda^2} \tag{2.35}$$

and noting that

$$\frac{dn_e}{d\lambda} = \frac{1}{\lambda}\left(n_e - \frac{d\beta}{dk}\right) \tag{2.36}$$

and

$$\frac{d\beta}{dk} = \frac{k}{\beta}\frac{d(\beta^2)}{d(k^2)} \tag{2.37}$$

it is evident that the chromatic dispersion is calculable via a single numerical differentiation.

The accuracy of the computed chromatic dispersion is limited by both the error in the computed value of $\frac{d(\beta^2)}{d(k^2)}$ and the intrinsic error in the numerical differentiation scheme used. It should be noted that $\frac{d(\beta^2)}{d(k^2)}$ is as accurate as β^2 because it is calculated using a similar ratio of scalar products.

Plots of the group delay relative to the group delay at 1.3μm (i.e. $\tau - \tau_{1.3}$) and chromatic dispersion for the single mode fibre discussed above are shown in Figures 2.8 and 2.9 respectively.

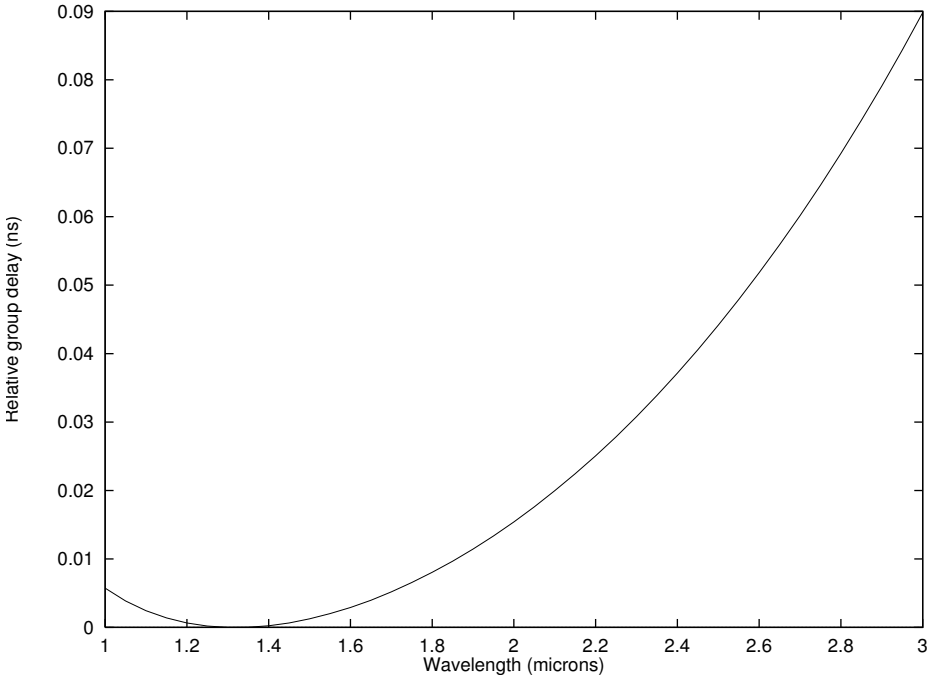

Figure 2.8: Relative group delay over the range 1–3μm

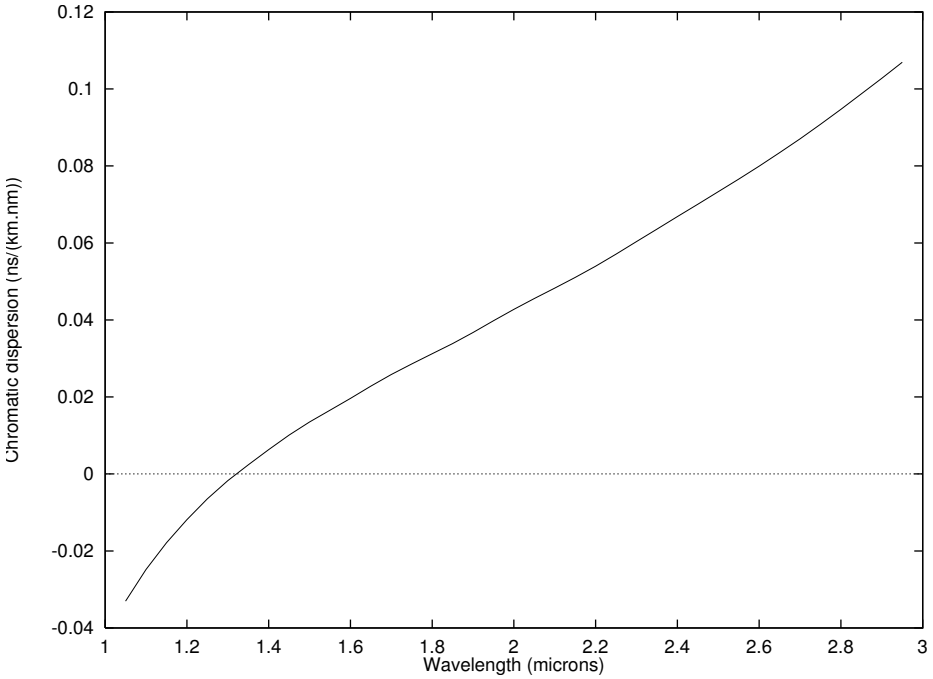

Figure 2.9: Chromatic dispersion over the range 1–3μm

With reference to Figure 2.9 it is evident that zero chromatic dispersion occurs at 1.3μm indicating that the fibre will have excellent transmission characteristics at that wavelength.

2.6 Conclusion

The technique for solving the scalar wave equation described in this chapter is extremely versatile in the range of fibre geometries that can be handled. It is robust enough to handle the inherently noisy refractive index profiles obtained from a preform profiler and fast enough to be a useful workstation (or well equipped PC) based tool in a fibre fabrication facility.

On the downside, because it is fully two-dimensional, the method cannot compete with techniques that integrate the radial wave equation directly or with finite element methods that make use of symmetry to reduce the number of elements required and hence the matrix order. However, the accuracy of the method is unambiguous and is in complete agreement with other less general methods [24].

Speed comparisons against a locally available version of an implementation of the method of Henry and Verbeek [29] come down in favour of the current method at equivalent accuracy levels.

Chapter 3

Numerical Solution of the Vector Wave Equation

3.1 Introduction

The analysis of optical fibres using the scalar wave equation is not applicable to all fibre designs that are currently being manufactured or contemplated. This is particularly true in the area of fibre sensing where fibres with large degrees of anisotropy and large core-cladding refractive index differences are being used. For this class of fibre, recourse to the full vector wave equation must be made with ensuing complications in the analysis—both analytic and numeric. These complications arise from the generality of the vector wave equation and are particularly evident when the dielectric tensor that describes the fibre medium is not isotropic.

The method for solving the vector wave equation described in this chapter is the direct generalization of the scalar method described in the previous chapter. The technique is in principle applicable to arbitrary lossless smoothly varying permittivity distributions with some restrictions elaborated upon in the text. The requirement of smooth variation rules out step profiles. In practice, however, the vast majority of silica based optical fibres are manufactured using modified chemical vapour deposition (MCVD) [67] and it is not possible, with this technique, to manufacture true step profile fibres. In fact the edges of the refractive index profile rarely fall faster than the super-Gaussian $\exp(-(r/a)^6)$ for suitably chosen a and usually no faster than $\exp(-(r/a)^4)$ as may be seen by referring to figure 2.2.

3.2 Formulation

Consider an arbitrary inhomogeneous anisotropic dielectric waveguide of infinite extent. The propagating (or bound) modal fields of the guide are defined to be those electromagnetic fields that propagate unattenuated along its length. Such solutions can be written as

$$\mathbf{E}(\mathbf{x},t) = \mathbf{E}(x,y)\exp[-i(\omega t-\beta z)] \tag{3.1}$$
$$\mathbf{H}(\mathbf{x},t) = \mathbf{H}(x,y)\exp[-i(\omega t-\beta z)] \tag{3.2}$$

where $\mathbf{E}$ is the electric field vector, $\mathbf{H}$ is the magnetic field vector, ω is the (angular) frequency of the fields and β is the modal propagation constant. Maxwell's equations may be written as

$$\nabla\times\mathbf{E} = \bar{\mu}i\omega\mathbf{H} \tag{3.3}$$
$$\nabla\times\mathbf{H} = -\bar{\varepsilon}i\omega\mathbf{E} \tag{3.4}$$
$$\nabla\cdot(\bar{\mu}\mathbf{H}) = 0 \tag{3.5}$$
$$\nabla\cdot(\bar{\varepsilon}\mathbf{E}) = 0 \tag{3.6}$$

where $\bar{\varepsilon}$ is the permittivity tensor, $\bar{\mu}$ is the permeability tensor of the dielectric waveguide and the time derivatives have been explicitly computed using the form of the fields above. The waveguide material is assumed lossless and not magneto-active so $\bar{\varepsilon}$ is a real symmetric second rank tensor [68] and $\bar{\mu}$ reduces to the scalar μ_0—the permeability of free space. No static fields are assumed present.

Taking the curl of Equation (3.3) and using equation (3.4) the vector wave equation for the electric field vector is obtained

$$\nabla\times\nabla\times\mathbf{E} = \omega^2\mu_0\bar{\varepsilon}\mathbf{E} \tag{3.7}$$

An equivalent equation for the magnetic field—**H**—may also be obtained but knowledge of the three electric field components is sufficient to calculate the **H**-field (and vice versa) through equation (3.3) (or Equation (3.4)).

Equation (3.7) may be written in a more familiar form by using the vector identity

$$\nabla\times\nabla = -\nabla^2+\nabla(\nabla\cdot)$$

whence Equation (3.7) becomes

$$\nabla^2\mathbf{E}-\nabla(\nabla\cdot\mathbf{E}) = -\omega^2\mu_0\varepsilon_0\bar{\varepsilon}_r\mathbf{E} \tag{3.8}$$

where $\bar{\varepsilon}_r$ is the relative permittivity tensor—in the isotropic case $\bar{\varepsilon}_r = n^2$, the refractive index squared.

Using the replacement $\frac{\partial}{\partial z} = i\beta$ equation (3.8) may be written componentwise as

$$\begin{pmatrix} \frac{\partial^2}{\partial y^2} - \beta^2 & -\frac{\partial^2}{\partial x \partial y} & -i\beta\frac{\partial}{\partial x} \\ -\frac{\partial^2}{\partial x \partial y} & \frac{\partial^2}{\partial x^2} - \beta^2 & -i\beta\frac{\partial}{\partial y} \\ -i\beta\frac{\partial}{\partial x} & -i\beta\frac{\partial}{\partial y} & \frac{\partial^2}{\partial x^2} + \frac{\partial^2}{\partial y^2} \end{pmatrix} \begin{pmatrix} E_x \\ E_y \\ E_z \end{pmatrix} = -\omega^2 \mu_0 \varepsilon_0 \bar{\varepsilon}_r \begin{pmatrix} E_x \\ E_y \\ E_z \end{pmatrix} \tag{3.9}$$

Introducing a change of length scale by $X = \beta x$ and $Y = \beta y$ reduces Equation (3.9) to

$$\begin{pmatrix} \frac{\partial^2}{\partial Y^2} - 1 & -\frac{\partial^2}{\partial X \partial Y} & -i\frac{\partial}{\partial X} \\ -\frac{\partial^2}{\partial X \partial Y} & \frac{\partial^2}{\partial X^2} - 1 & -i\frac{\partial}{\partial Y} \\ -i\frac{\partial}{\partial X} & -i\frac{\partial}{\partial Y} & \frac{\partial^2}{\partial X^2} + \frac{\partial^2}{\partial Y^2} \end{pmatrix} \begin{pmatrix} E_x \\ E_y \\ E_z \end{pmatrix} = -W^2 \bar{\varepsilon}_r \begin{pmatrix} E_x \\ E_y \\ E_z \end{pmatrix} \tag{3.10}$$

where $W^2 = \frac{\omega^2}{\beta^2 c^2}$ is the desired eigenvalue and is constrained by the condition $1/n_{co} \leq W \leq 1/n_{cl}$ with n_{cl} the minimum cladding refractive index and n_{co} the maximum core refractive index.

The divergence equation $\nabla \cdot \mathbf{D} = 0$ is automatically satisfied for all non-zero values of ω.

The only boundary condition imposed is that the electric field vanish at infinity limiting the treatment to permittivity distributions that are smoothly varying.

If, instead of scaling length by β, lengths had been scaled by k—the free space wavenumber—as in the scalar method described in the previous chapter an eigenproblem containing the eigenvalue both linearly and quadratically is obtained. Such eigenproblems are not fully understood from the numerical standpoint.

Multiplying Equation (3.10) from the left by $\mathbf{E}^H$ reveals that the differential operator is positive definite since $\mathbf{E}^H \bar{\varepsilon}_r \mathbf{E}$ is proportional to the field energy.

The solution of Equation (3.10) by numerical means is hampered by the lack of high quality Hermitian generalised eigenproblem codes and so the problem must be reduced to real form while still maintaining as much generality and symmetry as possible.

It is convenient to adopt the convention that the transverse components of $\mathbf{E}$—(E_x, E_y)—are real while E_z is pure imaginary. By demanding that the displacement vector $\mathbf{D} = \varepsilon\mathbf{E}$ also has this structure the permittivity tensor is forced to have the form

$$\varepsilon = \begin{pmatrix} \varepsilon_{11} & \varepsilon_{12} & 0 \\ \varepsilon_{21} & \varepsilon_{22} & 0 \\ 0 & 0 & \varepsilon_{33} \end{pmatrix} \tag{3.11}$$

if it is to be all real, i.e., there can be no coupling between the transverse components and the z-component. Physically, a tensor of this form describes a lossless

medium in which one of the principal axes of the permittivity tensor is aligned with the z-axis; a not unreasonable restriction given the geometry of an optical fibre [69].

With the permittivity tensor having the form shown in equation (3.11) and the electric field components having the real-imaginary structure stated above a simple unitary transformation via

$$U = \begin{pmatrix} 1 & 0 & 0 \\ 0 & 1 & 0 \\ 0 & 0 & -i \end{pmatrix} \tag{3.12}$$

reduces the wave equation to the following form

$$\begin{pmatrix} \frac{\partial^2}{\partial Y^2} - 1 & -\frac{\partial^2}{\partial X \partial Y} & -\frac{\partial}{\partial X} \\ -\frac{\partial^2}{\partial X \partial Y} & \frac{\partial^2}{\partial X^2} - 1 & -\frac{\partial}{\partial Y} \\ \frac{\partial}{\partial X} & \frac{\partial}{\partial Y} & \frac{\partial^2}{\partial X^2} + \frac{\partial^2}{\partial Y^2} \end{pmatrix} \begin{pmatrix} E_x \\ E_y \\ iE_z \end{pmatrix} = -W^2 \bar{\varepsilon}_r \begin{pmatrix} E_x \\ E_y \\ iE_z \end{pmatrix} \tag{3.13}$$

where E_x, E_y and iE_z are all real.

Equivalently Equation (3.10) can be converted into a 6×6 real problem by using standard techniques described in [70] whence the operator matrix becomes

$$M = \left(\begin{array}{ccc|ccc} t_1 & t_2 & 0 & 0 & 0 & Im(t_3) \\ t_2^T & t_4 & 0 & 0 & 0 & Im(t_5) \\ 0 & 0 & t_6 & Im(t_3^*) & Im(t_5^*) & 0 \\ \hline 0 & 0 & -Im(t_3) & t_1 & t_2 & 0 \\ 0 & 0 & -Im(t_5) & t_2^T & t_4 & 0 \\ -Im(t_3^*) & -Im(t_5^*) & 0 & 0 & 0 & t_6 \end{array} \right) \tag{3.14}$$

where the t_i's map to the elements of the left hand side matrix. Notice that the symmetric permutation row 6 $\leftrightarrow$ row 3 and column 3 $\leftrightarrow$ column 6 converts the 6×6 system into two disjoint 3×3 systems provided the permittivity tensor transforms like the operator matrix under the permutation described above which it does if and only if it has the structure shown in Equation (3.11).

The infinite cross-section of the waveguide is mapped into the unit square $(-\frac{1}{2}, \frac{1}{2}) \times (-\frac{1}{2}, \frac{1}{2})$ by means of a non-linear transformation

$$X = \varphi_1(u_1) \tag{3.15}$$

$$Y = \varphi_2(u_2) \tag{3.16}$$

where φ_1 and φ_2 are monotonically increasing functions of u_1 and u_2 that are at least twice differentiable, respectively. Consequently, the Jacobian matrix

$$J_m = \begin{pmatrix} \frac{\partial X}{\partial u_1} & 0 \\ 0 & \frac{\partial X}{\partial u_2} \end{pmatrix} \tag{3.17}$$

is positive definite because

$$J \equiv \det(J_m) = \frac{\partial X}{\partial u_1}\frac{\partial Y}{\partial u_2} \tag{3.18}$$

is always positive.

Applying the non-linear transformation to Equation (3.13) and multiplying throughout by $-\mathrm{diag}(J,J,J)$ gives

$$\begin{pmatrix} J - \frac{\partial}{\partial u_2}\left[\frac{\partial X}{\partial u_1}\frac{\partial u_2}{\partial Y}\right]\frac{\partial}{\partial u_2} & \frac{\partial^2}{\partial u_1 \partial u_2} & \frac{\partial Y}{\partial u_2}\frac{\partial}{\partial u_1} \\ \frac{\partial^2}{\partial u_1 \partial u_2} & J - \frac{\partial}{\partial u_1}\left[\frac{\partial Y}{\partial u_2}\frac{\partial u_1}{\partial X}\right]\frac{\partial}{\partial u_1} & \frac{\partial X}{\partial u_1}\frac{\partial}{\partial u_2} \\ -\frac{\partial Y}{\partial u_2}\frac{\partial}{\partial u_1} & -\frac{\partial X}{\partial u_1}\frac{\partial}{\partial u_2} & t_9(u_1,u_2) \end{pmatrix} \mathbf{E} = W^2 \bar{\varepsilon}_J \mathbf{E} \tag{3.19}$$

where

$$t_9(u_1,u_2) = -\left(\frac{\partial}{\partial u_1}\left[\frac{\partial Y}{\partial u_2}\frac{\partial u_1}{\partial X}\right]\frac{\partial}{\partial u_1} + \frac{\partial}{\partial u_2}\left[\frac{\partial X}{\partial u_1}\frac{\partial u_2}{\partial Y}\right]\frac{\partial}{\partial u_2}\right)$$

and $\bar{\varepsilon}_J = \mathrm{diag}(J,J,J)\bar{\varepsilon}_r$.

The magnetic field may be obtained directly from equation (3.3) with appropriate transformation into configuration space.

3.3 Numerical Method

Equation (3.19) is discretized on a regular grid in transform space with care being taken to ensure that the resulting matrix representation is symmetric.

Using the same notation as in the previous chapter, *viz*

$$\Gamma_1 = \frac{1}{h}\begin{bmatrix} -1 & 1 & 0 & 0 & & & \\ 0 & -1 & 1 & 0 & & \cdots & \\ & & -1 & 1 & & & \\ & & & & & & \\ & & & & -1 & 1 & 0 \\ & \cdots & & & 0 & -1 & 1 \\ & & & & 0 & 0 & -1 \end{bmatrix}. \tag{3.20}$$

is the forward finite difference operator acting only on functions of u_1 where $h = 1/N$ is the mesh spacing and N an integer with the grid having $(N-1)\times(N-1)$ interior points. Then $(-\Gamma_1)^T$ is the backward finite difference operator acting only on functions of u_1. Similarly, Γ_2 and $(-\Gamma_2)^T$ are defined as the forward and

backward finite difference operators acting on functions of u_2 only respectively. Then:

$$\begin{aligned}
J - \frac{\partial}{\partial u_2}\left[\frac{\partial X}{\partial u_1}\frac{\partial u_2}{\partial Y}\right]\frac{\partial}{\partial u_2} &\rightarrow J - \frac{1}{2}[(-\Gamma_2)^T g_2 \Gamma_2 + \Gamma_2^T g_2(-\Gamma_2)] \\
\frac{\partial^2}{\partial u_1 \partial u_2} &\rightarrow \frac{1}{4}[(\Gamma_1 + (-\Gamma_1)^T)(\Gamma_2 + (-\Gamma_2)^T)] \\
\frac{\partial Y}{\partial u_2}\frac{\partial}{\partial u_1} &\rightarrow \frac{1}{2}\varphi_1'[\Gamma_1 + (-\Gamma_1)^T] \\
J - \frac{\partial}{\partial u_1}\left[\frac{\partial Y}{\partial u_2}\frac{\partial u_1}{\partial X}\right]\frac{\partial}{\partial u_1} &\rightarrow J - \frac{1}{2}[(-\Gamma_1)^T g_1 \Gamma_1 + \Gamma_1^T g_1(-\Gamma_1)] \\
\frac{\partial X}{\partial u_1}\frac{\partial}{\partial u_2} &\rightarrow \frac{1}{2}\varphi_2'[\Gamma_2 + (-\Gamma_2)^T] \\
\frac{\partial}{\partial u_1}\left[\frac{\partial Y}{\partial u_2}\frac{\partial u_1}{\partial X}\right]\frac{\partial}{\partial u_1} + \frac{\partial}{\partial u_2}\left[\frac{\partial X}{\partial u_1}\frac{\partial u_2}{\partial Y}\right]\frac{\partial}{\partial u_2} &\rightarrow \frac{1}{2}\left[(-\Gamma_1)^T g_1 \Gamma_1 + \Gamma_1^T g_1(-\Gamma_1)\right] \\
&\quad + \frac{1}{2}\left[(-\Gamma_2)^T g_2 \Gamma_2 + \Gamma_2^T g_2(-\Gamma_2)\right]
\end{aligned}$$

With these replacements the operator matrix is fully symmetric and has the non-zero structure shown in Figure 3.1.

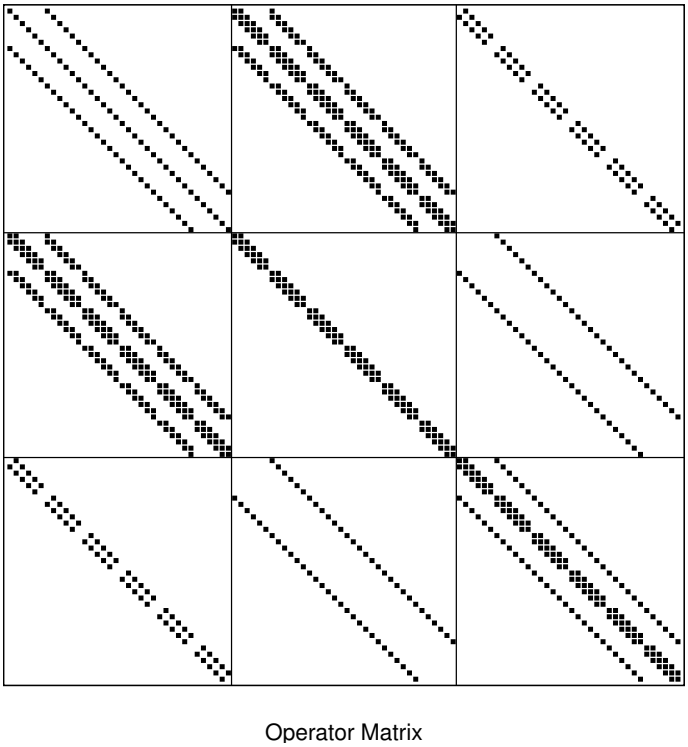

Figure 3.1: The non-zero structure of the operator matrix

As may be seen, the operator matrix has a distinctive block structure which is not exploited in solving the resulting algebraic eigenproblem. However, the manifest symmetric structure is utilised to minimize the overall storage requirements.

In final numerical form Equation (3.19) has the symbolic form

$$\mathscr{O}\mathbf{E} = W^2 \varepsilon_J \mathbf{E} \tag{3.21}$$

where $\mathscr{O}$ is the numerical representation of the operator matrix and $\varepsilon_J = \text{diag}(J,J,J)\varepsilon$ where J is defined in equation (3.18).

In order to gain some feeling for the spectrum of Equation (3.21) consider counting the modes of the scalar wave equation discretized on the same mesh. Notice that each mode of the scalar wave equation will in general split into two polarisation degenerate modes and so will account for 2 degrees of freedom per interior point, i.e. $2(N-1)^2$ modes, leaving an as yet unaccounted for $(N-1)^2$ modes. The additional modes are attributed to zero frequency solutions of the wave equation arising from the neglect of the divergence equation. Indeed, for N small (typically less than 30) the spectrum is clearly split into two groups. One third of the eigenvalues lying near zero and the smallest of the upper group corresponding to the fundamental mode. It follows that we must solve an interior eigenproblem in order to find the fundamental mode.

As N is increased the gap between the two groups of eigenvalues diminishes and there is a blurring together giving rise to the what are conventionally called 'spurious' modes—modes that lie within the allowed range of bound modes, satisfy the boundary conditions but are not consistent with the divergence equation.

3.3.1 Rayleigh Quotient Iteration

Due to the large number of spurious modes Equation (3.21) was not solved using the Lanczos method, as in the previous chapter, although the BCSlib code has no difficulties finding interior eigenvalues. Postprocessing to eliminate the spurious modes was simply too computationally time consuming.

In order to avoid this postprocessing step Rayleigh quotient iteration (RQI) [59] was used. The method is presented algorithmically below.

Choose starting vector $\mathbf{E}_0$

Choose starting eigenvalue W_0^2

While not converged do

Solve $(\mathscr{O} - W_n^2 \varepsilon_J)\mathbf{E}_{n+1} = \varepsilon_J \mathbf{E}_n$

Compute $W_{n+1}^2 = \frac{\mathbf{E}_{n+1}^T \mathscr{O} \mathbf{E}_{n+1}}{\mathbf{E}_{n+1}^T \varepsilon_J \mathbf{E}_{n+1}}$

Compute residual and check convergence condition

Normalise $\mathbf{E}_{n+1}$ in the ε_J-norm

end while

The proof that the above algorithm converges is standard and may be found in [70].

The residual, r, is defined by

$$r = \frac{\mathbf{E}_{n+1}^T(\mathscr{O} - W_{n+1}^2)\mathbf{E}_{n+1}}{\mathbf{E}_{n+1}^T\varepsilon_J\mathbf{E}_{n+1}} \tag{3.22}$$

and the convergence condition, $r \leq 1.0 \times 10^{-18}$, ensures that we have the eigenvalue for a given mesh to about 10 significant figures and the electric field to about 5 significant figures. The fields are normalised in the ε_J-norm which is natural for an eigenproblem of this form.

The rate of convergence under ideal conditions is cubic (i.e., the number of digits in the eigenvalue triples at each RQI step) and it is almost always guaranteed to converge to an eigenvalue. These results are proved in Parlett [59] for the standard eigenproblem and the extension to the generalised problem is trivial because $\mathscr{O}$ and ε_J are positive definite and any positive definite generalised eigenproblem can be rewritten as a standard eigenproblem via the Cholesky factorization. From the practical point of view such a factorization is usually not necessary or desirable because the product of a lower triangular matrix with the operator matrix will almost certainly be dense.

The downside of the method is that an indefinite linear system (i.e., the left hand side matrix $\mathscr{O} - W_n^2\varepsilon_J$ possesses both positive and negative eigenvalues) must be solved at each iteration step and it is the efficiency of solving the system that dominates overall performance.

Notice that as W_n^2 approaches an eigenvalue of the system the matrix $\mathscr{O} - W_n^2\varepsilon_J$ becomes increasingly singular and the condition number of the system becomes very large thus limiting the choice of methods available to solve the system. Indeed, iterative methods are largely ruled out because of the difficulty of finding preconditioners for near-singular systems. Direct sparse solution methods overcome these problems that are inevitable with iterative methods and the method used here is the multifrontal code available as part of the BCSlib-ext package from Boeing Computer Services. The advantage of this code is that the matrix factorizations can be stored out-of-core and so very large systems can be solved in relatively small amounts of physical memory.

Even direct methods will be hampered by matrices that are near numerical singularity but the eigenextraction can proceed primarily because the error associated

with the solution of the linear system is almost orthogonal to the space spanned by the eigenvectors associated with the eigenvalue W^2.

The eigenpair (i.e., eigenvalue-eigenvector pair) that the RQI scheme converges to is largely set by the choice of starting vector and estimated eigenvalue so they must be chosen carefully. Two techniques were used in practice. Firstly, the problem can be solved using the scalar method described in Chapter 2 and the resultant field and eigenvalue used as initial inputs. Alternatively, the problem can be solved on an extremely coarse grid where the number of eigenvalues is relatively small. In either case results from coarse grids were used to seed the calculation as the mesh size was refined. This is in some sense akin to a multigrid method although user intervention is required when proceeding to the finer grid.

Polarisation degeneracy for problems with circularly symmetric cores can be split in two ways: either the scaling functions $\varphi_1(u_1)$ can be chosen to be slightly dissimilar to $\varphi_2(u_2)$ thus breaking the symmetry in configuration space, or knowledge of modal symmetry can be used. Both methods are viable. The first technique proved extremely useful for testing the code because both the eigenvalues corresponding to the polarisation degenerate modes should converge to the same value when extrapolated using the technique described in the previous chapter.

It is important to note that the formulation requires the specification of the propagation constant β and returns k (via W^2) as the eigenvalue. This is a somewhat unnatural formulation because the propagation constant is usually required at a given operating wavelength. An iterative procedure over the value of β is used to zero in on the wanted operating wavelength. In general, an operating wavelength, λ, is chosen and used to set the cladding index via a Sellmeier expansion. An effective index n_e^0 is also chosen and used to compute the initial propagation constant via $\beta_0 = n_e^0 2\pi/\lambda$. The value of W returned from the numerical solution is then used to set the value of $n_e^1 = 1/W$ and hence to set $\beta_1 = n_e^1 2\pi/\lambda$. The refractive index distribution is also updated due to lengths being scaled by β. Iteration in this manner proceeds until $|n_e^m - n_e^{m-1}|$ is sufficiently small. The computational cost of the additional iterations can be amortized by updating n_e at every RQI step. The overall problem solved may therefore be viewed as a nonlinear generalized real symmetric eigenproblem and the solution method as a form of fixed point iteration in which the function evaluation is an eigenvalue extraction accompanied by a recalculation of the refractive index distribution.

3.4 Verification

It must be emphasized that the technique described in this chapter cannot be used to analyse fibres with permittivity distributions that are too steep. The previous statement is deliberately vague but step profiles cannot be handled nor any profile

with a discontinuity, however slight. The infinite parabolic profile again presents itself as the perfect candidate for initial trial.

The profile used is identical to that in the previous chapter (Equation 2.16). It is important to note that although all of the modes of the infinite parabolic profile are bound; analytic solutions of the vector wave equation are known only for the transverse electric (TE) modes [20] so the solutions sought are genuinely vectorial. The TE-modes are labelled by a single integer, n, that describes the azimuthal dependence of the electric field components and have E_z strictly zero. Attention is focussed on the TE_{01} mode for which the analytic value of W^2 is 0.447939601 using results from [20].

For the vector solver the value of the propagation constant β is required as input and the square of the reciprocal of the effective index is returned as the eigenvalue. For agreement with the discussion in Chapter 2 the wavelength is set at 1.3μm and the input value of n_e chosen as 1.494136484. The extrapolation table produced by running the same problem on increasingly finer meshes and extrapolating to zero mesh size using the technique described previously is shown in Table 3.1.

N	W^2			
80	0.44793382377			
		0.44794474218		
90	0.44793503692		0.44793959453	
		0.44794371265		0.44793960320
100	0.44793590450		0.44793959690	
		0.44794296433		
110	0.44793654630			

Table 3.1: Extrapolation table for TE_{01} mode of infinite parabolic profile

The final numerical result of 0.447939603 differs by 2 in the ninth place from the analytic result. The x- and y-components of the electric field are shown in Figure 3.2 and the intensity distribution in Figure 3.3. All plots are shown in transformed coordinates.

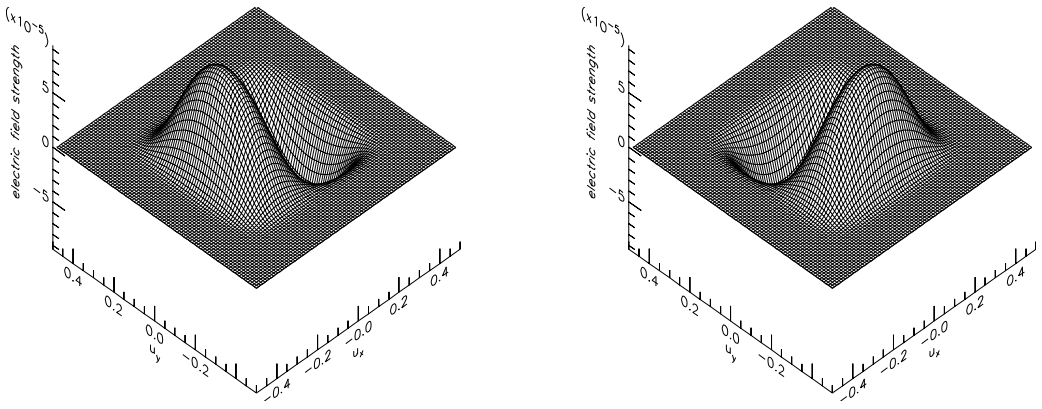

Figure 3.2: x- and y-components of TE_{01} mode of infinite parabolic profile

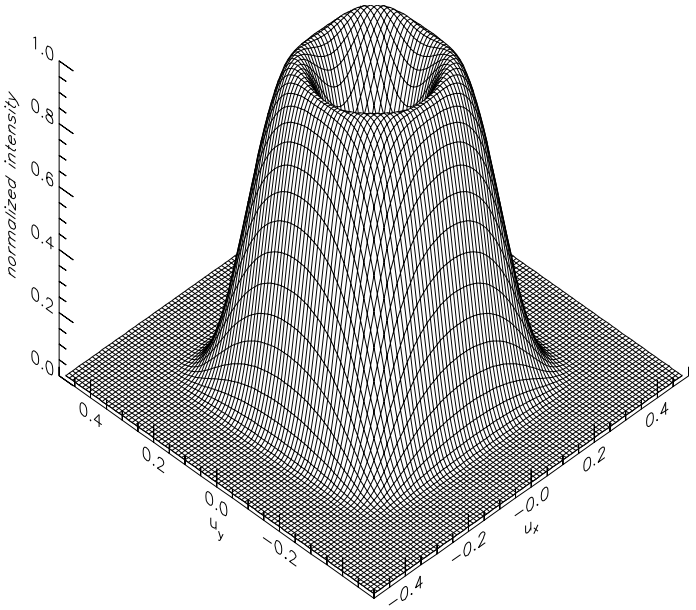

Figure 3.3: Intensity of TE_{01} mode of infinite parabolic profile

An interesting test is afforded by noting that the infinite parabolic profile being used is weakly guiding so agreement between the vector and scalar calculation is expected for the fundamental (polarisation degenerate) modes (as well as for the other modes).

The value of the propagation constant used was that obtained as the solution of the scalar wave equation for the fundamental mode in the previous chapter. The

resulting value of W^2 is 0.44618689 as may be seen from the extrapolation table (Table 3.2). This corresponds to an effective index of 1.497068241 compared to the scalar result of 1.49707111 a difference of 2.9×10^{-6} in agreement with the perturbation theory result that the difference in scalar and vector propagation constants is of order $\Delta^{\frac{3}{2}} = 10^{-6}$ [20].

N	W^2			
80	0.44618385889			
		0.44618958488		
90	0.44618449511		0.44618688425	
		0.44618904476		0.44618688974
100	0.44618495008		0.44618688575	
		0.44618865221		
110	0.44618528663			

Table 3.2: Extrapolation table for x-polarised fundamental mode of infinite parabolic profile

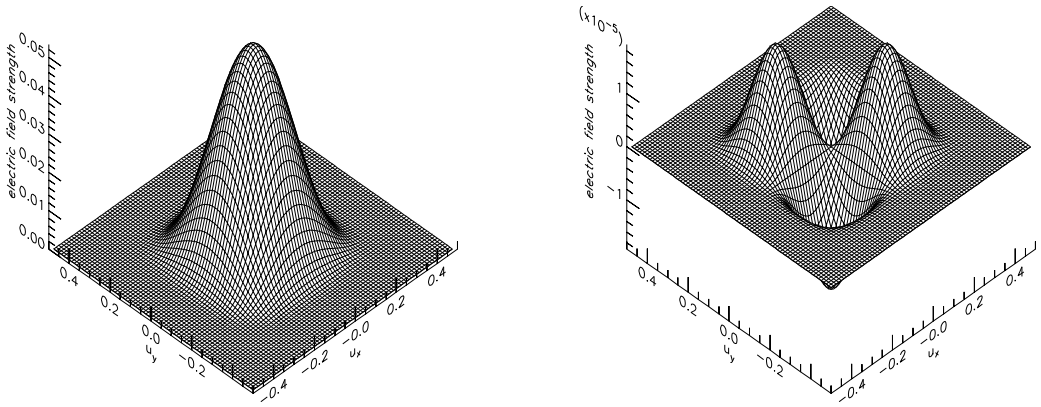

Figure 3.4: x- and y-components of x-polarised fundamental mode of infinite parabolic profile

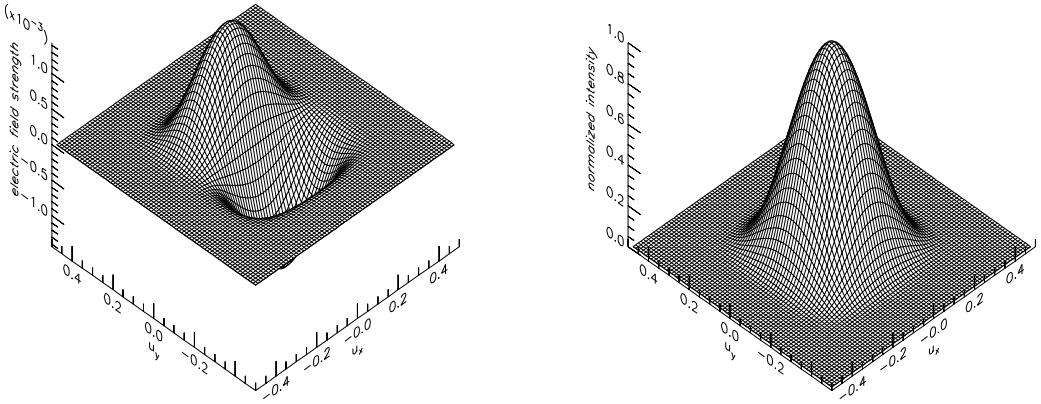

Figure 3.5: z-component and intensity of x-polarised fundamental mode of infinite parabolic profile

The field plots of the x-polarised fundamental mode are shown in Figures 3.4 and 3.5. The field components graphically show the often unappreciated difference in magnitude between the major field component (corresponding to the predominant polarisation direction) and the the minor field component (the component orthogonal to the predominant polarisation direction) and the z-component. Indeed, as expected [20] the minor field is down by a factor of $\Delta = 10^{-4}$ and the z-component is down by a factor of $\Delta^{\frac{1}{2}} = 10^{-2}$ compared to the major field. The vector direction of the fields confirm the results of Zheng, Henry and Snyder [71].

3.5 Example Applications

In this section three non-trivial applications are shown. Each forms the basis for material that will be discussed more fully in subsequent chapters.

It should be noted that the permittivity distributions for the vector program are usually represented by analytic functions. Preform or fibre profiler data is too noisy to be used directly. One solution which has had some success is to low pass filter the data using a Gaussian windowing function in Fourier transform space.

3.5.1 Single core—Preform data

The profile analyzed in this section is identical to that used in Section 2.5.2 with the exception that smoothing was carried out by fast Fourier transforming and applying a Gaussian windowing or filter function. The filter function applied to

the transformed data is

$$F(f) = \exp\left(-\frac{f^2}{\sigma^2 f_m^2}\right) \tag{3.23}$$

where σ is the smoothing parameter and f_m is the maximum frequency representable by the FFT. The full-width at half-maximum is

$$\text{FWHM} = 2\sigma f_m \left[\ln(2)\right]^{\frac{1}{2}} \tag{3.24}$$

so spatial frequencies higher than $\sigma f_m \left[\ln(2)\right]^{\frac{1}{2}}$ are strongly attenuated.

The raw and smoothed data are shown in Figure 3.6. The smoothing parameter was set to 0.08 and $f_m = 12.56\mu\text{m}^{-1}$. The cladding index was set to the refractive index value of fused silica at 1.3μm.

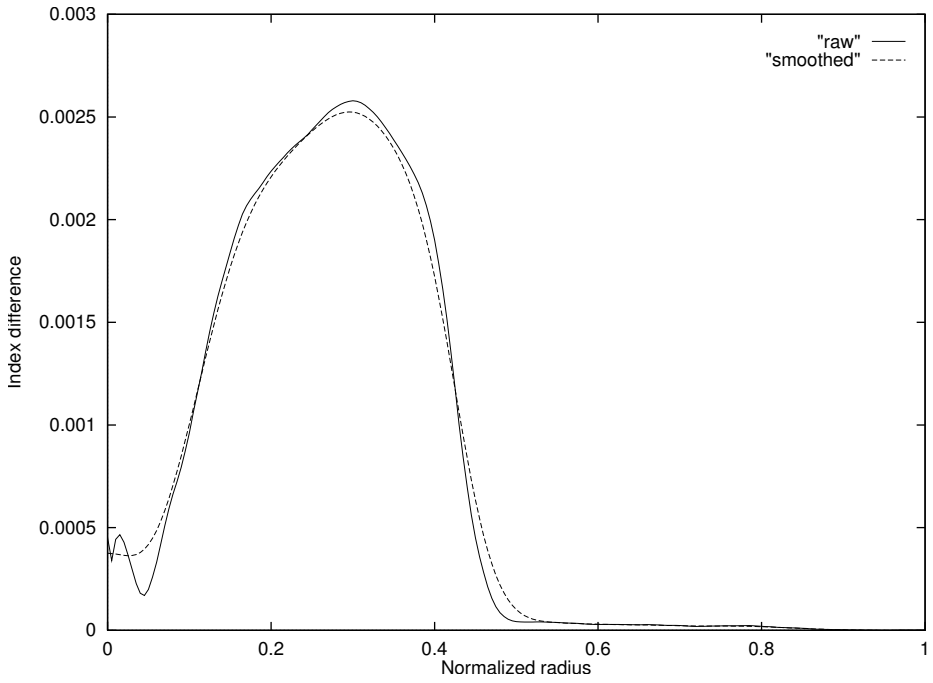

Figure 3.6: Original and smoothed refractive index profiles

The initial value of n_e was chosen to be 1.445 based on the scalar result for the non-smoothed profile discussed previously. The eigenvalue estimates were improved by extrapolation because the profile is smooth. The final computed value of W^2 is 0.47726824, correct to seven figures. Thus the effective index of the fundamental mode is 1.4475006 at 1.3μm.

The internal evidence for accuracy is afforded by the small size of the residual (defined in Equation (3.22)), $r = 1.3 \times 10^{-22}$ on a 120×120 mesh, and the consistency of the extrapolation table (see Table 3.3).

N	W^2				
70	0.47726663585				
		0.47726970987			
80	0.47726702011		0.47726821238		
		0.47726937710		0.47726827009	
90	0.47726728199		0.47726822970		0.47726824174
		0.47726914762		0.47726825828	
100	0.47726746856		0.47726823922		
		0.47726892052			
120	0.47726771055				

Table 3.3: Extrapolation table for smoothed real profile

Field plots of the x-polarised fundamental mode are shown in Figures 3.7 and 3.8.

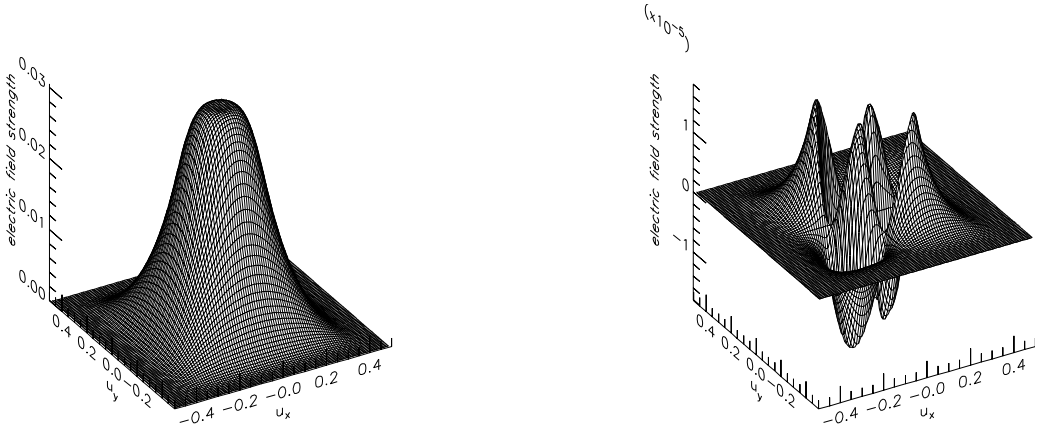

Figure 3.7: x- and y-components of x-polarised fundamental mode of smoothed profile

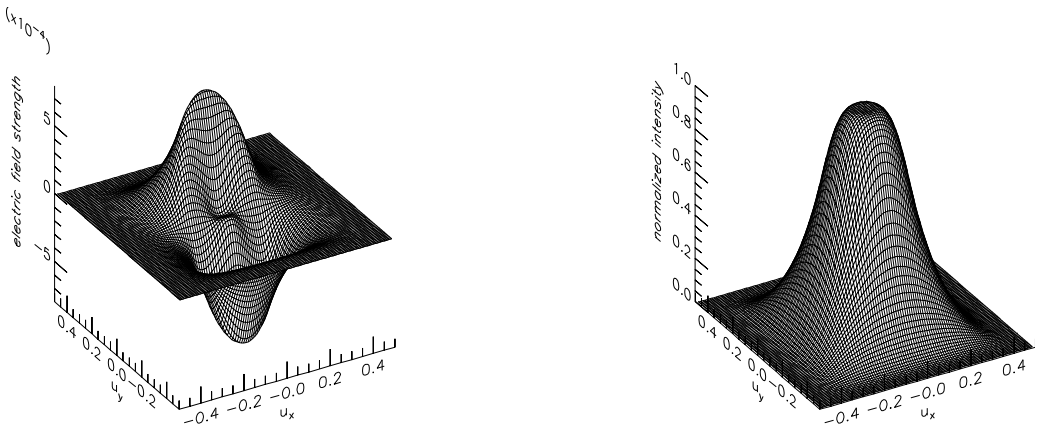

Figure 3.8: z-component and intensity of x-polarised fundamental mode of smoothed profile

With reference to Figures 3.7 and 3.4 it is apparent that the minor field component has considerably more structure than the minor field of the fundamental mode of the infinite parabolic profile. This additional structure is present in the minor field component of all fibres with a central dip in the refractive index profile and it is at least qualitatively possible to infer the refractive index distribution from the minor field even in cases when the major field component shows no visible central depression.

3.5.2 Twin-core Fibre

The twin-core fibre analysed is identical to that treated in Section 2.5.1 using the scalar solver. The nominal operating wavelength was 1.3μm and the cladding index set to 1.457.

In this case four modes were examined—the two polarisation modes corresponding to the scalar even and odd supermodes. Results are shown in Table 3.4 where $1/W$ has been identified as the effective index.

Mode	Effective index
even x	1.4604662
even y	1.4604662
odd x	1.4604411
odd y	1.4604411

Table 3.4: Effective index values for x- and y-polarised even and odd supermodes of twin-core fibre

The breaking of polarisation degeneracy is not evident because the fibre is weakly guiding. The beat length, $z_b = 2\pi/|\beta_1 - \beta_2|$, is 51.8mm in good agreement with the scalar result of 52mm.

The fields of the x-polarised even supermode are shown in Figures 3.9 and 3.10. Again, the additional structure due to the central dip in the refractive index distributions of the constitutive cores is clearly visible.

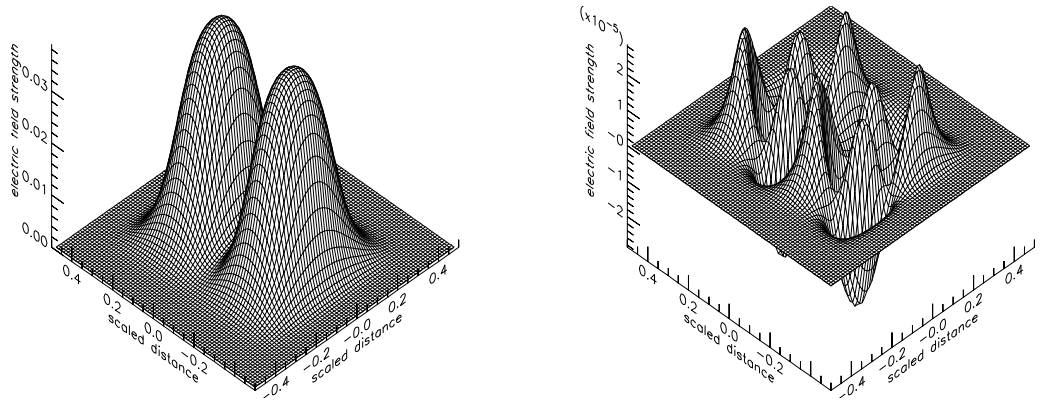

Figure 3.9: x- and y-components of x-polarised even supermode of twin-core fibre

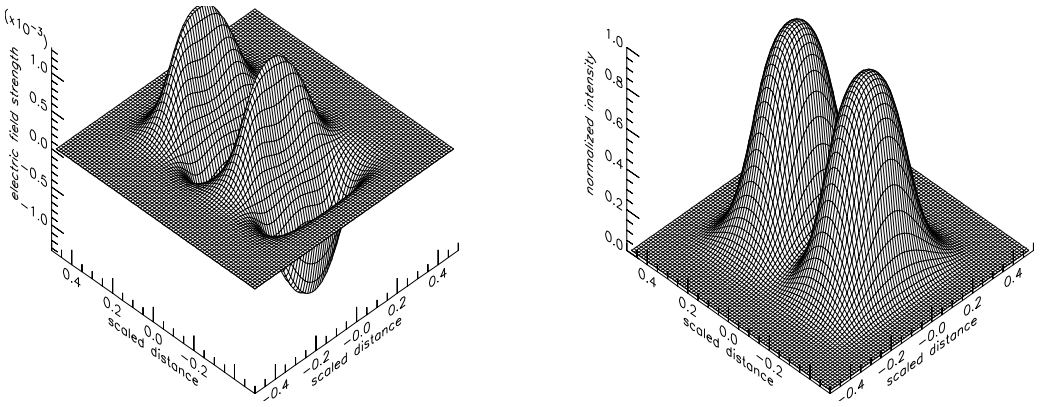

Figure 3.10: z-component and intensity of x-polarised even supermode of twin-core fibre

3.5.3 Biaxial Fibre

In a crystalline material it is always possible to find a set of three orthogonal axes in which the permittivity tensor is everywhere diagonal. These axes are termed the principal axes of the permittivity tensor and define the optical axes of the crystal,

that is, directions in which the phase velocity of the two linearly polarised modes are equal. In an optical fibre such a global coordinate system cannot, in general, be found.

The disposition of the elements of the diagonalized permittivity tensor is used to optically classify the material. If all three elements are different the material is termed biaxial and one of the principal axes is aligned with a symmetry axis of the crystal. The direction of the other two principal axes is arbitrary in the plane perpendicular to the first. In the case of a fibre it is convenient to take the z-axis (that is the direction of light propagation) as the axis of symmetry and the other two principal axes as lying along the transverse coordinate axes. Such a permittivity tensor may be used as a model of a double bow-tie [72] or PANDA [73] fibre. Interestingly, no closed form solutions can be found for fibres composed of biaxial media [20].

The elements of the permittivity tensor are defined by

$$\begin{aligned} \varepsilon_{11} &= n_{\text{cl}} + \Delta Q(x,a) \\ \varepsilon_{22} &= n_{\text{cl}} + \Delta Q(y,a) \\ \varepsilon_{33} &= n_{\text{cl}} + \Delta Q(x,a) + \Delta Q(y,a) \end{aligned} \tag{3.25}$$

where

$$\begin{aligned} Q(x,a) &= \exp\left[-\left(\frac{r_x^+}{a}\right)^4\right] + \exp\left[-\left(\frac{r_x^-}{a}\right)^4\right], \\ Q(y,a) &= \exp\left[-\left(\frac{r_y^+}{a}\right)^4\right] + \exp\left[-\left(\frac{r_y^-}{a}\right)^4\right], \end{aligned}$$

$$\begin{aligned} r_x^{\pm} &= \left[(x \mp b)^2 + y^2\right]^{\frac{1}{2}}, \\ r_y^{\pm} &= \left[x^2 + (y \mp b)^2\right]^{\frac{1}{2}}, \end{aligned}$$

$a = 3.0\mu\text{m}$, $b = 5.5\mu\text{m}$, $n_{cl} = 1.457$ and $\Delta = 0.002$. Calculations were carried out at a wavelength of $1.3\mu\text{m}$.

The x- and y-polarised modes of a fibre with the permittivity tensor given in Equation (3.25) will have equal propagation constants and the fields will simply be 90° rotations of each other because the x-polarised mode will be influenced primarily by ε_{11} and the y-polarised mode primarily by ε_{22} (both of course see ε_{33} equally). The value of the effective index computed on a 100×100 finite difference grid is 1.457190 accurate to six significant figures.

The x- and y-components of the x-polarised fundamental mode electric field are shown in Figure 3.11.

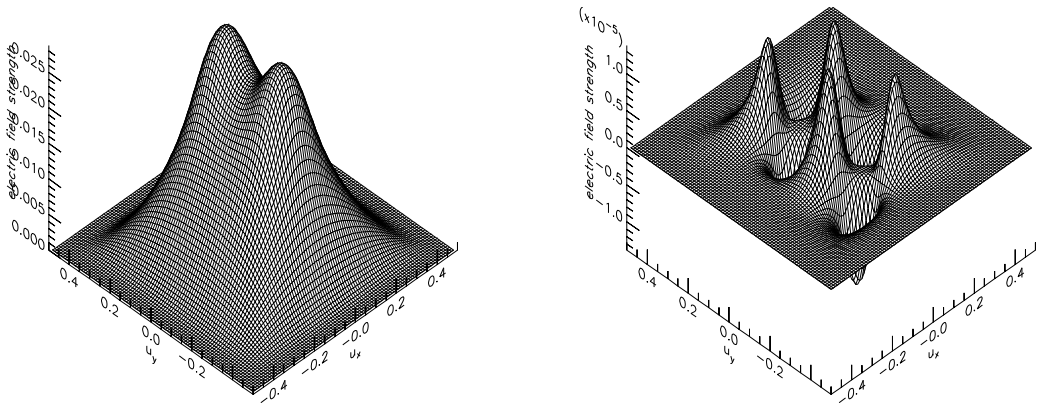

Figure 3.11: x- and y-components of x-polarised fundamental mode of biaxial fibre

For completeness, the x- and y-components of the x-polarised fundamental mode magnetic field are shown in Figure 3.12.

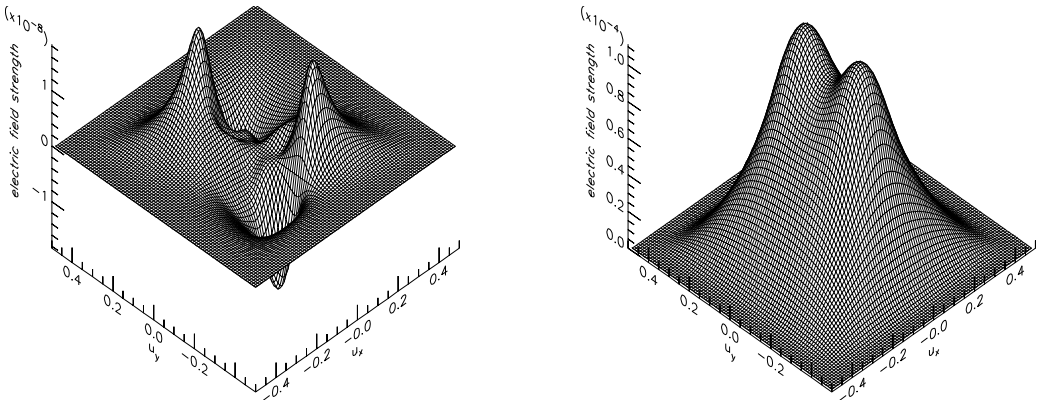

Figure 3.12: z-component and intensity of x-polarised fundamental mode of biaxial fibre

3.6 Conclusion

In this chapter a general finite difference method for the solution of the vector wave equation in an optical fibre has been presented and examples indicating the applicability of the method to a representatively wide range of problems exhibited.

Despite the fact that most fibres have circular symmetry the requirement to handle arbitrary azimuthal variation of both permittivity distributions and field

components justifies the decision to use Cartesian coordinates.

The program is sufficiently memory and CPU intensive that a well equipped workstation with at least 64 Mb of RAM and performance in the 10s of megaflops is required for adequate performance (a 100×100 grid problem solved in 10 minutes). However, with hardware prices falling and performance increasing at a rapid rate such systems are now commonly available on the desktop.

Chapter 4

Circularly Birefringent Optical Fibres

4.1 Introduction

Practical design and manufacture of circularly birefringent optical fibres has long been a goal of the optical fibre community. Such fibres have immediate application in optical fibre sensors [74], communication systems and devices.

A consistent set of design rules for such fibres has only recently been developed firstly for weakly guiding fibres [75] and extended to the strongly guided (i.e, large core-cladding index difference) case by Bassett and Shanahan [76]. An outline of the theory will be presented below and the weak guidance approach is shown to be consistent with the full vector treatment.

The theory is applied firstly to a model of a circularly birefringent fibre which gives clear indications of the desired properties of the permittivity tensor and then to a practical structure that is shown, theoretically, to exhibit useful levels of circular birefringence.

4.2 Circular Birefringence

A material is said to be circularly birefringent if left and right hand circularly polarised light propagate with different phase velocities, that is, if the degeneracy between left and right hand circularly polarised light is broken in the medium. Equivalently, the left and right hand circular polarisations 'see' different refractive indices, n_l and n_r respectively.

Consider a linearly polarised plane wave incident on a circularly birefringent medium. Such a wave may be written as the sum of left and right circularly

polarised components. In terms of the Jones' calculus (see [77] for example)

$$E_0 \begin{bmatrix} 1 \\ 0 \end{bmatrix} = \frac{E_0}{2} \begin{bmatrix} 1 \\ -i \end{bmatrix} + \frac{E_0}{2} \begin{bmatrix} 1 \\ i \end{bmatrix} \tag{4.1}$$

where the left hand side of Equation (4.1) represents linearly (x-) polarised light and the terms on the right represent right and left circularly polarised light respectively. After propagating a distance d into the medium the field is given by

$$E = \frac{E_0}{2} \begin{bmatrix} 1 \\ -i \end{bmatrix} \exp(2\pi i n_r d/\lambda) + \frac{E_0}{2} \begin{bmatrix} 1 \\ i \end{bmatrix} \exp(2\pi i n_l d/\lambda) \tag{4.2}$$

where λ is the free space wavelength of the light or, equivalently,

$$E = E_0 \exp(i\psi) \left\{ \begin{bmatrix} 1 \\ 0 \end{bmatrix} \cos\delta + \begin{bmatrix} 0 \\ 1 \end{bmatrix} \sin\delta \right\} \tag{4.3}$$

where

$$\psi = \frac{\pi(n_r + n_l)d}{\lambda} \tag{4.4}$$

and

$$\delta = \frac{\pi(n_r - n_l)d}{\lambda}. \tag{4.5}$$

It is evident from Equation (4.3) that the direction of linear polarisation in the propagated beam has suffered a rotation of δ or a relative phase shift between left and right circular polarisations of 2δ.

The circular birefringence, α, is defined as the phase shift per unit distance. For the case above,

$$\begin{aligned} \alpha &= 2\frac{\delta}{d} \\ &= k(n_r - n_l). \end{aligned} \tag{4.6}$$

In the vast majority of media circular birefringence is swamped by the linear birefringence of the medium, being several orders of magnitude smaller.

In optical fibre parlance the left and right circularly polarised waves have different propagation constants and the beat length is defined by

$$z_b = \left| \frac{2\pi}{\beta_l - \beta_r} \right| \tag{4.7}$$

where β_l and β_r are the propagation constants, $(2\pi/\lambda)n_l$ and $(2\pi/\lambda)n_r$ respectively, corresponding to left and right circularly polarised modes.

The simplest means of producing a circularly birefringent fibre is to helically wind a circularly symmetric standard fibre. Ross [78] observed that the plane of polarisation of linearly polarised light launched into such a structure rotates through an angle, θ (relative to the polarisation direction of the incident light), given by

$$\theta = \int \tau ds \tag{4.8}$$

where τ is the (mathematical) torsion of the helix given by

$$\tau = \mathbf{n} \cdot \frac{d\mathbf{b}}{ds} \tag{4.9}$$

where $\mathbf{n}$ is the unit normal to the helix and $\mathbf{b}$ is the unit normal to the osculating plane (both at a given point P on the helix); and s the arc length. The structure, therefore, exhibits circular birefringence. Indeed, any space curve with non-zero torsion must exhibit circular birefringence.

If a fibre is subjected to torsional stress (twisted) it will exhibit circular birefringence due to the stress-optic effect. However, such torsionally stressed fibres relax shear stress and will suffer mechanical failure before a usable level of circular birefringence is obtained [79]. Assuming 1000 turns per metre (quite close to the fracture limit of silica fibre) the minimum circular birefringence beatlength is $\sim$ 14mm.

A fibre that is spun during the drawing process will not be subject to torsional stress and so will not be subject to direct mechanical failure. It follows that spinning a fibre during drawing and thus introducing helicity may be a practical means of producing a circularly birefringent fibre.

4.3 Bassett's Analysis

Early analyses of spun circularly birefringent fibres based on ray optics [80] are incapable of producing valid predictions as noted by [81]. An accurate analysis is only possible if the form of the fields in the fibre are taken into account. The first such analysis due to Bassett is reviewed here. The analysis is restricted to weakly guiding waveguides and additionally it is assumed that the spin rate is 'adiabatic' that is sufficiently slowly varying so as to allow the use of coupled local-mode theory with only the two polarisation states in the forward propagating fundamental mode being excited [20].

Bassett proceeds by considering the way vector point functions transform under rotation and shows that the coupled local-mode equations for the spun fibre have the standard form

$$-i\frac{dc_{\rightarrow}}{dz} = \beta c_{\rightarrow} - \Gamma_{\rightarrow\rightarrow} c_{\rightarrow} - \Gamma_{\rightarrow\uparrow} c_{\uparrow} \tag{4.10}$$

$$-i\frac{dc_{\uparrow}}{dz} = \beta c_{\uparrow} - \Gamma_{\uparrow\rightarrow}c_{\rightarrow} - \Gamma_{\uparrow\uparrow}c_{\uparrow} \tag{4.11}$$

where the subscripted arrows indicate the polarisation, the c's are the z-dependent local-mode amplitudes and the Γ's are the coupling coefficients.

It is then shown that under conditions of weak guidance Equations (4.10) and (4.11) reduce to

$$-i\frac{dc_{\rightarrow}}{dz} = \beta c_{\rightarrow} - i\frac{2\pi}{p}\gamma c_{\uparrow} \tag{4.12}$$

$$-i\frac{dc_{\uparrow}}{dz} = \beta c_{\uparrow} + i\frac{2\pi}{p}\gamma c_{\rightarrow}, \tag{4.13}$$

where p is the spin-pitch of the spun fibre,

$$\gamma = \frac{\int\int dx\,dy\,\chi_{\rightarrow}\chi_{\uparrow}}{\left(\int\int dx dy\,\chi_{\rightarrow}^2\right)^{1/2}\left(\int\int dx dy\,\chi_{\uparrow}^2\right)^{1/2}} \tag{4.14}$$

and the χ's are the scalar fields. The integrations are carried out over the full cross-section of the fibre.

It is convenient to refer to the expression on the right hand side of equation (4.14) as the overlap integral because it is a direct measure of the overlap of the two polarisation modes. Clearly, it is maximum when $\chi_{\rightarrow} = \chi_{\uparrow}$ and minimum when the two fields are maximally dissimilar.

Bassett then shows that in a fixed frame of reference the two independent solutions of Equations (4.12) and (4.13) exhibit a circular birefringence of

$$\alpha = \frac{4\pi}{p}(1-\gamma) \tag{4.15}$$

and that $0 \leq \gamma \leq 1$. The corresponding beat length, from Equations (4.7) and (4.15), is

$$z_b = \frac{p}{2(1-\gamma)}. \tag{4.16}$$

The fundamental conclusions drawn are that the rotation of the modal polarisation will always lag the rotational pitch of the spun fibre and that in the absence of material birefringence the circular birefringence will be zero because then $\chi_{\uparrow} = \chi_{\rightarrow}$ in the weak guidance approximation.

The vector generalization follows from Equations (4.10) and (4.11) by retaining all vector components. In this case an expression for Γ_{ij} (the i, j range over

$\rightarrow$, $\uparrow$) is derived, yielding

$$\begin{aligned}\Gamma_{ij} &= \frac{-i}{4N_{(i)}N_{(j)}}\int\int dxdy\{e^x_{(i)}(h^x_{(j)}+y\frac{\partial h^y_{(j)}}{\partial x}-x\frac{\partial h^y_{(j)}}{\partial y}) \\ &\quad -e^y_{(i)}(-h^y_{(j)}+y\frac{\partial h^x_{(j)}}{\partial x}-x\frac{\partial h^x_{(j)}}{\partial y})+h^y_{(i)}(-e^y_{(j)}+y\frac{\partial e^x_{(j)}}{\partial x}-x\frac{\partial e^x_{(j)}}{\partial y}) \\ &\quad -h^x_{(i)}(e^x_{(j)}+y\frac{\partial e^y_{(j)}}{\partial x}-x\frac{\partial e^y_{(j)}}{\partial y})\} \qquad (4.17)\end{aligned}$$

where

$$N_{(i)} = \left[\frac{1}{2}\int\int dxdy(\mathbf{e}^t_{(i)}\times\mathbf{h}^t_{(i)})\cdot\hat{z}\right]^{\frac{1}{2}} \qquad (4.18)$$

is the power in polarisation i ($N_{(j)}$ is defined similarly), superscript t indicates transverse field components, superscripts x and y indicate the x- and y-components of the vector field respectively and the fact that transverse fields may be chosen to be purely real has been used.

It is further shown that $\Gamma_{\uparrow\uparrow}$ and $\Gamma_{\rightarrow\rightarrow}$ are identically zero and that $\Gamma_{\uparrow\rightarrow} = -\Gamma_{\rightarrow\uparrow}$. Finally, γ is redefined as

$$\gamma = i\Gamma_{\uparrow\rightarrow}. \qquad (4.19)$$

The only restriction placed on the vector formulation is that the spin-rate be adiabatic so that restriction to the fundamental forward propagating modes is valid.

4.3.1 First Order Vector Corrections

The connection between the scalar and vector calculations carried out by Bassett may be elucidated by finding the first order vector corrections that must be applied to the scalar theory. Only $\Gamma_{\uparrow\rightarrow}$ need be considered.

The fundamental premise of the weak guidance approximation is that the vector modal fields may be expanded in terms of the profile height parameter

$$\Delta = \frac{n^2_{co}-n^2_{cl}}{2n^2_{co}}. \qquad (4.20)$$

A fibre is weakly guiding if $\Delta \ll 1$.

The expansions for the electric and magnetic vector modal fields have the form [20]

$$\begin{aligned}\mathbf{e} &= \mathbf{e}^{t;0}+\Delta^{\frac{1}{2}}e^{z;\frac{1}{2}}+\Delta\mathbf{e}^{t;1}+\Delta^{\frac{3}{2}}e^{z;\frac{3}{2}}\hat{\mathbf{z}}+\cdots \\ \mathbf{h} &= \mathbf{h}^{t;0}+\Delta^{\frac{1}{2}}h^{z;\frac{1}{2}}+\Delta\mathbf{h}^{t;1}+\Delta^{\frac{3}{2}}h^{z;\frac{3}{2}}\hat{\mathbf{z}}+\cdots\end{aligned}$$

where $\mathbf{e}$ and $\mathbf{h}$ are the exact vector modal fields, $\hat{\mathbf{z}}$ is a unit vector in the z-direction and the numerical superscripts separated from t or z by a semicolon are used to denote the order of the expansion.

Equation (4.17) does not contain any reference to the z-component of the fields so the expansions above may be reduced to the form

$$\mathbf{e} = \mathbf{e}^{t;0} + \Delta\mathbf{e}^{t;1} \tag{4.21}$$
$$\mathbf{h} = \mathbf{h}^{t;0} + \Delta\mathbf{h}^{t;1} \tag{4.22}$$

to first order in Δ. Writing these componentwise and using the arrow notation introduced above gives

$$e^x_\rightarrow = e^{x;0}_\rightarrow + \Delta e^{x;1}_\rightarrow \tag{4.23}$$
$$e^y_\rightarrow = \Delta e^{y;1}_\rightarrow \tag{4.24}$$
$$h^x_\rightarrow = \Delta h^{x;1}_\rightarrow \tag{4.25}$$
$$h^y_\rightarrow = h^{y;0}_\rightarrow + \Delta h^{y;1}_\rightarrow \tag{4.26}$$

for the $\rightarrow$- (x-) polarised mode and

$$e^x_\uparrow = \Delta e^{x;1}_\uparrow \tag{4.27}$$
$$e^y_\uparrow = e^{y;0}_\uparrow + \Delta e^{y;1}_\uparrow \tag{4.28}$$
$$h^x_\uparrow = h^{x;0}_\uparrow + \Delta h^{x;1}_\uparrow \tag{4.29}$$
$$h^y_\uparrow = \Delta h^{y;1}_\uparrow \tag{4.30}$$

for the $\uparrow$- (y-) polarised mode. The additional superscripts x and y are used to indicate the vector component of the appropriate polarisation mode.

Substitution of Equations (4.23) through (4.30) into the integrand in the numerator of Equation (4.17) gives (see appendix A for details)

$$\text{Integrand} = e^{x;0}_\rightarrow h^{x;0}_\uparrow - e^{y;0}_\uparrow h^{y;0}_\rightarrow + \Delta q(x,y) \tag{4.31}$$

where

$$\begin{aligned} q(x,y) = {} & e^{x;0}_\rightarrow h^{x;1}_\uparrow + e^{x;1}_\rightarrow h^{x;0}_\uparrow - e^{y;0}_\uparrow h^{x;1}_\rightarrow - e^{y;1}_\uparrow h^{y;0}_\rightarrow \\ & + e^{x;0}_\rightarrow \left(y\frac{\partial h^{y;1}_\uparrow}{\partial x} - x\frac{\partial h^{y;1}_\uparrow}{\partial y} \right) + h^{y;0}_\rightarrow \left(y\frac{\partial e^{x;1}_\uparrow}{\partial x} - x\frac{\partial e^{x;1}_\uparrow}{\partial y} \right) \\ & - e^{y;1}_\rightarrow \left(y\frac{\partial h^{x;0}_\uparrow}{\partial x} - x\frac{\partial h^{x;0}_\uparrow}{\partial y} \right) - h^{x;1}_\rightarrow \left(y\frac{\partial e^{y;0}_\uparrow}{\partial x} - x\frac{\partial e^{y;0}_\uparrow}{\partial y} \right) \end{aligned} \tag{4.32}$$

and terms of order Δ^2 have been dropped. From Maxwell's equations it follows that the sign of $e_{\rightarrow}^{x;0} h_{\uparrow}^{x;0}$ is opposite to the sign of $e_{\uparrow}^{y;0} h_{\rightarrow}^{y;0}$ and so the first two terms in equation (4.31) effectively add.

The above analysis shows that, to a good approximation, γ may be computed solely from the major field components in agreement with Bassett's scalar result.

4.4 Numerical Calculations

In this section a potential design for a circularly birefringent fibre is examined. A model of a circularly birefringent fibre is analysed in order to obtain estimates of the effect of parameter variations on the degree of circular birefringence. In addition, a double PANDA fibre is analysed and the degree of circular birefringence ascertained.

The γ parameter was calculated using Equation (4.17) with all integrations being carried out numerically in transform space. The mesh size used in all calculations was 100×100.

4.4.1 Model Fibre

The fibre described in Section 3.5.3 when spun should give rise to a useful level of circular birefringence, that is, the overlap integral of the x- and y-polarised fundamental modes will be significantly less than unity.

The permittivity tensor is described analytically by Equation (3.25) and the nonzero elements are reproduced here for convenience

$$\begin{aligned} \varepsilon_{11} &= n_{\mathrm{cl}} + \Delta Q(x,a) \\ \varepsilon_{22} &= n_{\mathrm{cl}} + \Delta Q(y,a) \\ \varepsilon_{33} &= n_{\mathrm{cl}} + \Delta Q(x,a) + \Delta Q(y,a) \end{aligned} \tag{4.33}$$

where

$$\begin{aligned} Q(x,a) &= \exp\left[-\left(\frac{r_x^+}{a}\right)^4\right] + \exp\left[-\left(\frac{r_x^-}{a}\right)^4\right], \\ Q(y,a) &= \exp\left[-\left(\frac{r_y^+}{a}\right)^4\right] + \exp\left[-\left(\frac{r_y^-}{a}\right)^4\right], \end{aligned}$$

$$\begin{aligned} r_x^{\pm} &= \left[(x \mp b)^2 + y^2\right]^{\frac{1}{2}}, \\ r_y^{\pm} &= \left[x^2 + (y \mp b)^2\right]^{\frac{1}{2}}, \end{aligned}$$

$a = 3.0\mu$m, $n_{cl} = 1.457$ with b and Δ variable. Calculations were carried out at a wavelength of 1.3µm.

The geometry of the cross-section of the fibre is shown in Figure 4.1. The shading is used to indicate the contours of the major component of the electric field in the respective polarisations. It should be noted that the x-polarised (y-polarised) mode is influenced by the 22 (11) component of the permittivity very slightly by cross-coupling through the minor field component.

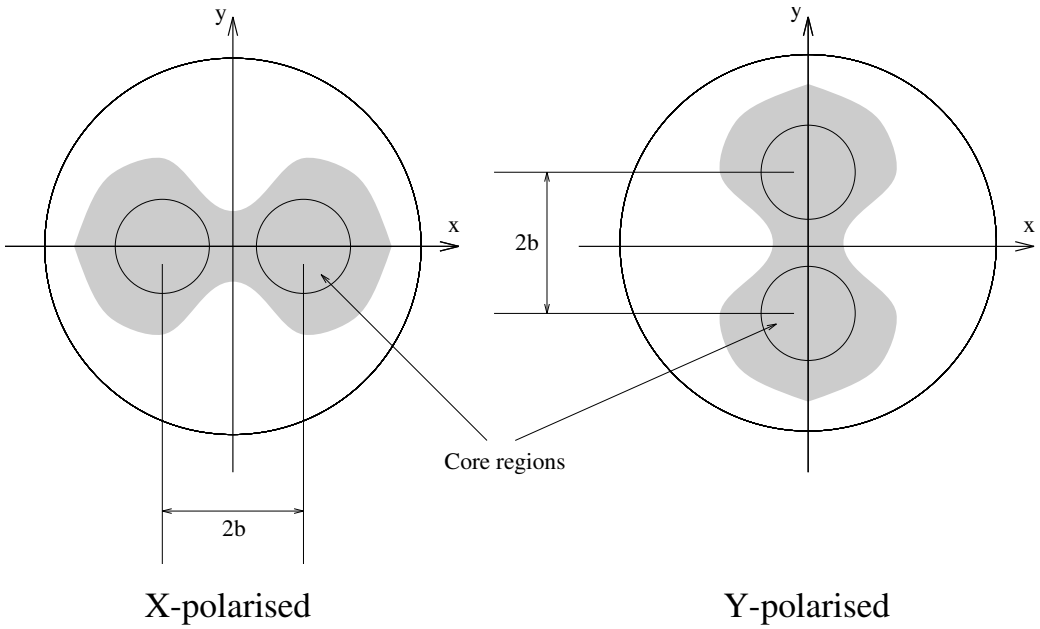

Figure 4.1: Geometrical layout of model fibre

'Core' separation was varied while holding the core-cladding index difference fixed at 0.002. The results are shown graphically in Figure 4.2. For core separations greater than 15µm the structure is 2-moded, an undesirable complication.

Physically, the graph may be explained as follows. When the cores are well separated the x- and y-polarised fundamental modes are most dissimilar so γ is relatively small. As the cores approach one another γ increases towards its ultimate value of unity that would be obtained when the guiding regions overlay one another, i.e. $b = 0$.

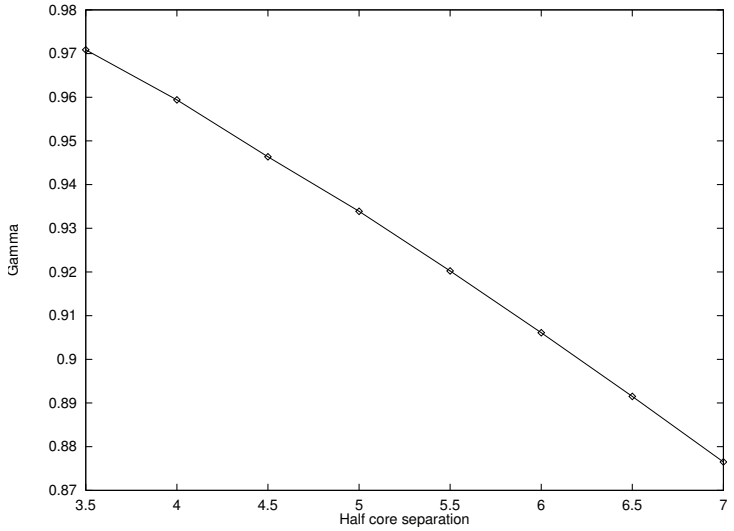

Figure 4.2: Plot of γ versus half-core separation with $\Delta n = 0.002$

The refractive index difference was also varied while holding the core separation fixed at 10μm. The results are shown graphically in Figure 4.3. As the refractive index difference is made smaller the fields spread more and so become more similar. Consequently γ increases. For larger index differences the fields are more confined to the cores and so γ is relatively small.

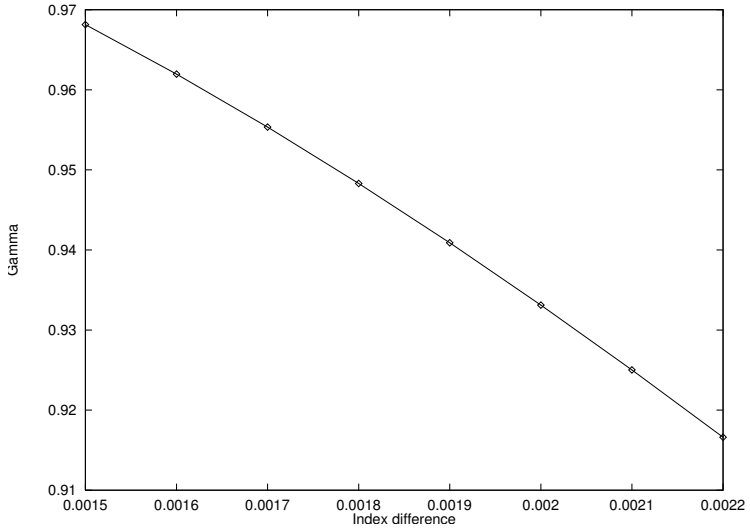

Figure 4.3: Plot of γ versus Δn for fixed core separation of 10μm

Contour plots of typical major fields of the x- and y-polarised modes are shown

in Figure 4.4. The 'hourglass' shape of the fields is clearly visible.

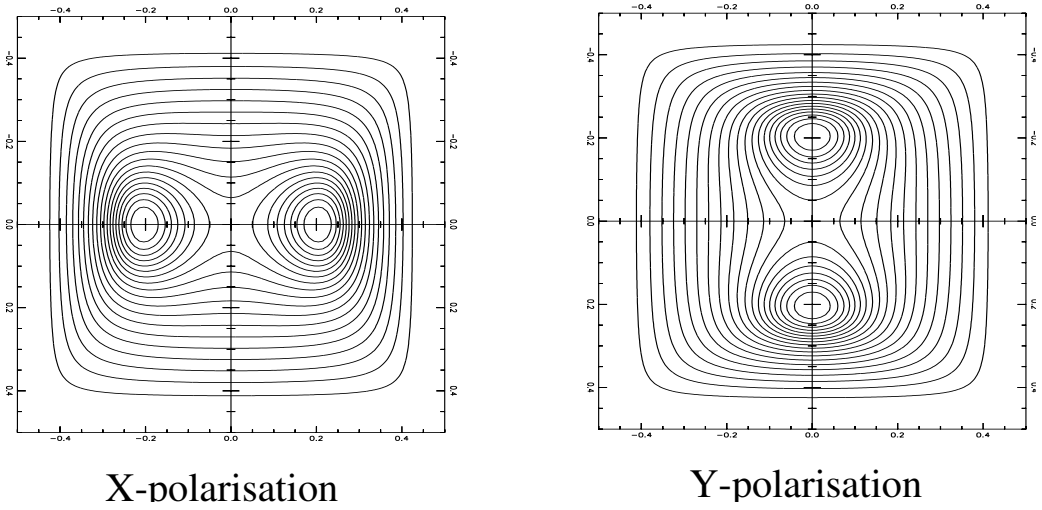

Figure 4.4: Contour plots of typical major fields of x- and y-polarised fundamental modes of biaxial fibre

4.4.2 Double PANDA fibre

One possible way of constructing a fibre with the required anisotropic permittivity distribution is to use stress producing elements. Anisotropy is produced in the permittivity tensor via the stress-optic effect [82]. The example presented is based on a double PANDA structure although a double bow-tie fibre could also be used.

A conventional PANDA fibre consists of a central guiding core region consisting of germanium doped silica and two symmetrically placed circular stress producing regions consisting of boron doped silica. The introduction of boron depresses the refractive index below that of the cladding whilst increasing the differential thermal expansion coefficient relative to that of silica. The overall result is that when the fibre is drawn there is a nett residual stress due to the differential expansion between the silica cladding, the germanium doped core, and the stress producing regions. This gives rise, via the stress-optic effect, to a permittivity tensor that is biaxial with the stress induced optical axes aligned along the x- and y-axes. It is the difference in stress induced permittivity components that give rise to the linear birefringence properties of PANDA fibres. The difference in refractive index seen by x- and y-polarised light can be as much as a few parts in 10^{-4} giving rise to a linear birefringence beatlength of about 1mm at typical operating wavelengths.

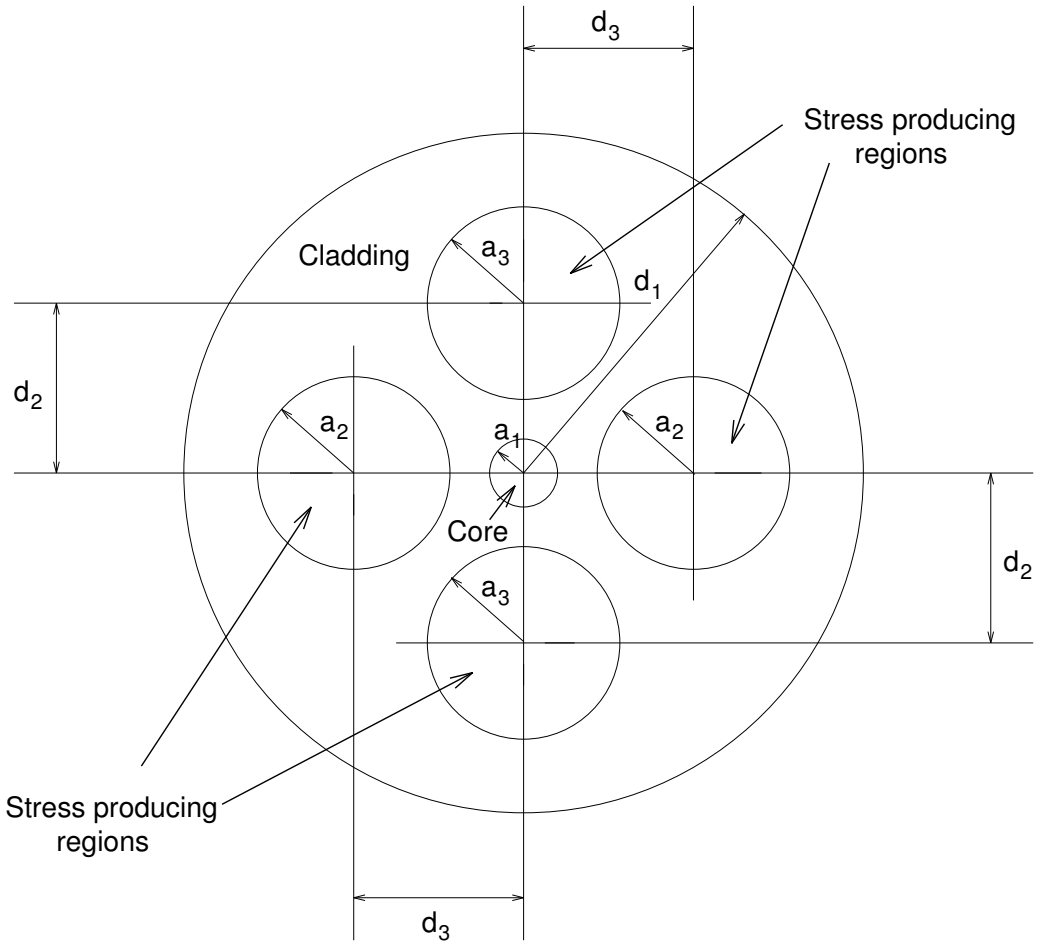

Figure 4.5: Detailed geometry of cross-section through a double PANDA fibre

The single PANDA fibre does not possess the symmetry required for circular birefringence as may be deduced from its linear birefringence properties. However, by introducing a second pair of stress producing regions identical to the first with their centres placed on the axis orthogonal to the first pair a structure which may be referred to as a double PANDA results. The cross section through a double PANDA fibre is shown in Figure 4.5.

In order to proceed with the electromagnetic field analysis of the double PANDA fibre it is first necessary to compute the permittivity distribution taking into account the stress distribution due to the different thermal expansions of all the regions. The approach taken is based on the plane strain analysis of Chu and Sammut [69] with the conversion from stress tensor components to permittivity tensor components following the treatment of Okamoto, *et. al.* [83]. Under

the plane strain approximation the stress tensor, and hence the permittivity tensor, have the form given in Section 3.2. A program for carrying out these computations was provided by Dr D. Wong of the Optical Fibre Technology Centre, University of Sydney. The required inputs are the fibre dimensions as shown in Figure 4.5, the germanium and boron dopant concentrations, and the operating temperature of the fibre.

The permittivity tensor components as produced by Wong's program must be smoothed before being used as inputs to the vector wave equation solver. The smoothing was performed using two-dimensional Gaussian filtering in the frequency domain with $\sigma_x = \sigma_y = 0.1$—the direct generalization of the method described in Section 3.5.1. Such smoothing is valid because the permittivity distributions in a fibre manufactured by the MCVD process will have no sharp edges.

Usable levels of circular birefringence can only be produced if the x- and y-polarised major field components are significantly distorted from the nominally round fields found in ordinary fibres. Such distortion is seen if the core index elevation is about the same as the stress induced index elevation. The off diagonal elements of the permittivity tensor are not small in relation to the diagonal elements and so cannot be neglected. (Indeed, when working in Cartesian coordinates the permittivity tensor of a standard circularly symmetric fibre including stress, necessarily possess non-zero 12 (and 21) components in its permittivity tensor.)

In order to maximize the stress induced refractive index the core region was doped with boron. The germanium is introduced as an additional dopant to slightly raise the core index above the cladding level. Boron doped regions are inherently more absorbing than either pure silica or germanium-doped silica at 1.3μm, however, at 633nm boron doping introduces no additional loss [84]. By varying the boron and germanium concentrations it is possible to set the core index to essentially any useful value whilst retaining the highest possible stress values and it is tempting to remove the core altogether leaving a fibre in which guidance is achieved purely through the stress-optic induced index elevations. Numerical design studies show, however, that such structures do not provide sufficient guidance.

The number of parameters required to fully define a double PANDA fibre is large and full optimization is difficult. In order for the x- and y-polarisation modes to have the same propagation constant it is mandatory to set $a_2 = a_3$ and $d_2 = d_3$. The fibre radius d_1 was fixed at 62.5μm the same as for standard communications fibre. The other geometrical parameters were also held constant: the core radius, $a_1 = 5$μm, the stress region radii, $a_2 = a_3 = 12$μm and the offset of the centre of the stress regions, $d_2 = d_3 = 26$μm. These values are typical for standard PANDA fibres. The boron dopant concentration in the stress inducing regions was fixed at 20mol% well below the value of 25mol% at which the preform is likely to shatter.

The boron concentration in the core region was also fixed at 20mol% in order to produce maximum stress. The addition of germanium to the core does not change the stress behaviour significantly.

Two fibres are examined. **Fibre 1** has a core germanium concentration of 4.9mol% giving a peak core refractive index of 1.45907 somewhat below the peak stress induced refractive index and **fibre 2** has a core germanium concentration of 5.3mol% giving a peak core refractive index of 1.45927 somewhat above the peak stress induced refractive index. Both peak index values were computed at 0°C. Contour plots of the smoothed permittivity tensor components are shown in Figures 4.6 and 4.7 for fibre 1. The plots show

$$\Delta\varepsilon_{ii} = \varepsilon_{ii} - \varepsilon_{ii}^{\inf}$$

where $\varepsilon_{ii}^{\inf}$ is the unstressed value of the permittivity of pure silica at the operating wavelength of 0.6328μm and temperature of 0°C, in transformed coordinates. The off-diagonal element, ε_{12} takes the value zero in unstressed silica. The plots clearly show the distortion introduced by the nonlinear scaling transformation—

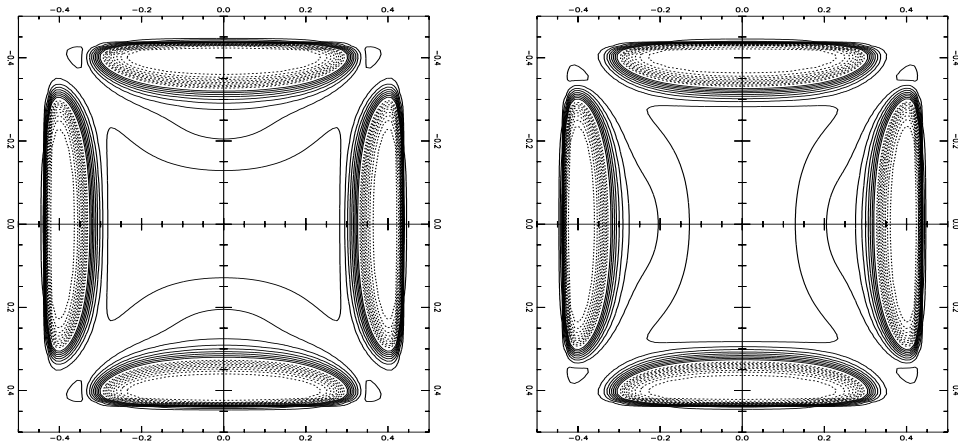

Figure 4.6: Contour plots of ε_{11} and ε_{22}

the elongated elliptical contours near the edges of the plots correspond to the stress inducing regions which are round in real

space. The biaxial nature of the permittivity tensor is clearly evident from these figures.

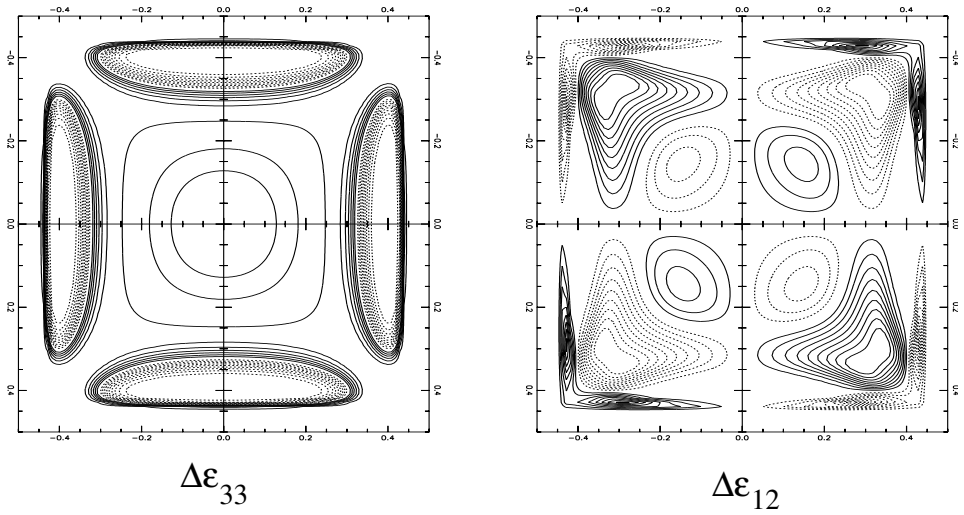

Figure 4.7: Contour plots of ε_{33} and ε_{12}

Results

Plots of the x-polarised electric field components for fibre 1 at 0°C are shown in Figures 4.8 and 4.9. The elongation of E_x along the x-axis is clearly visible and the intricate structure of E_y is also of interest. It should be noted the peak magnitude

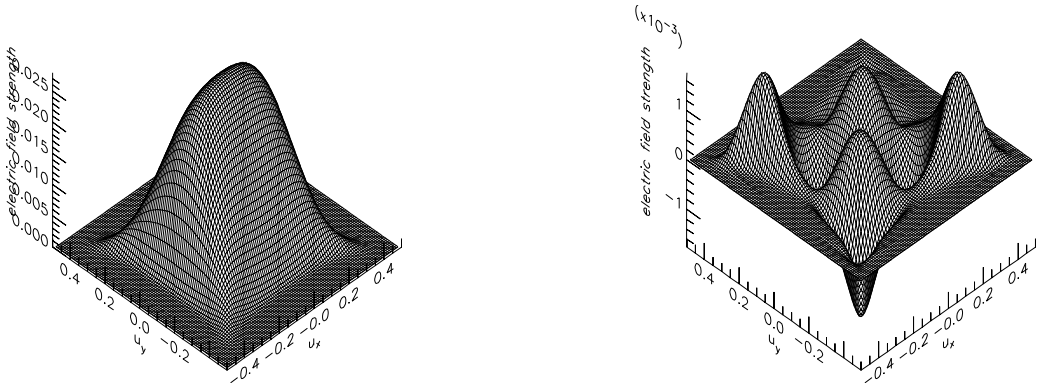

Figure 4.8: x- and y-components of x-polarised electric field

of E_y (the nominal 'minor' field) is greater than the peak magnitude of E_z. This

last result is not too surprising given the experimental observations of the minor field of a bow-tie fibre by Varnham, *et. al.* [85].

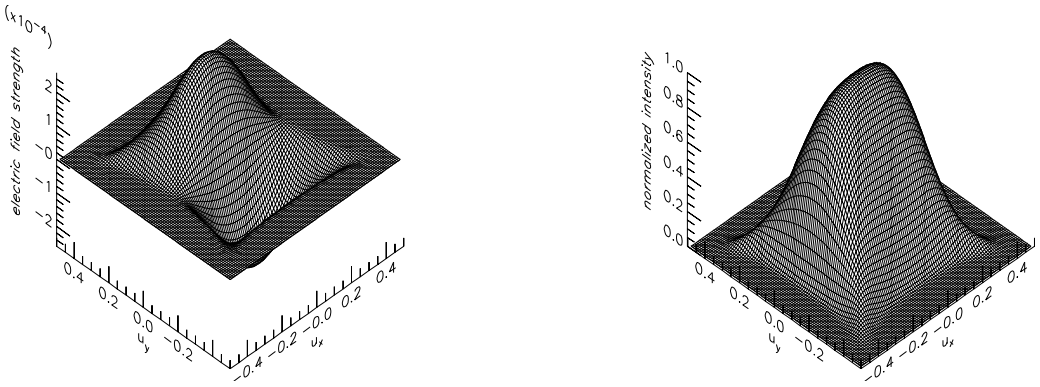

Figure 4.9: z-component and intensity of x-polarised electric field

The results of the numerical computations are displayed in Table 4.1. The beat length was calculated using an assumed spin-pitch $p = 1$mm. It is to be observed that γ increases when the refractive index difference between core and cladding

	fibre 1 @ 0°C	fibre 1 @ 20°C	fibre 2 @ 0°C	fibre 2 @ 20°C
n_{eff}	1.458860	1.458868	1.458969	1.458987
γ	0.901	0.913	0.953	0.959
$z_b(\text{mm})$	5.05	5.75	10.64	12.20

Table 4.1: Results of numerical computations for double PANDA fibres

is increased and when the temperature is increased. The reasons are as follows: when the core-cladding index difference is increased by adding additional germanium dopant to the core there is only a minimal increase in the stress induced refractive index and so the modal fields are more tightly bound to the core hence the two polarisation modes are more similar and γ increases. Similarly, when the temperature is increased the stress induced index falls whilst the core index remains essentially constant hence the influence of the stress induced index decreases and so γ increases.

Calculation at two different temperatures enables an estimate of the thermal stability of the circular birefringence to be made. For fibre 1 a simple calculation gives an increase in beat length of 0.69%/°C and for fibre 2 an increase in beat length of 0.73%/°C.

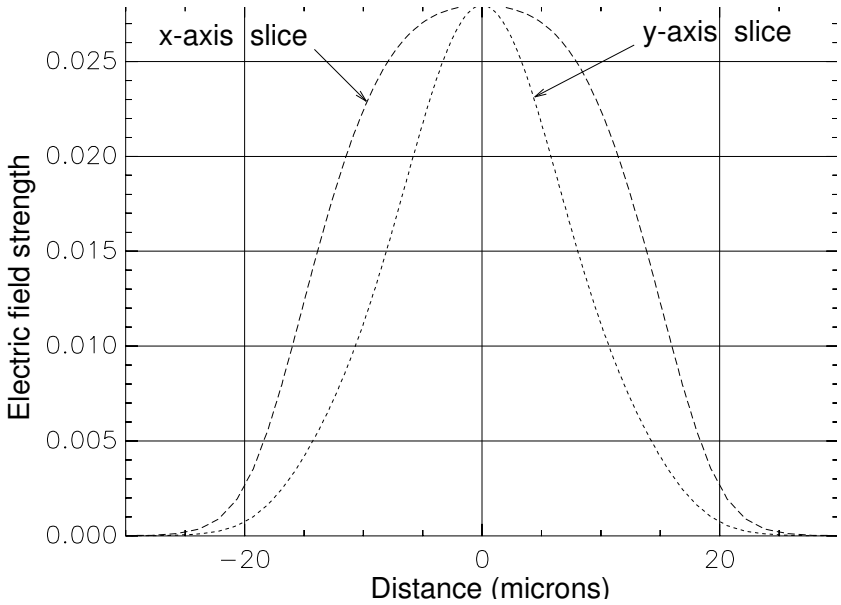

Figure 4.10: Sections through the major electric field component along the x- and y-axes for fibre 1 @ 0°C

It is also important to have some idea of the mode field diameter within the fibre in order to estimate both loss due to absorption in the boron stress regions and the ease of coupling to standard fibres. Figure 4.10 shows cross-sections through the major field components along the x- and y-axes for the nominal worst case of fibre 1 at 0°C. The $1/e$ mode field diameters are 34µm and 20µm respectively and should be compared with the usual 8 to 10µm mode field diameter of a standard fibre.

4.5 Conclusion and Discussion

In this chapter some practical designs for a circularly birefringent fibre have been presented. The fibres do not satisfy the usual 'weak guidance' condition (because the minor field is large). The full vector theory is required in order to make useful predictions. The designs presented need some tuning particularly to reduce the mode field diameter. Such tuning may be difficult within the current design framework given that the modal fields must be strongly influenced by the stress induced refractive index which is necessarily small thus requiring that the relative core index elevation be low and hence allowing the modal fields to spread significantly into the cladding. The bending loss must also be calculated because this will dictate the physical arrangement of such fibres and hence strongly influence

their application to various types of sensing and communication systems.

Laboratory demonstration of the viability of the design is, of course, necessary. Fabrication should not be much more difficult than a standard PANDA fibre. It is hoped that a sample of fibre will be available in the near future.

Chapter 5

Twin-core Wavelength Demultiplexer

5.1 Introduction

The twin-core fibre is the simplest of multiple core fibre structures yet it exhibits a range of theoretically interesting and practically useful properties. In particular if the two cores are sufficiently similar and relatively close together, coupling will occur between modes of equal (or nearly equal) propagation constants in each core. This modal coupling is analogous to the behaviour of coupled pendula.

An analytic solution of optical coupling in multi-core fibres was first presented by Jones in 1965 [86] who arrived at a pair of coupled differential equations via an integral equation approach to the problem. General coupled-mode theory for an essentially arbitrary number of coupled cores was described by Snyder [87] and forms the basis of the formal electromagnetic approach to the problem. Unfortunately, the coupled-mode equations are normally insoluble analytically so it is necessary to either solve them numerically or by various approximation techniques.

An alternative and much more intuitive approach is afforded by regarding the modes of the coupled twin-core structure as superpositions of the modes of the uncoupled fibres [88]. Such superposed modes are known as 'supermodes'. Supermodes are the exact modes of the twin-core structure. However, if the constituent single core fibres are single-moded and polarisation is neglected then the supermodes are given approximately as the even and odd superposition of the single bound mode. The two superpositions are usually referred to as the even and odd supermode because of their symmetry with respect to the fibre axis as shown in Figure 5.1.

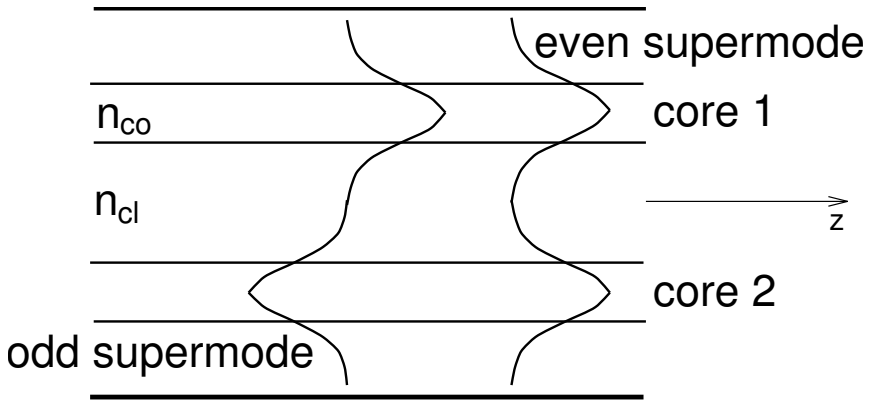

Figure 5.1: Even and odd supermodes in a twin-core fibre

Analysis of twin-core structures using supermodes proceeds by finding the modes of the individual fibres in isolation and using perturbation theory to compute the propagation constants of the even and odd supermodes [20]. Such an approach is strictly valid when the coupling is weak (i.e., the cores are well separated) but in practice good results are obtained down to the point when the cores virtually touch [89].

A third approach is to solve the wave equation (essentially exactly) numerically in the twin-core fibre and this is the method used here. No limitation is placed on the strength of the coupling and as perturbation methods are not used the results obtained are as accurate as the solutions of the wave equation.

5.1.1 Wavelength Demultiplexing

The ever increasing demand on communication systems is to carry more information over pre-existing channels. Today, most high data rate communication systems use some form of wavelength-division or time-division multiplexing. In the former, signals with different information content are sent at different wavelengths over the same communication channel and in the latter (digital) signals with different information content are allocated a portion of time over which they are transmitted. Both methods achieve the same end—more than one information bearing signal is available at the receiver. (Wavelength-division multiplexing is not restricted to digital signals, however, time-division multiplexing of a group of analogue signals would be extremely difficult to realise in practice.)

At the receiver the inverse operation has to be performed that is, the incoming multiplexed signal has to be demultiplexed to yield its constituent information containing components. In this chapter a novel design for an all-fibre optical wavelength demultiplexer is examined. The work is a large collaboration between

workers at the University of Sydney (Dr S. B. Poole, Dr G. A. Atkins, Mr P. Coghill, Mr D. Thorncraft, Mr J. Shun and the author), the University of New South Wales (Prof. P. L. Chu and Dr P. Allen), the Australian National University (Dr J. D. Love and Dr S. J. Hewlett) and Siemens Ltd. (Mr B. Gillhoff and Mr J. Arkwright) with the ultimate aim of producing a commercially viable twin-core wavelength demultiplexer.

The essential requirements are to split a 1.55μm digital (telephone) signal from a 1.3μm analogue (cable television) signal with better than 40dB extinction ratio. Such a high extinction ratio is required to ensure purity of the analogue signal. If both signals were digital a more modest 20dB extinction ratio would suffice.

5.2 Twin-core Wavelength Demultiplexer Design

5.2.1 Twin-core Fibre Coupling Properties

It is customary to describe the coupling between modes of a twin-core optical fibre in terms of a coupling coefficient, C, defined by

$$C = \frac{1}{2}|\beta_1 - \beta_2| \tag{5.1}$$

where β_1 and β_2 are the propagation constants of the even and odd supermodes respectively.

If the cores are identical then the power transfer from core 1 to core 2 (refer to Figure 5.1) and vice versa is a function of distance along the fibre [20] with a particularly simple form,

$$P_1(z) = \cos^2(Cz) \tag{5.2}$$
$$P_2(z) = \sin^2(Cz), \tag{5.3}$$

where it has been assumed that $P_1(0) = 1$ and $P_2(0) = 0$. Hence all the power in core 1 is transferred to core 2 and back to core 1 again in a distance of

$$z_b = \frac{\pi}{C} \tag{5.4}$$

referred to as the beat length.

5.2.2 Principle of Operation

The coupling coefficient clearly depends on the wavelength of operation, core radius, core separation and refractive index profile of the constitutive cores. If these

parameters are chosen appropriately it is possible for the beat length at 1.3μm to be twice that at 1.55μm allowing the two wavelengths to be conveniently accessible at the output ports of the device. A schematic representation of such a device is shown in Figure 5.2. With three free parameters to choose the design problem is difficult. However, the core radius and profile can be fixed (essentially) *á priori* during preform manufacture provided the final fibre diameter is specified. Then, the problem is reduced to finding the centre-to-centre core separation, d, at which

$$z_b(1.3) = 2z_b(1.55). \tag{5.5}$$

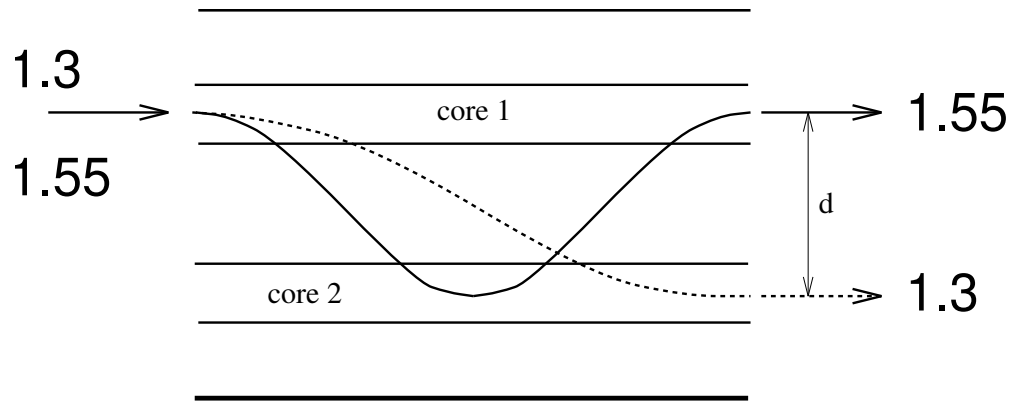

Figure 5.2: Schematic of twin-core wavelength demultiplexer

Optical wavelength demultiplexers relying on this principle of operation have been fabricated recently using planar waveguide technology [90]. Such devices are also of interest as multiplexers in order to combine pump and signal beams in optical amplifiers [91]. An all fibre twin-core wavelength demultiplexer relying on bending the fibre in the plane of the cores has also been recently reported [92].

5.3 Device Specification and Tolerance

In order for such a demultiplexer to be practically usable in a consumer device it is necessary that device length be not longer than about 10mm, i.e. $z_b(1.55) \lesssim 10$mm. The fibre to which the demultiplexer will be attached is a standard single mode communication fibre with a nominal refractive index difference of 0.005 and a nominal core radius of 4μm. For reasons of field matching it is convenient to construct the multiplexer from an equivalent fibre.

5.3.1 Analytic Approximation

An approximation of the core spacing and device length can be calculated using standard results for two parallel step-profile circular cores. The coupling coefficient is given by [20]

$$C \approx \left(\frac{\pi\Delta}{Wd\rho}\right)^{\frac{1}{2}} \frac{U^2}{V^3} \frac{\exp(-Wd/\rho)}{K_1^2(W)} \tag{5.6}$$

where Δ is the normalized profile height, ρ is the core radius, d is the centre-to-centre core spacing, $W = \rho(\beta^2 - k^2 n_{cl}^2)^{\frac{1}{2}}$ is the (bound mode) cladding parameter, $U = \rho(k^2 n_{co}^2 - \beta^2)^{\frac{1}{2}}$ is the core parameter and $V = k\rho(n_{co}^2 - n_{cl}^2)^{\frac{1}{2}}$ is the normalized frequency and $K_1()$ is the modified Bessel function of the first kind and order 1.

For purposes of approximation assume that $V \approx 2.2$ whence $U \approx W \approx V/\sqrt{2}$ (see table 14-4 in [20]) in which case Equation (5.6) becomes

$$C = \left(\frac{\sqrt{2}\pi\Delta}{Vd\rho}\right)^{\frac{1}{2}} \frac{1}{2V} \frac{\exp\left(-Vd/\sqrt{2}\rho\right)}{K_1^2(V/\sqrt{2})}. \tag{5.7}$$

Equation (5.7) can be used to determine the coupling coefficients as a function of core separation at wavelengths of 1.3μm and 1.55μm. By setting $\rho = 4\mu$m and $\Delta = 0.005$ the ratio, $R(d)$, is given by

$$R(d) = \frac{k_2^{\frac{3}{2}}}{k_1^{\frac{3}{2}}} \frac{K_1^2(V_2/\sqrt{2})}{K_1^2(V_1/\sqrt{2})} \exp\left(-(V_1+V_2)d/4\sqrt{2}\right) \tag{5.8}$$

where $k_1 = 2\pi/(1.3 \times 10^{-6})\text{m}^{-1} = 4.833 \times 10^6\text{m}^{-1}$, $k_2 = 2\pi/(1.55 \times 10^{-6})\text{m}^{-1} = 4.054 \times 10^6\text{m}^{-1}$; and $V_1 = 1.93$ and $V_2 = 1.62$ calculated using the definition for V above.

A plot of $R(d)$ versus d is shown in Figure 5.3 clearly indicating that a beat length ratio of $2:1$ occurs at around $d = 20.1\mu$m. The device length is approximately 5.5mm. It must be noted that the approximation used is fairly rough but it does show the feasibility of an all fibre wavelength demultiplexer meeting the design goals.

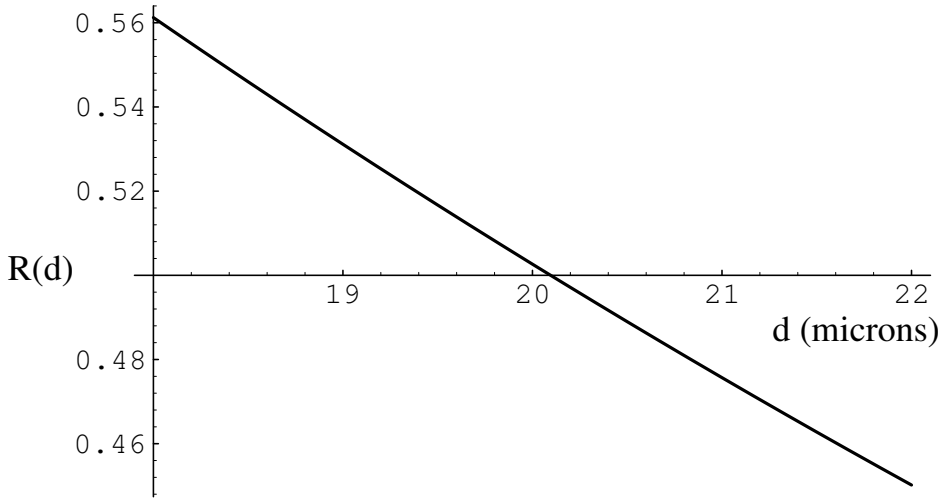

Figure 5.3: Approximate analytic determination of core separation

5.3.2 Calculations Using Preform Data

A preform—designation AD227—with $\Delta n \approx 0.005$ and core radius 0.4mm was fabricated at the Optical Fibre Technology Centre (University of Sydney) using the modified chemical vapour deposition process [93]. The refractive index profile is shown in Figure 5.4. It must be pointed out that Figure 5.4 shows a single core which is used to form the twin-core fibre using the technique outlined in section 5.4.1 below. The inhomogeneity over the core region is clearly visible making an analytic calculation all but impossible.

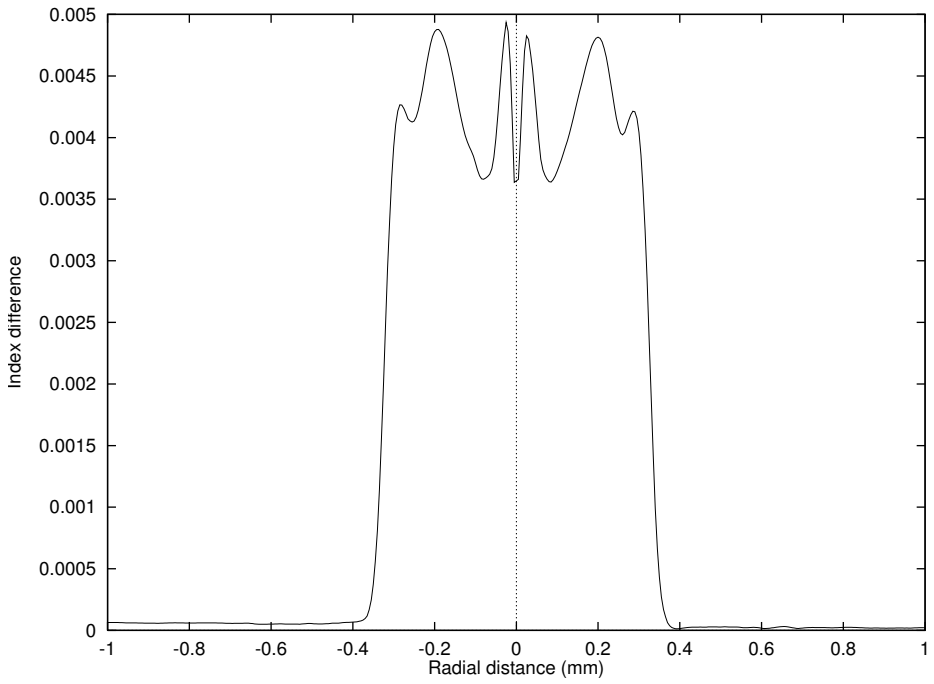

Figure 5.4: Preform profile of AD227

In order to compute the core separation required to produce a beat length ratio of $2:1$ it was assumed that both cores were identical. Calculations were carried out using the scalar solver described in Chapter 2 on a 200×200 grid providing 7 significant figures in the propagation constant and hence about 0.1% accuracy in the beat length. The cores were scaled down to 4μm radius for calculation purposes.

A plot of beat length versus core separation is shown in Figure 5.5. From the graph, the core separation required for demultiplexing 1.3μm radiation from 1.55μm radiation is 13.93μm and the device length is 8.28mm.

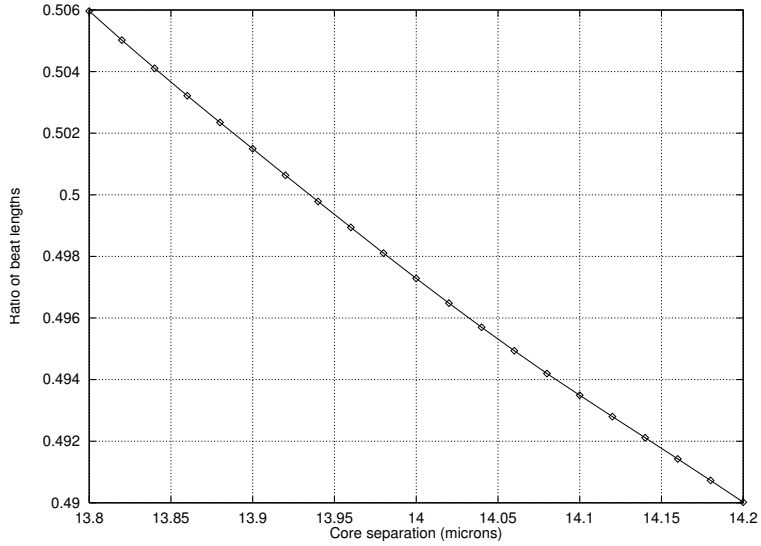

Figure 5.5: Beat length ratio for twin-core fibre composed of preform AD227

Independent calculation of the required centre-to-centre core separation by Hewlett and Love [94] gave a value of 14.03μm. The computed device length was 7.92mm. The slight discrepancy is most likely due to the different way the experimental data is fitted to the assumed uniform cladding in the two different numerical methods. However, it must be noted that the core separation value lies within the tolerance computed below.

5.3.3 Tolerances

Ideally the product of the coupling constant at 1.55μm and the device length must satisfy

$$C(1.55)z_b(1.55) = 2\pi \tag{5.9}$$

for 100% power transfer from core 1 to core 2 and back again. However, due to tolerance in the manufacturing process it is unlikely that such exact behaviour will occur in practice. The -40dB crosstalk criterion can be used to place tolerances on the design parameters. The simplest way of setting the tolerance level is to view any shift from the ideal as a small error, δ, in Equation (5.9) which then becomes

$$C(1.55)z_b(1.55) = 2\pi + \delta. \tag{5.10}$$

Substituting into Equations (5.2) and (5.3) and noting that $\cos^2(2\pi+\delta) \approx 1$ and $\sin^2(2\pi+\delta) \approx \delta^2$ for small δ, the crosstalk criterion becomes

$$\delta \leq \frac{1}{100}. \tag{5.11}$$

That is the beat length and hence the beat length ratio must be within 1% of the nominal value of 0.5—$0.495 \leq R(d) \leq 0.505$—in order for correct demultiplexing action.

The effect of variation in design parameters was quantified by perturbing one parameter from its nominal design value (whilst holding all other parameters constant) and monitoring the beat length ratio. It is implicitly assumed that the parameters of each core will change in the same manner over the device length because the entire demultiplexer will be formed from a very short piece of the preform.

The peak refractive index difference was varied from 0.004 to 0.006 and the beat length ratio computed. A plot of the variation is shown in Figure 5.6. The monotonically decreasing behaviour of the Δn versus R plot can be analytically verified from Equation (5.8) where the Δn variation comes in through the V value. At the design value of Δn the beat length ratio is 0.5.

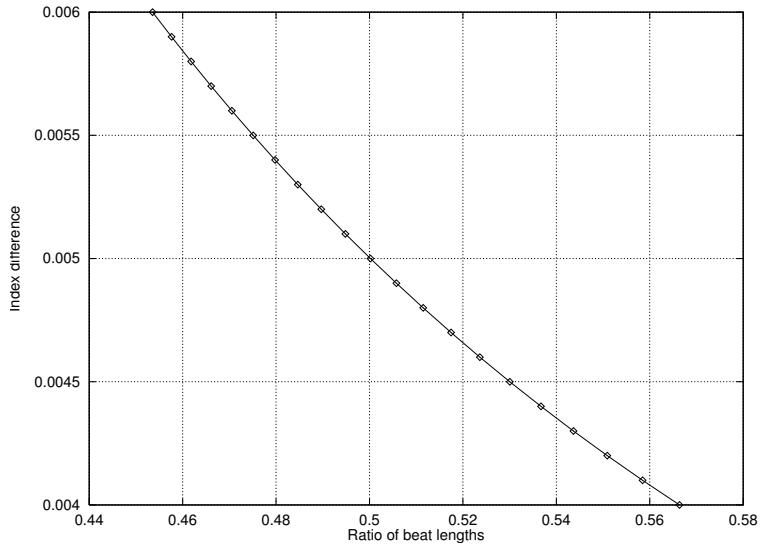

Figure 5.6: Effect of core Δn variation on beat length ratio for twin-core fibre composed of preform AD227

The required design tolerance on Δn is $0.00494 \leq \Delta n \leq 0.0055$ thus the value of Δn must lie within -1.2% and +1.0% of the specified value.

Variation in core radius also has an effect on the beat length ratio. Calculations were carried out in the same manner as for the Δn variation and results are shown in Figure 5.7. Second order effects are now evident as the plot is no longer monotonic. The beat length ratio is relatively insensitive to radius variation and the core radius can lie between 3.38μm and 4.09μm whilst still satisfying the beat length criterion to within the 1% level. The tolerance specification is therefore

rather wide—the core radius must be within -15.5% and +2.25% of the nominal design value of 4µm. The wide tolerance is to be expected due to the second order influence of the core radius on beat length ratio. The effect cannot be predicted analytically using the simple approximation presented above.

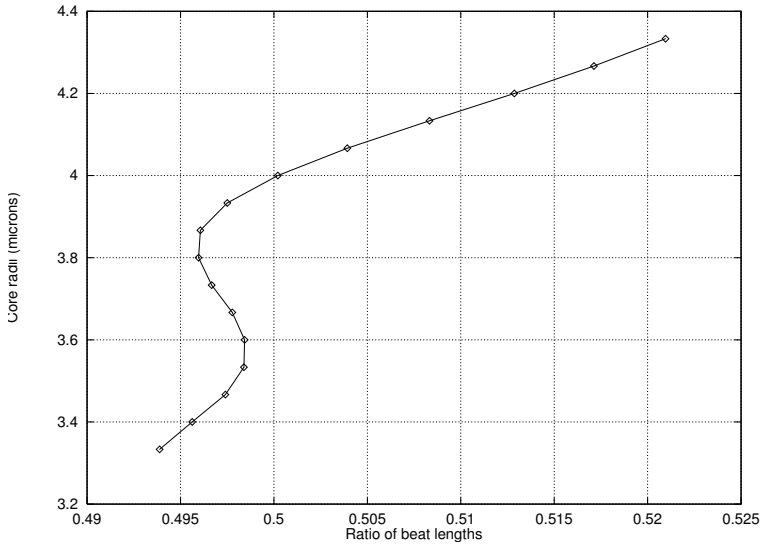

Figure 5.7: Effect of core radius variation on beat length ratio for twin-core fibre composed of preform AD227

Referring to Figure 5.5 it is apparent that in order for the beat length ratio to lie within $\pm 1\%$ of the design value the core separation must fall within the range $13.82\mu m \leq d \leq 14.052\mu m$, placing fabrication tolerances of -0.79% and +1.1% on the core separation.

It is evident that accuracy in setting the core separation is most critical in obtaining a working device. This can be further quantified by using the sensitivity parameter. This parameter is commonly used in electronic filter design [95] to compute the effect of changing circuit component values on the frequency response of the filter.

The sensitivity, S_p^v, of an output v dependent on a parameter p is defined by

$$S_p^v = \frac{p}{v}\frac{\partial v}{\partial p}. \tag{5.12}$$

If $S_p^v << 1$ then the output is insensitive to changes in the parameter v. Conversely, if $S_p^v \approx 1$ or greater then the output is extremely sensitive to changes in the parameter p.

In this case the beat length ratio, R, is viewed as the output and is dependent on the core separation, d. Then, S_d^R is given by

$$S_d^R = \frac{d}{R}\frac{\partial R}{\partial d}. \tag{5.13}$$

The sensitivity of beat length ratio as the core separation changes is shown in Figure 5.8. The fact that the sensitivity is negative reflects the fact that as the core separation increases the beat length ratio decreases.

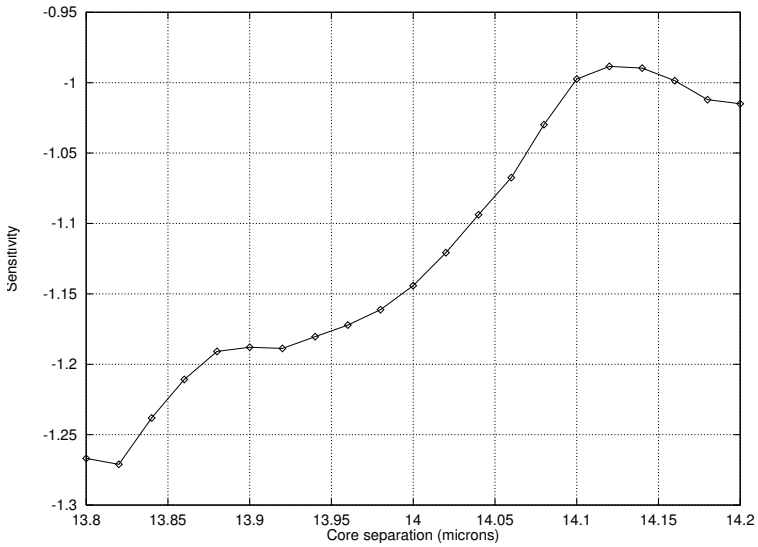

Figure 5.8: Sensitivity of beat length ratio to core separation for twin-core fibre composed of preform AD227

The sensitivity does not fall much below unity across the entire scanned range of core separation indicating the extreme dependence of beat length ratio on core separation.

Independent calculations by Hewlett and Love [96] using a different preform profile and different numerical wave equation solver have yielded similar tolerances in the design parameters of a twin-core fibre demultiplexer.

5.4 Twin-Core Fibre—Fabrication, Simulation and Performance

5.4.1 Fabrication

The preform AD227 was used to fabricate the twin-core demultiplexer to the given design. The fabrication process [93] involved cutting the preform in half to yield two single core preforms. These preforms were then cut longitudinally and polished down so that when rejoined and drawn the core separation met the previously specified core-to-core separation. The twin-core preform was designated AD237.

The overall twin-core preform fabrication process is shown schematically in Figure 5.9.

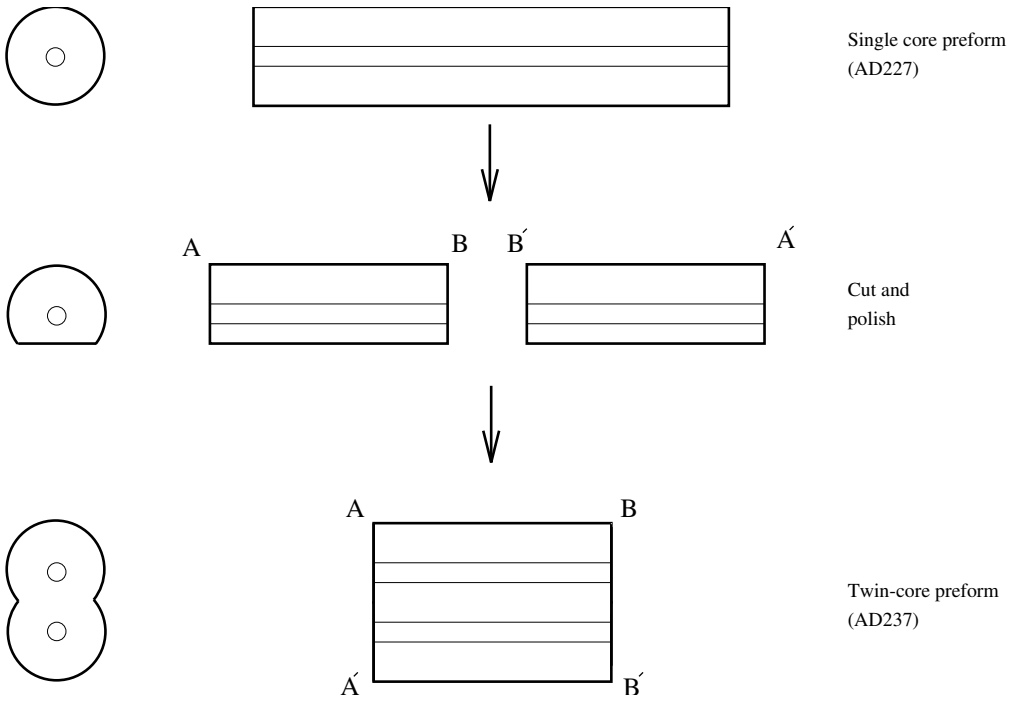

Figure 5.9: Steps in fabricating twin-core preform AD237

The twin-core preform was drawn down to form a 130µm diameter fibre giving a measured centre-to-centre core separation of 14.03 ± 0.05µm. Both cores had a measured radius of 8.3 ± 0.05µm. A fibre refractive index profile could not be obtained due to the diameter of the fibre being too large for the fibre refractive index profiler.

5.4.2 Simulation

Figure 5.10 shows a surface plot of the refractive index profile of preform AD237 as measured on a York Technologies P102 preform profiler. Due to the unavailability of a fibre profile the preform profile was scaled down using the experimentally measured fibre core-to-core separation value.

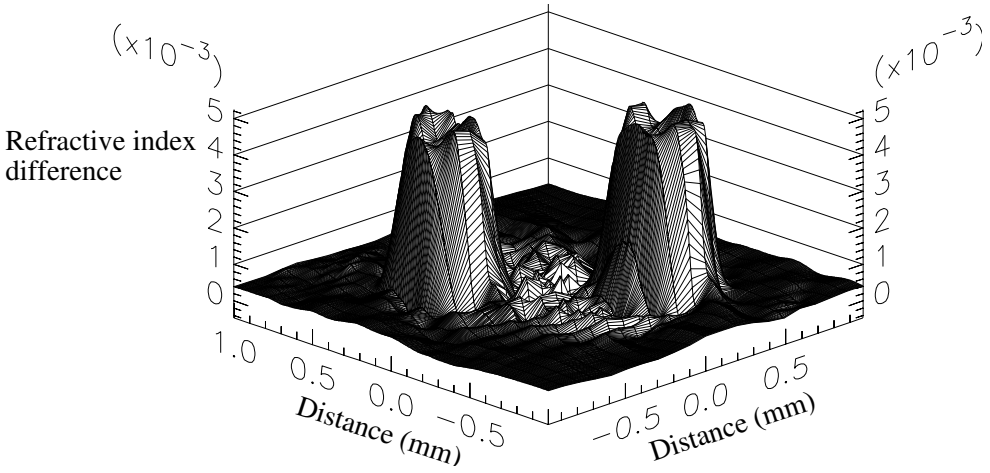

Figure 5.10: Two-dimensional refractive index profile of preform AD237

Computation of the effective indices of the even and odd supermodes, modal fields and beat lengths at 1.3µm and 1.55µm were carried out using the scalar wave equation solver on a 100×100 finite difference grid. Results are shown below in Table 5.1. The refractive index values were fitted to the grid using 2-dimensional cubic spline functions [63]. No smoothing of the data was performed.

Parameter	1.3µm	1.55µm
n_e (even)	1.448111	1.444825
n_e (odd)	1.447814	1.444421
beat length (mm)	4.38	3.84

Table 5.1: Computed parameters based on preform AD237

The cutoff wavelengths for the first six modes were also computed and are shown in Table 5.2. The computed cutoff wavelength for the second mode of a single core fibre based on preform AD227 is 1.138µm. The fact that the second and

third mode cutoffs of the twin-core fibre are below the single core second mode cutoff value while the fourth and fifth mode cutoffs are above is consistent with analytic results for coupled step core profiles due to Love and Ankiewicz [97].

Mode cutoff	Wavelength (μm)
second	2.407
third	1.208
fourth	1.179
fifth	1.118
sixth	1.082

Table 5.2: Cutoff of the lowest six modes based on preform AD237

Using the values for the beat length shown above the beat length ratio was found to be 0.89—very different from the design goal of 0.5.

The modal fields of the even and odd supermodes at 1.55μm are shown in Figure 5.11. The smoothness of the field plots again attests to the robustness of the scalar solver even in the presence of extremely noisy data.

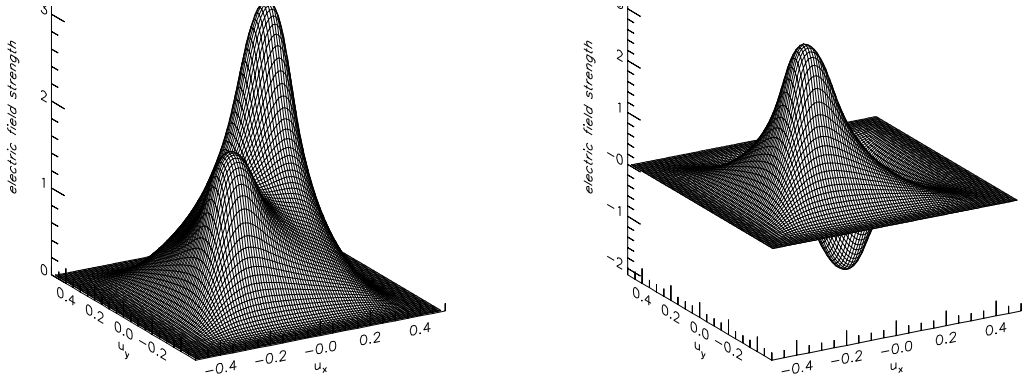

Figure 5.11: Nominally even and odd supermodes computed from preform AD237

It is evident from the modal field plots that a twin-core fibre formed from preform AD237 will perform extremely poorly as a coupler at 1.55μm because of the disparity in field amplitudes in the two cores. The coupling strength was estimated to be 35% from the calculated modal fields. The poor coupling is due to the lack of similarity in the refractive index profiles of the individual cores because of the lack of fine control in the MCVD process. It is well known [88] that the cores of a twin-core fibre must be nearly identical for significant power

transfer from one core to the other. Hence the device will perform poorly at all wavelengths.

5.4.3 Performance

Three lengths of fibre were drawn from preform AD237 and each was characterised for cutoff [93], coupling and demultiplexing [98].

The measured cutoff value for a length of single core fibre drawn form AD227 was 1.050μm which is not inconsistent with the computed value above. However, the cutoff value for the twin-core fibre was measured as 950nm far lower than any of the computed modal cutoffs for the twin-core. This result is not understood at present and work is ongoing.

Two of the fibres performed poorly. The first fibre showing 25% coupling which is in agreement with the simulations carried out in Section 5.4.2 above. The second length of fibre showed no coupling behaviour at all. The third showed a coupling strength of around 95% more than likely due to the fibre being drawn nearer to the end marked BB' in Figure 5.9. Demultiplexing action of all three fibre lengths was not evident.

5.5 Conclusions and Discussion

The possibility of constructing an all fibre optical wavelength demultiplexer has been theoretically demonstrated and fabrication tolerances computed. The required tolerances are quite high and may be beyond the capability of current modified chemical vapour deposition processing which, being a gas-flow deposition system, is likely to be accurate only to the few percent level, and hence more than likely outside the specified tolerance ranges. There are two fabrication effects that need to be controlled. The first is core separation which is set, not only by the final construction of the twin-core fibre, but also by core concentricity in the precursor preform. In particular, the preform must be straight so that the longitudinal cut remains the required distance from the core for a substantial length of the preform. The second effect is core variability along the length of the preform which influences not only the demultiplexing action but also the strength of coupling between the cores.

A method of aligning the demultiplexer for correct performance may be provided by using some form of post-tuning of the core refractive indices of the cores using ultraviolet processing [99].

The ability of the scalar wave equation solver to handle experimentally measured two-dimensional refractive index data was also shown. This capability is

particularly useful for analyzing non-circularly symmetric fibres as demonstrated above.

The work described in this chapter is ongoing and the poor experimental performance of the demultiplexer was probably due to it being the first attempt at fabrication of a twin-core fibre (or indeed any fibre) to such high tolerances using the fibre manufacturing facilities.

Chapter 6

Some Further Applications and Developments

6.1 Introduction

In this chapter some extensions to the theory presented in Chapters 2 and 3 are developed. These extensions take different lines for the scalar and vector solvers respectively. None of the material presented here has been fully studied and the contents should be perhaps be regarded as indicative of directions of possible future work.

The first extension is the inclusion of nonlinear effects in the scalar wave equation solver via the two-dimensional generalization of the method used by Chiang and Sammut [100] to analyse planar structures. This method is iterative and allows the bound modes of nonlinear waveguides with arbitrary nonlinearity to be computed.

In the second section of this chapter modifications of the vector wave equation are discussed. In particular, a different approach to that taken in Chapter 3 is presented in which the resulting eigenproblem is formulated in such a way as to eliminate spurious modes while still maintaining the same generality of the permittivity tensor allowed previously.

The chapter is concluded with a calculation of the influence of central 'dips' in the refractive index profile on the minor component of the electric field and an experimental arrangement for observation of the effect presented.

6.2 Nonlinear Waveguides

There is considerable current interest in optically nonlinear materials being used to fabricate waveguiding structures. Such structures have many interesting prop-

erties of which the most studied is switching [101]. Other interesting applications include the idea of 'guiding light with light' [102] in which an incident light beam writes a waveguide in a saturable self-focusing nonlinear medium which then acts as a waveguide for the writing beam itself. The medium must be saturable otherwise self-focusing will dominate and the model will exhibit an unphysical singularity in the field [103].

In optical fibres (and glasses in general) the dominant optical nonlinear effect is third order [104]. In general, however, it is of theoretical interest to be able to handle nonlinearities that are essentially arbitrary functions of the local light intensity, I. The most straightforward way of doing this is to introduce an intensity dependent nonlinear dielectric constant given approximately by

$$n^2 = n_l^2 + n_2 n_l f(I) \tag{6.1}$$

where n_l is the linear refractive index, n_2 is the nonlinear coefficient and f() is an arbitrary function. Thus the dielectric constant of a nonlinear material is composed of a linear part and an intensity dependent nonlinear part. In practice nonlinear effects in most materials are small, $n_2 << 1$ and $f(I) \sim I$.

Analytic solutions of the nonlinear scalar wave equation are known for only a few refractive index profiles in self-focusing media: step [105], power law [106] and exponential [107]. In order to handle more general non-linearities, including saturation effects, numerical techniques must be used. In particular, variational methods and finite element methods have been used (see for example [108]). However, such techniques seem to have been used only for the study of slab and rectangular waveguides and not for circular fibre geometries. The method described below can be used for arbitrary fibre geometries due to the generality of the underlying linear wave equation solver.

The method is of course restricted to finding stable solutions (positive slope of the effective index versus power curve) and so switching transition regions, where the modes are highly unstable, cannot be obtained. An extension of the method to this regime would, however, be possible using the technique described in [108].

6.2.1 Formulation

The method proposed by Chiang and Sammut can be readily generalized to two-dimensional fibre geometries because it only involves the repeated solution of a linear waveguide problem. The technique finds bound mode solutions of the scalar wave equation which are, by definition, solutions of Maxwell's equations in the weak guidance limit. Such solutions are usually referred to as solitons because of their particle-like properties.

The bound mode solutions of the scalar wave equation can be written as

$$\varphi(x,y,z,t) = \psi(x,y)\exp[i(\beta z - \omega t)] \tag{6.2}$$

where $\beta = n_{\text{eff}}k$ is the modal propagation constant, ω is the angular frequency of the optical field, $\psi(x,y)$ is the modal field, and propagation occurs in the z-direction. The scalar modal field satisfies the nonlinear scalar wave equation

$$\nabla_t^2 \psi - k^2 \left[n_l^2 + c\varepsilon_0 n_l^2 n_2(x,y) g(\psi^2) - n_{\text{eff}}^2 \right] \psi = 0 \tag{6.3}$$

where the nonlinear refractive index has been written as the sum of a linear part and a nonlinear part in accordance with equation (6.1), ∇_t^2 is the transverse Laplacian operator, c is the speed of light *in vacuo*, ε_0 is the permittivity of free space, $n_2(x,y)$ is the (spatially dependent) nonlinear coefficient, $k = 2\pi/\lambda$ is the free space wavenumber and $g(\psi^2)$ characterizes the nonlinearity.

The modal fields satisfying Equation (6.3) propagate in the z-direction and have a power density, S, given by the magnitude of the Poynting vector in that direction

$$S = \frac{1}{2}\text{Re}\left(\mathbf{E} \times \mathbf{H}^*\right) \cdot \hat{\mathbf{z}} \tag{6.4}$$

where $\mathbf{E}$ is the modal electric field, $\mathbf{H}$ is the modal magnetic field, $\hat{\mathbf{z}}$ is a unit vector in the z-direction, Re denotes the real part and * denotes complex conjugation. The total power carried by a mode is given by

$$P = \frac{1}{2}\int\int \text{Re}\left(\mathbf{E} \times \mathbf{H}^*\right) \cdot \hat{\mathbf{z}}\, dy\, dx \tag{6.5}$$

where the integration is performed over all two-dimensional space.

In the weak guidance approximation the modal fields are uniformly linearly polarised. Without loss of generality assume that the electric field vector is given by

$$\mathbf{E} = \psi\hat{\mathbf{x}} \tag{6.6}$$

where ψ is purely real and $\hat{\mathbf{x}}$ is an x-directed unit vector. Then $\mathbf{H}$, computed from Maxwell's equations, is also purely real and y-directed being given by

$$\mathbf{H} = \frac{\beta\varepsilon_0 c}{k}\psi\hat{\mathbf{y}} \tag{6.7}$$

where ε_0 is the permittivity of free space and $\hat{\mathbf{y}}$ is a y-directed unit vector, whence Equation (6.5) becomes

$$P = \frac{\beta c\varepsilon_0}{2k}\int\int \psi^2(x,y)\, dy\, dx. \tag{6.8}$$

Define a field ψ_0 such that

$$\int\int \psi_0^2(x,y)\, dy\, dx = 1 \tag{6.9}$$

then from Equation (6.8) it follows that

$$\psi = \left(\frac{2kP}{\beta c\varepsilon_0}\right)^{\frac{1}{2}} \psi_0 \tag{6.10}$$

and so the equivalent linear refractive index is defined by

$$n^2(x,y) = n_l^2 \left[1 + c\varepsilon_0 n_2(x,y) g\left(\frac{2kP}{\beta c\varepsilon_0}\psi_0^2\right)\right]. \tag{6.11}$$

Hence the nonlinear scalar wave equation is reduced to linear form,

$$\nabla_t^2 \psi - k^2(n^2 - n_{\text{eff}}^2)\psi = 0. \tag{6.12}$$

Starting from a given power, P, given initial field, ψ, and guessing an initial value of β an iterative process can be used to find nonlinear modes requiring only the solution of the linear wave Equation (6.12). The new values of β and ψ are used to compute an updated $n(x,y)$ via Equation (6.11). The process is continued until successively computed values of β differ by a suitably small amount.

For reasons of computational efficiency all integrations are carried out in configuration space (see Chapter 2), whence Equation (6.8) becomes

$$P = \frac{\beta c\varepsilon_0}{2k}\frac{h^2}{k^2}\left(\psi^\dagger J \psi\right) \tag{6.13}$$

where h is the mesh spacing, J is the Jacobian of the transformation from real space to configuration space and † denotes transposition.

6.2.2 Numerical Examples

Three examples of nonlinear fibre structures are presented below. The first two are primarily for comparative purposes. The details of the fibre geometry for the examples are

Example 1: nonlinear core of radius 1μm embedded in a nonlinear cladding

Example 2: linear core of radius 1μm embedded in a nonlinear cladding

Example 3: linear core of radius 1μm embedded in an annular saturating nonlinear cladding with inner radius 1μm and outer radius 2μm surrounded by a linear outer cladding.

The material properties are the same for all examples: core index 1.57 and cladding index 1.55. The nonlinearity is of the Kerr type, i.e.

$$g(\psi^2) = \psi^2, \tag{6.14}$$

and $n_2 = 10^{-9}\mathrm{m}^2/\mathrm{W}$. These values correspond to a fibre composed of MBBA liquid crystal. In example 3 the refractive index saturates at 1.58.

The wavelength of operation used in all examples is 0.515μm and the underlying linear wave equation is solved on a 100×100 finite difference grid. In all cases the fundamental mode (LP_{01}) is being sought.

Example 1: Nonlinear Core and Cladding

Figure 6.1 shows the dispersion (effective index versus power) curve for a

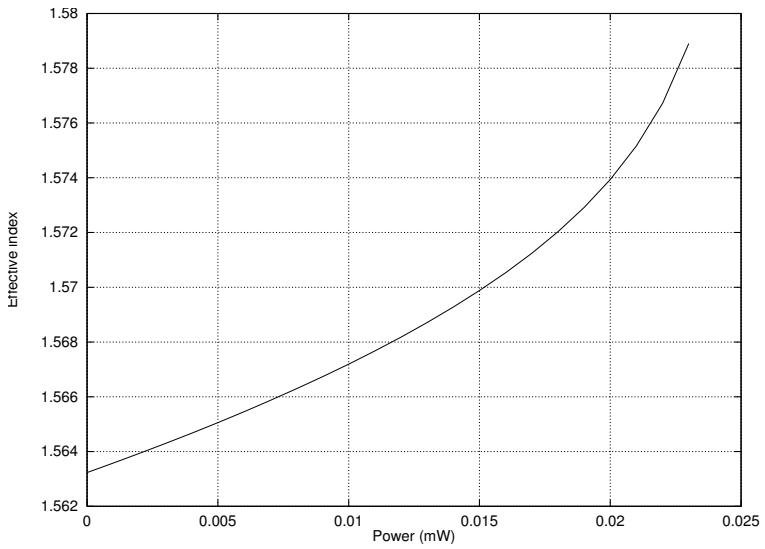

Figure 6.1: Effective index versus power curve for Example 1

fibre composed of a nonlinear core and cladding. The starting field was a Gaussian centred at the origin.

The values computed agree with results calculated by Chiang [109] using the radial wave equation. No additional branches due to switching or other phenomena occur because the refractive indices simply become larger and self-focusing eventually forces the fields to become vanishingly small in extent and infinitely large in amplitude.

Above 0.23mW convergence to a stable effective index value does not occur due to self-focusing effects.

Example 2: Linear Core and Nonlinear Cladding

The dispersion curve (effective index versus power) for a fibre composed of a linear core embedded in a nonlinear cladding is shown in Figure 6.2. Again, these results agree with those of Chiang with the exception of the vertical branch (shown dashed in Figure 6.2). This branch corresponds to the appearance of annular modes directly analogous to the asymmetric modes found in nonlinear slab waveguides and cannot be found by the current method even when the iterative procedure is started with a non-centrally placed Gaussian or an annular field. There are several possible reasons why these modes do not appear. The most likely candidates are numerical instability in the eigensolver arising from discretization of a circular geometry on a square grid or that the modes are physically unstable and simply self-focus away. Such azimuthal self-focusing may be a real physical effect artificially excluded from Chiang's simulation by the assumption of a purely radial field. Work in this area is ongoing.

Convergence of the horizontal branch at power levels greater than 0.253mW was not observed. This power is slightly lower than the value of 0.261mW computed by Chiang. In either case non-convergence is simply evidence of the algorithm failing in the physically unstable regime.

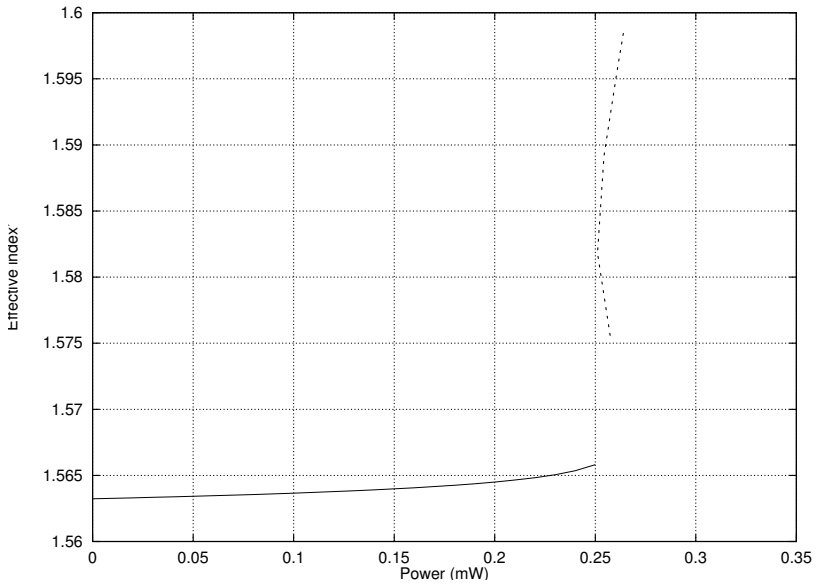

Figure 6.2: Effective index versus power curve for Example 2. The dashed curve shows schematically an additional branch found by Chiang but not with the current method.

Example 3: Linear Core with Surrounding Annular Nonlinear Inner Cladding and Outer Linear Cladding

The effect of a saturating nonlinearity is to provide stability to both the underlying physical problem and the numerical problem being solved as may be seen by recalling that there are no stable soliton solutions in a two-dimensional (or higher) self-focusing medium.

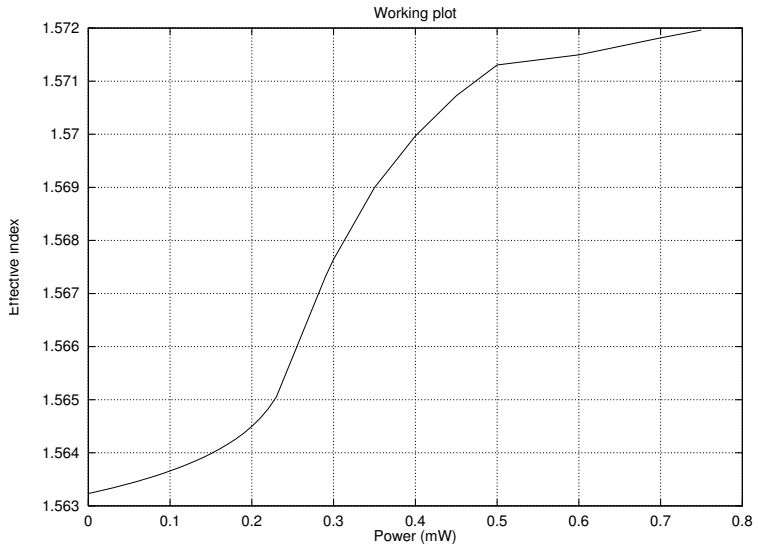

Figure 6.3: Effective index versus power curve for Example 3

The dispersion curve (effective index versus power) shown in Figure 6.3 has three clear branches although they are all linked smoothly *and* stably. The lower horizontal section corresponds to guidance primarily by the central linear core. Between 0.21mW and 0.5mW the field is annular—the refractive index of the inner cladding being greater than 1.57. At powers of 0.5mW and greater the field splits into two separate peaks symmetrically placed about the line $x = 0$ (or $y = 0$). The reason for the breakup of the annular mode is not clear.

It should also be pointed out that the starting field was in all cases a centrally placed Gaussian although searches for additional branches were carried out using an annular starting field at power levels between 0.2 and 0.5mW .

6.2.3 Conclusion

The method presented above appears to be able to converge to all unquestionably stable solutions of the nonlinear scalar wave equation in an optical fibre. Since no unphysical boundary conditions (such as the symmetry boundary condition)

are applied or can be applied easily the method cannot be forced to converge to unstable solutions. A proof that all the solutions obtained are physically real is a long term goal.

Future work in this area will include study of the behaviour of higher order modes (in particular the LP_{11} mode) and nonlinear modal behaviour in materials which exhibit different forms of saturation than that used in Example 3. It would also be of interest to examine the vector corrections to the scalar nonlinear solutions by treating the final form of the induced refractive index as a perturbation of the zero-power refractive index. Such an approach would, of course, only be valid at low power levels where the nonlinear index differs only slightly from the zero-power index.

6.3 Alternative Treatment of the Vector Wave Equation

The major problem with the form of the wave equation presented in Chapter 3 is the presence of spurious modes in the spectrum. Although these are practically eliminated by using a Rayleigh quotient iteration scheme to solve the resulting numerical eigenproblem it would be more convenient if the spurious modes were explicitly eliminated in the analytic formulation.

6.3.1 Elimination of Spurious Modes

It is well known [110] that spurious modes can be eliminated by explicitly enforcing the divergence condition,

$$\nabla \cdot \mathbf{D} = 0. \tag{6.15}$$

This condition is in fact automatically satisfied by Maxwell's equations at all non-zero frequencies. Such an approach has been used by Marcuse [111] to formulate a Galerkin method for solving the vector wave equation in an inhomogeneous isotropic optical fibre. Marcuse's method is a direct extension of the scalar technique presented by Henry and Verbeek [29].

Marcuse considers only isotropic waveguides; however, the generalization to anisotropic media in which the permittivity tensor has the form given in Equation (3.11), *viz*

$$\varepsilon = \begin{pmatrix} \varepsilon_{11} & \varepsilon_{12} & 0 \\ \varepsilon_{21} & \varepsilon_{22} & 0 \\ 0 & 0 & \varepsilon_{33} \end{pmatrix} \tag{6.16}$$

is straightforward. The displacement current vector, D, now involving coupling

between the field components:

$$\begin{aligned}\mathbf{D} &= \varepsilon\mathbf{E} \\ &= \begin{pmatrix} \varepsilon_{11}E_x + \varepsilon_{12}E_y \\ \varepsilon_{21}E_x + \varepsilon_{22}E_y \\ \varepsilon_{33}E_z \end{pmatrix}. \end{aligned} \tag{6.17}$$

Further, assuming the guide is translationally invariant in the z-direction, the modal solutions have a z-dependence of the form $\exp(i\beta z)$ and so

$$\frac{\partial}{\partial z} \to i\beta. \tag{6.18}$$

Substituting into Equation (6.15) and rearranging gives

$$\begin{aligned} E_z &= -\frac{i}{\beta\varepsilon_{33}}\left[\frac{\partial}{\partial x}(\varepsilon_{11}E_x + \varepsilon_{12}E_y) + \frac{\partial}{\partial y}(\varepsilon_{21}E_x + \varepsilon_{22}E_y)\right] \\ &= -\frac{i}{\beta\varepsilon_{33}}\nabla_t \cdot (\varepsilon_t \mathbf{E}_t) \end{aligned} \tag{6.19}$$

where

$$\nabla_t = \left(\frac{\partial}{\partial x}, \frac{\partial}{\partial y}\right)$$

is the transverse gradient operator and

$$\varepsilon_t = \begin{pmatrix} \varepsilon_{11} & \varepsilon_{12} \\ \varepsilon_{21} & \varepsilon_{22} \end{pmatrix}$$

is the transverse permittivity tensor. Thus, the z-component of the electric field can be expressed in terms of the transverse field components. For more general permittivity tensors such an expression cannot be obtained due to the presence of transverse derivatives (i.e., involving $\frac{\partial}{\partial x}$ and $\frac{\partial}{\partial y}$) of E_z.

Writing the vector wave equation in the natural way

$$\nabla^2\mathbf{E} - \nabla(\nabla \cdot \mathbf{E}) = -k^2\varepsilon\mathbf{E} \tag{6.20}$$

and considering only the x- and y-components (the z-component being calculable from Equation (6.19)) gives

$$\begin{aligned}\left(\frac{\partial}{\partial x} + \frac{\partial}{\partial y}\right)E_x - \frac{\partial}{\partial x}\left[\nabla_t \cdot \mathbf{E}_t - \frac{1}{\varepsilon_{33}}P(x,y)\right] \\ +k^2(\varepsilon_{11}E_x + \varepsilon_{12}E_y) = \beta^2 E_x \end{aligned} \tag{6.21}$$

$$\left(\frac{\partial}{\partial x}+\frac{\partial}{\partial y}\right)E_y-\frac{\partial}{\partial y}\left[\nabla_t\cdot\mathbf{E}_t-\frac{1}{\varepsilon_{33}}P(x,y)\right]$$
$$+k^2(\varepsilon_{21}E_x+\varepsilon_{22}E_y)=\beta^2E_y \tag{6.22}$$

where

$$P(x,y)=\frac{\partial}{\partial x}(\varepsilon_{11}E_x+\varepsilon_{12}E_y)+\frac{\partial}{\partial y}(\varepsilon_{21}E_x+\varepsilon_{22}E_y).$$

These reduce to the form presented by Marcuse for the isotropic case as may be seen by replacing ε_{11}, ε_{22} and ε_{33} by n^2—the square of the refractive index—and setting $\varepsilon_{12}=\varepsilon_{21}=0$ in which case the term in square brackets in Equations (6.21) and (6.22) becomes

$$\begin{aligned}P(x,y) &= -\frac{2}{n}\left(\frac{\partial n}{\partial x}E_x+\frac{\partial n}{\partial y}E_y\right)\\ &= -2\left(\frac{\partial \ln(n)}{\partial x}E_x+\frac{\partial \ln(n)}{\partial x}E_y\right).\end{aligned} \tag{6.23}$$

The system is therefore reduced to the simpler form

$$\begin{aligned}\left(\frac{\partial}{\partial x}+\frac{\partial}{\partial y}\right)E_x+2\frac{\partial}{\partial x}\left(\frac{\partial \ln(n)}{\partial x}E_x+\frac{\partial \ln(n)}{\partial x}E_y\right)+k^2n^2E_x &= \beta^2E_x\\ \left(\frac{\partial}{\partial x}+\frac{\partial}{\partial y}\right)E_y+2\frac{\partial}{\partial y}\left(\frac{\partial \ln(n)}{\partial x}E_x+\frac{\partial \ln(n)}{\partial x}E_y\right)+k^2n^2E_y &= \beta^2E_y\end{aligned} \tag{6.24}$$

Equations (6.21) and (6.22) explicitly include the divergence condition and so will not exhibit any spurious modes. It is also evident that they contain spatial derivatives of the elements of the permittivity tensor which will give rise to delta functions in the case of waveguides with step discontinuities in the refractive index distribution. Consequently this formulation will also be sensitive to noise in the refractive index data.

6.3.2 Discussion and Conclusion

Solution of the system of coupled partial differential equations could be accomplished using a finite difference scheme identical to that used in Chapter 3 and would give rise to a non-symmetric generalized eigenproblem of order $2(N-1)^2$ if discretized on an $(N-1)\times(N-1)$ finite difference mesh. Hence the problem is two-thirds the size of that solved in Chapter 3 and it is the additional $(N-1)^2$ eigenvalues that are present in the original formulation that account for the spurious modes. It is not possible to solve a non-symmetric (generalized or ordinary) eigenproblem using Rayleigh quotient iteration and use must be made of

a specialized method such as the non-symmetric Lanczos algorithm or Arnoldi's method [45]. With a view towards implementing such a scheme it is useful to point out that the non-symmetric form of the wave equation does not have complex eigenpairs. On physical grounds ε (and hence ε_t) is a real symmetric matrix for a lossless non-gyrotropic medium and E_x and E_y are real by construction. The eigenvalues corresponding to bound modes will all lie in the range $k^2 n_{cl}^2 \leq \beta^2 \leq k^2 n_{co}^2$. Such a scheme has recently been used to solve the wave equation in slab dielectric waveguides [112].

Alternatively, the Galerkin method could be generalized to the anisotropic case. Nonlinear scaling can be used to extend the range of the method to include the ability of finding modal cutoff. For arbitrarily shaped waveguides, however, numerical integration must be used to compute the matrix elements arising in the Galerkin formulation.

On a more speculative note it would appear that the solution of the vector wave equation with a more general permittivity tensor than the one used in the present work would be all but impossible using finite difference or finite element methods simply because of the lack of methods for solving the fully complex generalized eigenproblem. The transformation from the complex matrix representation to the real matrix representation by doubling the size of the matrix is still mathematically feasible but again solving a large sparse non-symmetric real generalized eigenproblem lies outside the scope of current numerical eigenproblem solvers. It therefore seems likely that generalizations of the Galerkin method or Rayleigh method [113] may be more fruitful areas to explore.

6.4 The Effect of Refractive Index Dips on Minor Field Structure

The vast majority of optical fibres are manufactured using the modified chemical vapour deposition system. This system allows for considerable automation and so is viable for fibre mass production and from the researchers point of view it allows relatively straightforward production of fibres for special purposes due to the ease with which dopant materials such as erbium or boron may be introduced into the core or cladding regions. It is, however, difficult (if not impossible) to produce true step refractive index profiles due to thermally induced diffusion at the core-cladding interface. A more interesting departure from the ideal step-index core is the presence of a central dip in the refractive index profile due to the boil off of the more volatile constituents (usually germanium) of the core during preform collapse. These central refractive index dips are certainly present in the preform but owing to the low spatial resolution of fibre profilers the dips cannot

be unambiguously measured in the fibre.

Numerical studies of the influence of the dip on propagation characteristics have been performed by Gambling, *et al.* [114] where the core was modelled as a step index with a power-law central dip. Earlier Stolen [115] considered the case of a ring waveguide which can be viewed as the simplest possible model of a refractive index profile with a central dip. Both of these works use scalar analysis so no information on the minor field components is available. Also, neither take into account the smooth transition at the core-cladding interface. However, the effect of the dip on spot size, second mode cutoff [116] and near and far field radiation patterns were all calculated.

6.4.1 Core Model

In order to model a real (preform) refractive index profile more closely it is convenient to Gaussian filter (see Section 3.5.1) a refractive index distribution constructed from line segments. The normalized refractive index difference, Δn, prior to smoothing is given by

$$\Delta n(R) = \begin{cases} 4(1-\alpha)R + \alpha & 0 \leq R < \frac{1}{4} \\ 1 & \frac{1}{4} \leq R < \frac{1}{2} \\ 0 & R \geq \frac{1}{2} \end{cases} \tag{6.25}$$

where α is a parameter between 0 and 1 that determines the depth of the central dip, reducing to a step-index profile for $\alpha = 1$ and R is the normalized radius; the core cladding interface being at $R = \frac{1}{2}$.

The smoothing parameter, σ, used to set the width of the Gaussian filter was set to 0.05 in all cases considered in order that the smoothing be uniform across the profiles examined. The core radius ($R = \frac{1}{2}$) was scaled to 4μm and the peak refractive index difference scaled to 0.005. The parameter α was varied from zero (for which the central dip extends down to the cladding) to unity in steps of 0.25. The normalized smoothed refractive index functions are shown in Figure 6.4. Calculations were carried out at 1.3μm where all the structures are singlemoded. A 100×100 finite difference grid was used throughout. The modal fields examined are nominally x-polarised, that is, the major field component is x-directed.

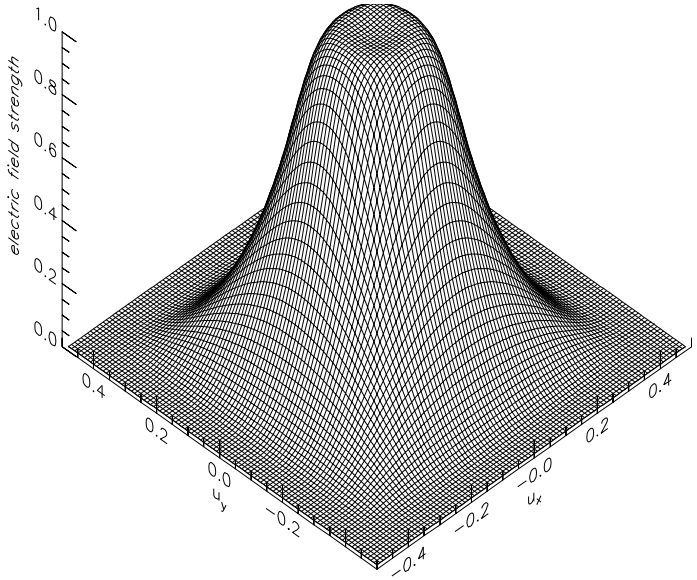

Figure 6.4: Normalized smoothed refractive index difference functions

6.4.2 Numerical Results

Effective indices were computed using both scalar and vector programs for comparative purposes and the results are shown in Table 6.1. The fourth column of the table indicates whether a depression was visible in the major field component.

α	scalar	vector	depression?
0.00	1.448914	1.448913	yes
0.25	1.449036	1.449035	yes
0.50	1.449166	1.449165	yes
0.75	1.449037	1.449036	just visible

Table 6.1: Effective indices computed for a range of α values

From the table it is apparent that the effective index decreases as the depth of the dip increases. This is to be expected because with increasing dip depth the guiding region becomes smaller and the modal fields will be less strongly bound.

The presence of a central depression in the major field component is to be expected because the electromagnetic field will tend to hug the regions of elevated index. The main effect on the scalar field (which is almost identical in shape to the major field) is to flatten the peak as shown clearly in figure 3 of reference [114].

For comparison with the present work cross sections through the major field components of the electric field for $\alpha = 0.00$ and $\alpha = 1.00$ are shown in Figure 6.5. It is also to be noted that the central depression in the major field component is much more evident in the current work a fact largely due to the use of a more realistic refractive index distribution.

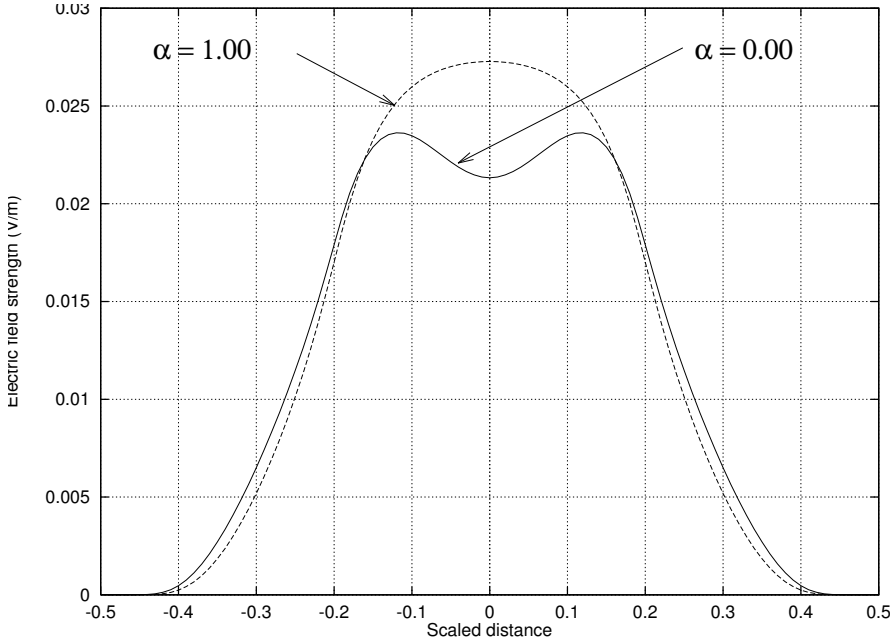

Figure 6.5: Central cross-section through major field component for $\alpha = 0.00$ and $\alpha = 1.00$

Figures 6.6 through 6.8 show the minor electric field component as α varies from 0.00 (deep dip) to 1.00 (no dip). The plots are shown side on in order to clearly show the field amplitudes.

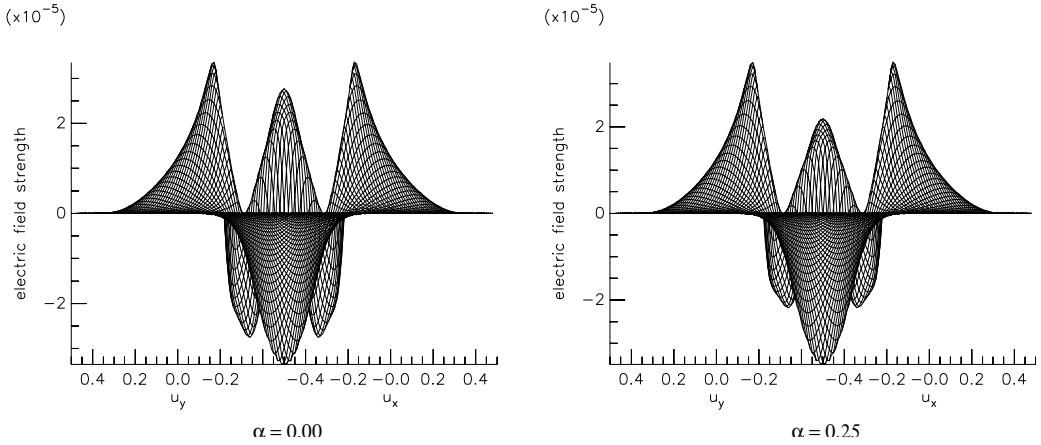

Figure 6.6: Minor field components for $\alpha = 0.00$ and $\alpha = 0.25$

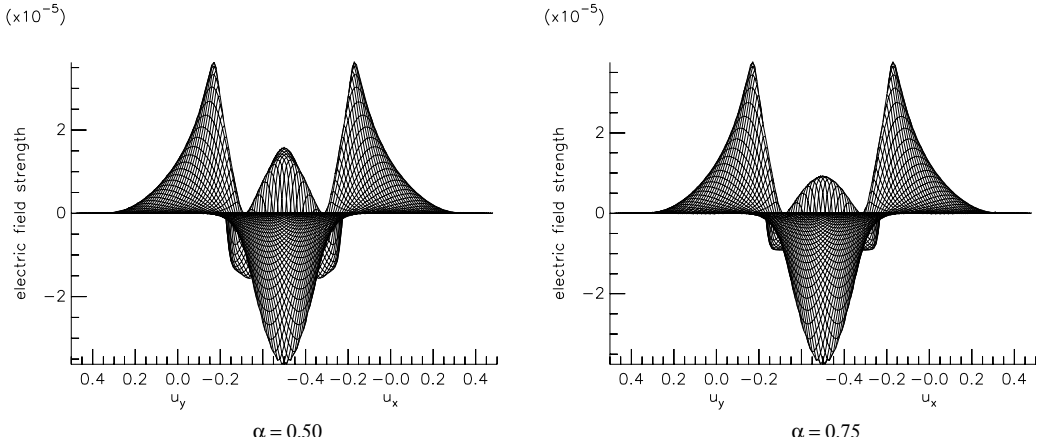

Figure 6.7: Minor field components for $\alpha = 0.50$ and $\alpha = 0.75$

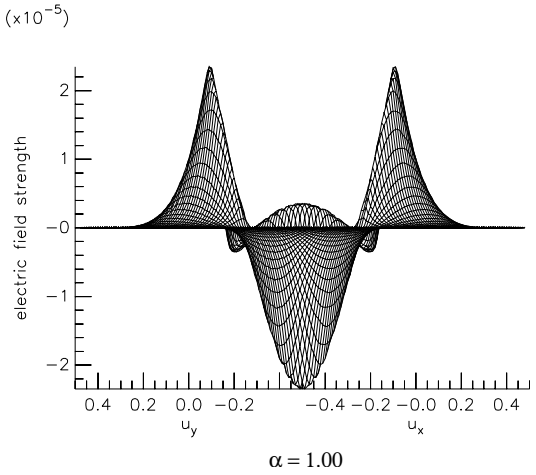

Figure 6.8: Minor field component for $\alpha = 1.00$

The marked increase in amplitude of the internal peaks (an internal peak lies inside the nominal core-cladding boundary) is clearly in evidence. In fact the internal peak for $\alpha = 0.00$ has an amplitude roughly five times that when $\alpha = 1.00$ and just 10% less than the peak amplitude. This compares with the depression of roughly 10% of the peak value of the major field when $\alpha = 0.00$ as clearly seen in Figure 6.5. It therefore follows that the minor field component is much more sensitive to changes in refractive index profile than the major field component. Additional evidence in support of this statement comes from the smoothing of the refractive index distributions required by the vector solver—the minor field component becomes extremely ragged if the profiles are left unsmoothed.

Due to the extreme sensitivity of the minor field component to refractive index variation it may perhaps be possible to indirectly probe the refractive index distribution through changes in the minor field. However, measurement may be difficult owing to the relative size of the major and minor field components (the major field is 1000 times larger in amplitude than the minor field in the examples presented here).

6.4.3 Proposed Experiment

The additional structure in the minor field should be able to be observed experimentally using the arrangement shown in Figure 6.9. Such an experiment has been performed in the visible with a fibre of the stress-induced birefringent type (bow-tie fibre) [85]. In a fibre of this type the minor field is down by only 15dB in amplitude compared to the major field making the polariser requirements less severe. In this case the polariser must be of high quality in order to provide at

least 60dB suppression of the orthogonally polarised field. Of course, the lower amplitude of E_y in the ordinary fibre could be partially compensated by using a higher power laser source.

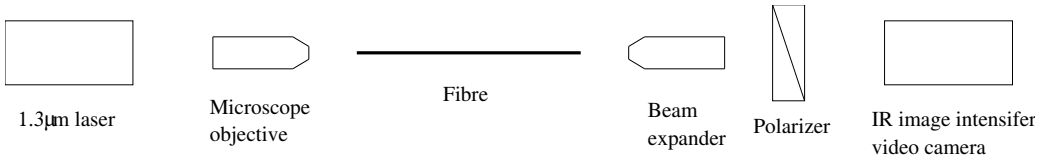

Figure 6.9: Schematic arrangement for proposed experiment

The microscope objective and beam expander must be made from stress-free optical elements in order to prevent coupling of the x- and y-fields via the stress-optic effect and the fibre must be kept as straight as possible in order to minimize bending effects.

6.4.4 Conclusion

The minor field component obtained as part of the solution of the vector wave equation has a much richer structure than the major field component. The fine structure arises from the sensitivity of the minor field to the form of the permittivity distribution. In particular, it is the minor field that exhibits the first signs of noise in a numerical simulation a fact attributable not only to its small relative magnitude but also to its sensitivity to noise on the permittivity distribution. The smoothness of the minor field component produced by a vector wave equation solver may therefore be viewed as a direct test of the solvers quality.

Experimentally, the minor field is hard to see. However, it carries the bulk of the information concerning details of the underlying fibre refractive index profile. Eventually experimentally measured minor fields may provide additional quantitative information of interest to fibre designers and fabricators.

Bibliography

[1] Lord Rayleigh, XVIII. On the passage of electric waves through tubes, or the vibrations of dielectric cylinders, *The London, Edinburgh, and Dublin Philosophical Magazine and Journal of Science* 43 (261) (1897) 125–132. doi:10.1080/14786449708620969.

[2] D. Hondros, P. Debye, Elektromagnetische Wellen an dielektrischen Drähten, *Annalen der Physik* 337 (8) (1910) 465–476. doi:10.1002/andp.19103370802.

[3] H. Zahn, Über den Nachweis elektromagnetischer Wellen an dielektrischen Drähten, *Annalen der Physik* 354 (8) (1916) 907–933. doi:10.1002/andp.19163540803.

[4] O. Schriever, Elektromagnetische Wellen an dielektrischen Drähten, *Annalen der Physik* 368 (23) (1920) 645–673. doi:10.1002/andp.19203682304.

[5] L. Bergmann, L. Krügel, Messungen im Strahlungsfeld einer im Innern eines metallischen Hohlzylinders erregten Linearantenne, *Annalen der Physik* 413 (2) (1934) 113–138. doi:10.1002/andp.19344130202.

[6] J. R. Carson, S. P. Mead, S. A. Schelkunoff, Hyper-Frequency Wave Guides-Mathematical Theory, *Bell System Technical Journal* 15 (2) (1936) 310–333. doi:10.1002/j.1538-7305.1936.tb00734.x.

[7] G. C. Southworth, Hyper-Frequency Wave Guides-General Considerations and Experimental Results, *Bell System Technical Journal* 15 (2) (1936) 284–309. doi:10.1002/j.1538-7305.1936.tb00733.x.

[8] W. Barrow, Transmission of Electromagnetic Waves in Hollow Tubes of Metal, *Proceedings of the IRE* 24 (10) (1936) 1298–1328. doi:10.1109/JRPROC.1936.227357.

[9] J. A. Stratton, *Electromagnetic Theory*, International Series in Physics, McGraw-Hill, New York, 1941.

[10] H. H. Hopkins, N. S. Kapany, A Flexible Fibrescope, using Static Scanning, *Nature* 173 (4392) (1954) 39–41. doi:10.1038/173039b0.

[11] A. C. S. Van Heel, A New Method of transporting Optical Images without Aberrations, *Nature* 173 (4392) (1954) 39. doi:10.1038/173039a0.

[12] H. Hopkins, N. Kapany, Transparent Fibres for the Transmission of Optical Images, *Optica Acta: International Journal of Optics* 1 (4) (1955) 164–170. doi:10.1080/713818685.

[13] N. S. Kapany, Fiber Optics Part I Optical Properties of Certain Dielectric Cylinders, *Journal of the Optical Society of America* 47 (5) (1957) 413–422. doi:10.1364/JOSA.47.000413.

[14] N. S. Kapany, J. A. Eyer, R. E. Keim, Fiber Optics Part II Image Transfer on Static and Dynamic Scanning with Fiber Bundles, *Journal of the Optical Society of America* 47 (5) (1957) 423–427. doi:10.1364/JOSA.47.000423.

[15] E. Snitzer, Cylindrical Dielectric Waveguide Modes, *Journal of the Optical Society of America* 51 (5) (1961) 491–498. doi:10.1364/JOSA.51.000491.

[16] D. Gloge, Optical waveguide transmission, *Proceedings of the IEEE* 58 (10) (1970) 1513–1522. doi:10.1109/PROC.1970.7976.

[17] A. Snyder, Asymptotic Expressions for Eigenfunctions and Eigenvalues of a Dielectric or Optical Waveguide, *IEEE Transactions on Microwave Theory and Techniques* 17 (12) (1969) 1130–1138. doi:10.1109/TMTT.1969.1127112.

[18] D. Gloge, Weakly Guiding Fibers, *Applied Optics* 10 (10) (1971) 2252–2258. doi:10.1364/AO.10.002252.

[19] H. Motz, Calculation of the electromagnetic field, frequency and circuit parameters of high-frequency resonator cavities, *Journal of the Institution of Electrical Engineers - Part III: Radio and Communication Engineering* 93 (25) (1946) 335–343. doi:10.1049/ji-3-2.1946.0054.

[20] A. W. Snyder, J. D. Love, *Optical Waveguide Theory*, Chapman and Hall, London, 1983.

[21] R. Sammut, C. Pask, Simplified numerical analysis of optical fibres and planar waveguides, *Electronics Letters* 17 (3) (1981) 105–106. doi:10.1049/el:19810074.

[22] W. L. Mammel, L. G. Cohen, Numerical prediction of fiber transmission characteristics from arbitrary refractive-index profiles, *Applied Optics* 21 (4) (1982) 699–703. doi:10.1364/AO.21.000699.

[23] L. G. Cohen, W. L. Mammel, H. M. Presby, Correlation between numerical predictions and measurements of single-mode fiber dispersion characteristics, *Applied Optics* 19 (12) (1980) 2007–2010. doi:10.1364/AO.19.002007.

[24] D. G. Geers, I. M. Bassett, S. J. Hewlett, Numerical characterization of twin-core fibre: Scalar and vector solutions, in: *18th Australian Conference on Optical Fibre Technology (ACOFT-18'93): Proceedings*, Institution of Radio and Electronics Engineers Australia, 1993, pp. 348–351.

[25] Kin Chiang, Finite element analysis of weakly guiding fibers with arbitrary refractive-index distribution, *Journal of Lightwave Technology* 4 (8) (1986) 980–990. doi:10.1109/JLT.1986.1074842.

[26] L. S. Tamil, G. H. Aicklen, Analysis of optical fibers with arbitrary refractive index profiles: Accuracy, convergence, and effects of finite cladding, *Optics Communications* 99 (5-6) (1993) 393–404. doi:10.1016/0030-4018(93)90349-A.

[27] S. Seki, T. Yamanaka, K. Yokoyama, Two-dimensional analysis of optical waveguides with a nonuniform finite difference method, *IEE Proceedings J Optoelectronics* 138 (2) (1991) 123–127. doi:10.1049/ip-j.1991.0022.

[28] C. Vassallo, Improvement of finite difference methods for step-index optical waveguides, *IEE Proceedings J Optoelectronics* 139 (2) (1992) 137–142. doi:10.1049/ip-j.1992.0024.

[29] C. Henry, B. Verbeek, Solution of the scalar wave equation for arbitrarily shaped dielectric waveguides by two-dimensional Fourier analysis, *Journal of Lightwave Technology* 7 (2) (1989) 308–313. doi:10.1109/50.17772.

[30] M. Vlassis and R. C. McPhedran, Private Communication, (1993).

[31] K. S. Chiang, Review of numerical and approximate methods for the modal analysis of general optical dielectric waveguides, *Optical and Quantum Electronics* 26 (3) (1994) S113–S134. doi:10.1007/BF00384667.

[32] M. Koshiba, K. Hayata, M. Suzuki, Vectorial finite-element method without spurious solutions for dielectric waveguide problems, *Electronics Letters* 20 (10) (1984) 409–410. doi:10.1049/el:19840283.

[33] K. Hayata, M. Koshiba, M. Eguchi, M. Suzuki, Novel finite-element formulation without any spurious solutions for dielectric waveguides, *Electronics Letters* 22 (6) (1986) 295–296. doi:10.1049/el:19860201.

[34] A. Bermúdez, D. G. Pedreira, Mathematical analysis of a finite element method without spurious solutions for computation of dielectric waveguides, *Numerische Mathematik* 61 (1) (1992) 39–57. doi:10.1007/BF01385496.

[35] M. Koshiba, K. Hayata, M. Suzuki, Finite-element solution of anisotropic waveguides with arbitrary tensor permittivity, *Journal of Lightwave Technology* 4 (2) (1986) 121–126. doi:10.1109/JLT.1986.1074687.

[36] B. Rahman, J. Davies, Penalty Function Improvement of Waveguide Solution by Finite Elements, *IEEE Transactions on Microwave Theory and Techniques* 32 (8) (1984) 922–928. doi:10.1109/TMTT.1984.1132789.

[37] M. Koshiba, S. Maruyama, K. Hirayama, A vector finite element method with the high-order mixed-interpolation-type triangular elements for optical waveguiding problems, *Journal of Lightwave Technology* 12 (3) (1994) 495–502. doi:10.1109/50.285332.

[38] Ching-Chuan Su, Chun Hsiiung Chen, Calculation of Propagation Constants and Cutoff Frequencies of Radially Inhomogeneous Optical Fibers, *IEEE Transactions on Microwave Theory and Techniques* 34 (3) (1986) 328–332. doi:10.1109/TMTT.1986.1133339.

[39] J.-D. Decotignie, O. Parriaux, F. Gardiol, Birefringence Properties of Twin-Core Fibers by Finite Differences, *Journal of Optical Communications* 3 (1) (1982) 8–12. doi:10.1515/JOC.1982.3.1.8.

[40] M. Stern, Semivectorial polarised finite difference method for optical waveguides with arbitrary index profiles, *IEE Proceedings J Optoelectronics* 135 (1) (1988) 56–63. doi:10.1049/ip-j.1988.0013.

[41] M. Stern, Semivectorial polarised $\tilde{\mathrm{H}}$ field solutions for dielectric waveguides with arbitrary index profiles, *IEE Proceedings J Optoelectronics* 135 (5) (1988) 333–338. doi:10.1049/ip-j.1988.0062.

[42] P. Clarricoats, K. Chan, Electromagnetic-wave propagation along radially inhomogeneous dielectric cylinders, *Electronics Letters* 6 (22) (1970) 694–695. doi:10.1049/el:19700482.

[43] K. Lo, R. McPhedran, I. Bassett, G. Milton, An electromagnetic theory of dielectric waveguides with multiple embedded cylinders, *Journal of Lightwave Technology* 12 (3) (1994) 396–410. doi:10.1109/50.285321.

[44] K. M. Lo, Analysis of optical fibres with multiple radially inhomogeneous cylinders, *Journal of the Optical Society of America B,* submitted, (1994).

[45] Y. Saad, *Numerical Methods for Large Eigenvalue Problems*, Manchester University Press Series in Algorithms and Architectures for Advanced Scientific Computing, Manchester University Press, Manchester, 1992.

[46] J. Reid, On the method of conjugate gradients for the solution of large sparse systems of linear equations, in: J. Reid (Ed.), *Large Sparse Sets of Linear Equations*, The Institute of Mathematics and Its Applications, Academic Press, London, 1971.

[47] G. H. Golub, C. F. Van Loan, *Matrix Computations*, 2nd Edition, Johns Hopkins Studies in the Mathematical Sciences, Johns Hopkins University Press, Baltimore, MD, 1989.

[48] D. J. Rose, A Graph-Theoretic Study of the Numerical Solution of Sparse Positive Definite Systems of Linear Equations, in: *Graph Theory and Computing*, Elsevier, 1972, pp. 183–217. doi:10.1016/B978-1-4832-3187-7.50018-0.

[49] A. George, J. W. Liu, The Evolution of the Minimum Degree Ordering Algorithm, *SIAM Review* 31 (1) (1989) 1–19. doi:10.1137/1031001.

[50] Alan George, Joseph W-H. Liu, *Computer Solution of Large Sparse Positive Definite Systems*, Prentice-Hall, Englewood Cliifs, NJ, 1981.

[51] I. S. Duff, A. M. Erisman and J. K. Reid, *Direct Methods for Sparse matrices*, Clarendon Press, Oxford, 1986.

[52] I. S. Duff, J. K. Reid, The Multifrontal Solution of Indefinite Sparse Symmetric Linear, *ACM Transactions on Mathematical Software* 9 (3) (1983) 302–325. doi:10.1145/356044.356047.

[53] I. S. Duff, J. K. Reid, The Multifrontal Solution of Unsymmetric Sets of Linear Equations, *SIAM Journal on Scientific and Statistical Computing* 5 (3) (1984) 633–641. doi:10.1137/0905045.

[54] B. M. Irons, A frontal solution program for finite element analysis, *International Journal for Numerical Methods in Engineering* 2 (1) (1970) 5–32. doi:10.1002/nme.1620020104.

[55] P. Hood, Frontal solution program for unsymmetric matrices, *International Journal for Numerical Methods in Engineering* 10 (2) (1976) 379–399. doi:10.1002/nme.1620100209.

[56] Richard Barrett, Michael Berry, Tony Chan, James Demmel, June Donato, Jack Dongarra, Victor Eijkhout, Roldan Pozo, Charles Romine and Henk van der Vorst, *Templates for the Solution of Linear Systems: Building Blocks for Iterative Methods*, SIAM, Philadelphia, PA, 1993.

[57] C. Lanczos, An iteration method for the solution of the eigenvalue problem of linear differential and integral operators, *Journal of Research of the National Bureau of Standards* 45 (4) (1950) 255–282. doi:10.6028/jres.045.026.

[58] W. E. Arnoldi, The principle of minimized iterations in the solution of the matrix eigenvalue problem, *Quarterly of Applied Mathematics* 9 (1) (1951) 17–29. doi:10.1090/qam/42792.

[59] Beresford N. Parlett, *The Symmetric Eigenvalue Problem*, Prentice-Hall, Englewood Cliifs, N.J., 1980.

[60] E. Jaunart, P. Megret, J. Froidure, P. Crahay, M. Blondel, M. Lamquin, Influence of refractive index measurement accuracy on single-mode optical fiber modeling, *IEEE Photonics Technology Letters* 4 (11) (1992) 1282–1284. doi:10.1109/68.166969.

[61] L. F. Richardson, IX. The approximate arithmetical solution by finite differences of physical problems involving differential equations, with an application to the stresses in a masonry dam, *Philosophical Transactions of the Royal Society of London. Series A, Containing Papers of a Mathematical or Physical Character* 210 (459-470) (1911) 307–357. doi:10.1098/rsta.1911.0009.

[62] Roger G. Grimes, John G. Lewis, Horst Simon, A shifted block lanczos algorithm for solving sparse symmetric generalized eigenproblems, Tech. Rep. AMS-TR-166, Boeing Computer Services, Applied Mathematics and Statistics P.O. Box 24346 Seattle Washington 98124–0346 (July 1991).

[63] William H. Press, Saul A. Teukolosky, William T. Vetterling, Brian P. Flannery, *Numerical Recipes in C*, 2nd Edition, Cambridge University Press, London, 1992.

[64] J. G. Herriot, C. H. Reinsch, Algorithm 507: Procedures for Quintic Natural Spline Interpolation [E1], *ACM Transactions on Mathematical Software* 2 (3) (1976) 281–289. doi:10.1145/355694.355701.

[65] I. H. Malitson, Interspecimen Comparison of the Refractive Index of Fused Silica, *Journal of the Optical Society of America* 55 (10) (1965) 1205–1209. doi:10.1364/JOSA.55.001205.

[66] B. Ainslie, C. Day, A review of single-mode fibers with modified dispersion characteristics, *Journal of Lightwave Technology* 4 (8) (1986) 967–979. doi:10.1109/JLT.1986.1074843.

[67] D. Payne, W. Gambling, New silica-based low-loss optical fibre, *Electronics Letters* 10 (15) (1974) 289–290. doi:10.1049/el:19740231.

[68] L. D. Landau, E. M. Lifshitz, L. P. Pitaevski, *Electrodynamics of Continuous Media*, 2nd Edition, Vol. 8 of *Landau and Lifshitz Course of Theoretical Physics*, Pergamon, London, 1984.

[69] Pak Chu, R. Sammut, Analytical method for calculation of stresses and material birefringence in polarization-maintaining optical fiber, *Journal of Lightwave Technology* 2 (5) (1984) 650–662. doi:10.1109/JLT.1984.1073673.

[70] J. H. Wilkinson, *The Algebraic Eigenvalue Problem*, Monographs on Numerical Analysis, Oxford University Press, Oxford, 1965.

[71] X.-H. Zheng, W. Henry, A. Snyder, Polarization characteristics of the fundamental mode of optical fibers, *Journal of Lightwave Technology* 6 (8) (1988) 1300–1305. doi:10.1109/50.4134.

[72] R. Birch, D. Payne, M. Varnham, Fabrication of polarisation-maintaining fibres using gas-phase etching, *Electronics Letters* 18 (24) (1982) 1036–1038. doi:10.1049/el:19820709.

[73] Y. Sasaki, K. Okamoto, T. Hosaka, N. Shibata, Polarization-maintaining and absorption-reducing fibers, in: *Optical Fiber Communication*, OSA, Phoenix, Arizona, 1982, p. ThCC6. doi:10.1364/OFC.1982.ThCC6.

[74] S. Rashleigh, Origins and control of polarization effects in single-mode fibers, *Journal of Lightwave Technology* 1 (2) (1983) 312–331. doi:10.1109/JLT.1983.1072121.

[75] I. M. Bassett, Design principle for a circularly birefringent optical fiber, *Optics Letters* 13 (10) (1988) 844–846. doi:10.1364/OL.13.000844.

[76] D. Shanahan, Circularly birefringent optical fibres, Graduate Diploma in Science Thesis, University of Sydney (1993).

[77] D. B. Melrose and R. C. McPhedran, *Electromagnetic Processes in Dispersive Media*, Cambridge University Press, London, 1991.

[78] J. N. Ross, The rotation of the polarization in low birefringence monomode optical fibres due to geometric effects, *Optical and Quantum Electronics* 16 (5) (1984) 455–461. doi:10.1007/BF00619638.

[79] A. Barlow, D. Payne, Polarisation maintenance in circularly birefringent fibres, *Electronics Letters* 17 (11) (1981) 388–389. doi:10.1049/el:19810272.

[80] Y. Fujii, C. Hussey, Design considerations for circularly form-birefringent optical fibres, *IEE Proceedings J Optoelectronics* 133 (4) (1986) 249–255. doi:10.1049/ip-j.1986.0040.

[81] R. Castelli, F. Irrera, C. G. Someda, Circularly birefringent optical fibres: New proposals: Part I. Field analysis, *Optical and Quantum Electronics* 21 (1) (1989) 35–46. doi:10.1007/BF02199465.

[82] Max Born and Emil Wolf, *Principles of Optics*, sixth Edition, Pergamon Press, London, 1980.

[83] Okamoto K, Hosaka T, Edahiro T, Stress Analysis of Single Polarization Fibers, *Review of the Electrical Communication Laboratories* 31 (3) (1983) 381–392.

[84] A. Carter, Private communication, (1994).

[85] M. Varnham, D. Payne, J. Love, Fundamental limits to the transmission of linearly polarised light by birefringent optical fibres, *Electronics Letters* 20 (1) (1984) 55–56. doi:10.1049/el:19840038.

[86] A. L. Jones, Coupling of Optical Fibers and Scattering in Fibers, *Journal of the Optical Society of America* 55 (3) (1965) 261–271. doi:10.1364/JOSA.55.000261.

[87] A. W. Snyder, Coupled-Mode Theory for Optical Fibers, *Journal of the Optical Society of America* 62 (11) (1972) 1267–1277. doi:10.1364/JOSA.62.001267.

[88] A. W. Snyder, W. R. Young, Modes of optical waveguides, *Journal of the Optical Society of America* 68 (3) (1978) 297–309. doi:10.1364/JOSA.68.000297.

[89] A. Ankiewicz, A. Snyder, Xue-Heng Zheng, Coupling between parallel optical fiber cores–Critical examination, *Journal of Lightwave Technology* 4 (9) (1986) 1317–1323. doi:10.1109/JLT.1986.1074906.

[90] A. Tervonen, Analysis of symmetric directional couplers and asymmetric Mach-Zehnder interferometers as 1.30- and 1.55-um dual-wavelength demultiplexers/multiplexers, *Optical Engineering* 32 (9) (1993) 2083–2091. doi:10.1117/12.145072.

[91] A. Tervonen, P. Pöyhönen, S. Honkanen, M. Tahkokorpi, Integrated Optics 1·48/1·55 *M*m Wavelength Division Multiplexer for Optical Amplifier Application, *Journal of Modern Optics* 39 (8) (1992) 1615–1618. doi:10.1080/713823580.

[92] J. Arkwright, P. Chu, T. Tjugiarto, Variable demultiplexing using a twin-core fiber Mach-Zehnder interferometer, *IEEE Photonics Technology Letters* 5 (10) (1993) 1216–1218. doi:10.1109/68.248432.

[93] P. Coghill, Report on Twin-Core Fibre Project, Tech. rep., OFTC (October 1993).

[94] S. J. Hewlett and J. D. Love, Private Communication (November 1993).

[95] M. E. V. Valkenberg, *Analog Filter Design*, Holt-Saunders, New York, 1982.

[96] S. J. Hewlett and J. D. Love, Twin- and dissimilar-core fibre fabrication tolerances, Tech. rep., Optical Sciences Centre, ANU (March 1994).

[97] J. Love, A. Ankiewicz, Modal cutoffs in single- and few-mode fiber couplers, *Journal of Lightwave Technology* 3 (1) (1985) 100–110. doi:10.1109/JLT.1985.1074138.

[98] J. Arkwright, GIRD review 26/11/93, Tech. rep., Seimens Ltd. (November 1993).

[99] K. O. Hill, Y. Fujii, D. C. Johnson, B. S. Kawasaki, Photosensitivity in optical fiber waveguides: Application to reflection filter fabrication, *Applied Physics Letters* 32 (10) (1978) 647–649. doi:10.1063/1.89881.

[100] K. S. Chiang, R. A. Sammut, Iterative methods and stability of TE modes of nonlinear planar waveguides, *Optics Communications* 109 (1-2) (1994) 59–64. doi:10.1016/0030-4018(94)90738-2.

[101] G. I. Stegeman, E. M. Wright, All-optical waveguide switching, *Optical and Quantum Electronics* 22 (2) (1990) 95–122. doi:10.1007/BF02189947.

[102] A. W. Snyder, D. J. Mitchell, L. Poladian, F. Ladouceur, Self-induced optical fibers: Spatial solitary waves, *Optics Letters* 16 (1) (1991) 21–23. doi:10.1364/OL.16.000021.

[103] G. H. Derrick, Comments on Nonlinear Wave Equations as Models for Elementary Particles, *Journal of Mathematical Physics* 5 (9) (1964) 1252–1254. doi:10.1063/1.1704233.

[104] G. P. Agrawal, *Nonlinear Fiber Optics*, Academic Press, Boston, 1989.

[105] A. Boardman, P. Egan, S-polarized waves in a thin dielectric film asymmetrically bounded by optically nonlinear media, *IEEE Journal of Quantum Electronics* 21 (10) (1985) 1701–1713. doi:10.1109/JQE.1985.1072568.

[106] R. A. Sammut, Nonlinear planar waveguides with graded-index core: Power series solution, *Optical and Quantum Electronics* 26 (3) (1994) S301–S310. doi:10.1007/BF00384681.

[107] R. K. Varshney, M. A. Nehme, R. Srivastava, R. V. Ramaswamy, Guided waves in graded-index planar waveguides with nonlinear cover medium, *Applied Optics* 25 (21) (1986) 3899–3902. doi:10.1364/AO.25.003899.

[108] Q. Li, R. Sammut, C. Pask, Variational and finite element analyses of nonlinear strip optical waveguides, *Optics Communications* 94 (1-3) (1992) 37–43. doi:10.1016/0030-4018(92)90402-D.

[109] K. S. Chiang, Private communication, (1993).

[110] E. Yamashita (Ed.), *Analysis Methods for Electromagnetic Wave Problems*, The Artech House Microwave Library, Artech House, Boston, 1990.

[111] D. Marcuse, Solution of the vector wave equation for general dielectric waveguides by the Galerkin method, *IEEE Journal of Quantum Electronics* 28 (2) (1992) 459–465. doi:10.1109/3.123273.

[112] A. T. Galick, Efficient solution of large sparse eigenvalue problems in microelectronic simulation, in: *Proceedings of the Cornelius Lanczos International Centenary Conference*, Society for Indutrial and Applied Mathematics, 1994.

[113] RC. McPhedran, IM. Bassett, GW. Milton, KM. Lo, An electromagnetic theory of optical fibre with multiple embedded cylinders, in: *17th Australian Conference on Optical Fibre Technology (ACOFT-17 '92): Proceedings*, Institution of Radio and Electronics Engineers Australia, Edgecliff, NSW, 1992, pp. 388–391.

[114] W. A. Gambling, H. Matsumura, C. M. Ragdale, Wave propagation in a single-mode fibre with dip in the refractive index, *Optical and Quantum Electronics* 10 (4) (1978) 301–309. doi:10.1007/BF00620118.

[115] R. H. Stolen, Modes in fiber optical waveguides with ring index profiles, *Applied Optics* 14 (7) (1975) 1533–1537. doi:10.1364/AO.14.001533.

[116] W. Gambling, D. Payne, H. Matsumura, Effect of dip in the referctive index on the cut-off frequency of a single-mode fibre, *Electronics Letters* 13 (7) (1977) 174–175. doi:10.1049/el:19770128.

Appendix A

Derivation of First Order Vector Corrections

The derivation of Equation (4.31) is straightforward, if tedious. Equations (4.23) through (4.30) are substituted into the integrand in the numerator of equation (4.17). Each part is considered in turn below and terms of order Δ^2 are dropped.

$$\begin{aligned} & e^x_{\rightarrow}\left(h^x_{\uparrow}+y\frac{\partial h^y_{\uparrow}}{\partial x}-x\frac{\partial h^y_{\uparrow}}{\partial y}\right) \\ &= \left(e^{x;0}_{\rightarrow}+\Delta e^{x;1}_{\rightarrow}\right)\left[\left(h^{x;0}_{\uparrow}+\Delta h^{x;1}_{\uparrow}\right)+y\frac{\partial(\Delta h^{y;1}_{\uparrow})}{\partial x}-x\frac{\partial(\Delta h^{y;1}_{\uparrow})}{\partial y}\right] \\ &= e^{x;0}_{\rightarrow}h^{x;0}_{\uparrow}+\Delta\left[e^{x;1}_{\rightarrow}h^{x;0}_{\uparrow}+e^{x;0}_{\rightarrow}h^{x;1}_{\uparrow}+e^{x;0}_{\rightarrow}\left(y\frac{\partial h^{y;1}_{\uparrow}}{\partial x}-x\frac{\partial h^{y;1}_{\uparrow}}{\partial y}\right)\right] \end{aligned} \tag{A.1}$$

$$\begin{aligned} & e^y_{\rightarrow}\left(-h^y_{\uparrow}+y\frac{\partial h^x_{\uparrow}}{\partial x}-x\frac{\partial h^x_{\uparrow}}{\partial y}\right) \\ &= \Delta e^{y;1}_{\rightarrow}\left[-\Delta h^{y;1}_{\uparrow}+y\frac{\partial(h^{x;0}_{\uparrow}+\Delta h^{x;1}_{\uparrow})}{\partial x}-y\frac{\partial(h^{x;0}_{\uparrow}+\Delta h^{x;1}_{\uparrow})}{\partial y}\right] \\ &= \Delta e^{y;1}_{\rightarrow}\left(y\frac{\partial h^{x;0}_{\uparrow}}{\partial x}-x\frac{\partial h^{x;0}_{\uparrow}}{\partial y}\right) \end{aligned} \tag{A.2}$$

$$h^y_{\rightarrow}\left(-e^y_{\uparrow}+y\frac{\partial e^x_{\uparrow}}{\partial x}-x\frac{\partial e^x_{\uparrow}}{\partial y}\right)$$

$$
\begin{aligned}
&= \left(h_{\rightarrow}^{y;0} + \Delta h_{\rightarrow}^{y;1}\right)\left[-(e_{\uparrow}^{y;0} + \Delta e_{\uparrow}^{y;1}) + y\frac{\partial(\Delta e_{\uparrow}^{x;1})}{\partial x} - x\frac{\partial(\Delta e_{\uparrow}^{x;1})}{\partial y}\right] \\
&= -h_{\rightarrow}^{y;0}e_{\uparrow}^{y;0} + \Delta\left[-h_{\rightarrow}^{y1}e_{\uparrow}^{y;0} + h_{\rightarrow}^{y;0}e_{\uparrow}^{y;1} + h_{\rightarrow}^{y;0}\left(y\frac{\partial e_{\uparrow}^{x;1}}{\partial x} - x\frac{\partial e_{\uparrow}^{x;1}}{\partial y}\right)\right] \qquad \text{(A.3)}
\end{aligned}
$$

$$
\begin{aligned}
&h_{\rightarrow}^{x}\left(e_{\uparrow}^{x} + y\frac{\partial e_{\uparrow}^{y}}{\partial x} - x\frac{\partial e_{\uparrow}^{y}}{\partial y}\right) \\
&\quad = \Delta h_{\rightarrow}^{x;1}\left(\Delta e_{\uparrow}^{x;1} + y\frac{\partial(e_{\uparrow}^{y;0} + \Delta e_{\uparrow}^{y;1})}{\partial x} - x\frac{\partial(e_{\uparrow}^{y;0} + \Delta e_{\uparrow}^{y;1})}{\partial y}\right) \\
&\quad = \Delta h_{\rightarrow}^{x;1}\left(y\frac{\partial e_{\uparrow}^{y;0}}{\partial x} - x\frac{\partial e_{\uparrow}^{y;0}}{\partial y}\right) \qquad \text{(A.4)}
\end{aligned}
$$

Adding Equations (A.1) through (A.4) and grouping gives the desired result

$$
\text{Integrand} = e_{\rightarrow}^{x;0}h_{\uparrow}^{x;0} - e_{\uparrow}^{y;0}h_{\rightarrow}^{y;0} + \Delta q(x,y) \qquad \text{(A.5)}
$$

with $q(x,y)$ as given in Equation (4.32).

Appendix B

User Manual

B.1 Introduction

This manual describes the programs *drives* (the scalar solver), *drivev* (the vector solver) and related ancillary programs used for displaying and manipulating output files from the first two programs. The manual describes how to compile the programs, set up data files, write core description subroutines and postprocess the resulting output files. The majority of the programs are written in the C programming language which interface to FORTRAN library routines that perform the numerical computations. It is important to realise that both *drives* and *drivev* have been developed over a long period of time and so the code is not a pretty sight. Users modify the code at their own risk!

Both programs are intended to be run under some version of the UNIX[1] operating system. An ANSI C compiler is essential (the GNU C compiler is an excellent choice on most UNIX variants). The only real restriction is that you must have BCSlib-ext (which may be obtained from Boeing Computer Services, Seattle, Washington, USA). The programs have been successfully run under SunOS, AIX and UNICOS. A FORTRAN compiler is also necessary and some knowledge of the FORTRAN/C interface may be necessary if the program is being ported to a different architecture. In these cases it may be preferable to use *f2c* to convert the FORTRAN files to C instead of using the supplied (or perhaps non-existent) FORTRAN compiler(*f2c* is freely available by ftp from netlib.att.com:netlib/f2c).

The memory requirements are quite large. The scalar program requires around 50 Mbytes of memory and the vector program up to 200 Mbytes. Both programs rely heavily on the dynamic memory allocation facilities provided by C in order to keep memory usage to a manageable level.

This manual is divided into three major sections. The first deals with the scalar

[1] UNIX is a trademark of X/Open Ltd.

program, the second with the vector program and the third with various ancillary programs that are useful for output postprocessing and display.

In order to make this manual easier to read various font conventions are used. The names of computer programs are shown in *italic*, contents of computer programs are shown in `teletype` as are commands that a user would type into the computer. The user is assumed to have a basic knowledge of the UNIX operating system.

If the prospective user has serious difficulties the author may be reached by electronic mail to `glenn@physics.su.oz.au` to answer any queries.

B.2 Scalar Program

B.2.1 Description

The program *drives* is a computer code for solving the scalar wave equation,

$$(\nabla^2 + k^2 n^2)\psi = \beta^2 \psi, \tag{B.1}$$

in an optical fibre. The effective index and scalar field are provided as output and may be further processed by the user as required. The program produces an effective index from a user supplied free space wave number (or wavelength).

The user must write a subroutine that describes the refractive index distribution of the fibre being analysed and also provide a file containing various program control parameters.

The *drives* program is a finite difference code. The differential operator is discretized on a two dimensional square region giving rise to a large, sparse, generalised eigenvalue problem which is then solved using a shift-and-invert Lanczos scheme. The Lanczos solver is 'industrial strength'—direct sparse matrix techniques are used to solve the inhomogeneous systems that arise as part of the Lanczos iteration—and considerable memory savings are made by writing many arrays to disk. Consequently, it is possible to solve very large problems in reasonable amounts of time and memory.

The source code is for *drives* is subdivided into twelve C source files, three C header files and one FORTRAN source file. These are listed below together with a brief description of their contents.

- `calcri.c`—computes refractive index distribution.
- `driver.c`—the main program.
- `funcs.c`—computes the scaling functions.
- `gensubsid.c`—generates matrix elements.
- `invit.c`—eigensolver.
- `ioconv.c`—converts between 2-d arrays and 1-d arrays.
- `nrutil.c`—various modified routines from *Numerical Recipes*.
- `readdata.c`—reads the data file.
- `spline.c`—initializes cubic spline routine.
- `splint.c`—performs cubic spline interpolation.

- `transform.c`—carries out transformations to and from real space.
- `writeout.c`—output routines.
- `nrutil.h`—C prototype declarations for functions in nrutil.c
- `proto.h`—C prototype declarations for other functions.
- `sorp.h`—global variable declarations, global macro setup, etc.
- `inter.f`—interface to BCSlib-ext routines.

The user is referred to the comments in the individual source files for details.

A `Makefile` is provided to control the compilation process which will be discussed in more detail below. The files `calcri.c` and to a lesser extent `funcs.c` are problem dependent. The user must write a calcri function for every core profile examined. The file `funcs.c` must be altered if the scaling is changed from the tangent function provided in the distribution version of *drives*.

B.2.2 Compiling and Running *drives*

Compiling *drives*

Compilation of the *drives* program is controlled by a makefile. *Make* is a standard UNIX utility for maintaining, updating and regenerating related programs and files. A full description may be found in the UNIX manual page (`man make`). Typing `make` in the directory containing the *drives* source code should result in the construction of the *drives* executable.

A *Makefile* is conventionally divided into three sections: a definition section, a rule section and a dependency section. The definition section contains various compiler flags and library declarations. This section may be changed by the user. The rule and dependency section should not require any changes. The dependency section of the *drives Makefile* follows:

```
#
# Makefile for drives - solve field equations in an optical
# fibre in the weak guidance approximation
#

#CC=cc
CC=gcc
F77=f77
M=-DMEM=40
#G=-g
#OPT = -Ox -CSON
#OPT = -O4
OPT = -O2 -fomit-frame-pointer
OPTS = -DSPLINE_DATA
```

```
#GCCFLAGS= -finline-functions -fstrength-reduce -fkeep-inline-functions
CFLAGS=$(G) $(GCCFLAGS) $(OPT) $(OPTS) $(M)
LDFLAGS=$(G)
LIBS= -L/usr/physics/lib -lskit -lbcsext -lgcc
```

Anything following a # is treated as a comment.

The parameters shown above are quite straightforward. `CC` and `F77` are used to select the C compiler and FORTRAN compiler to use respectively. `M=-DMEM=num` is used to set the amount of (virtual) memory (in megabytes) to be used by the eigensolver. It should be made as large as possible but must not exceed the total memory of the machine on which `drives` is being *run* (as opposed to compiled). This last point is particularly important in a network environment. `G` is used to select compilation with the symbolic debugging option. `OPT` is used to select various C compiler optimization flags. Suitable flags may be found in your C compiler reference manual. `OPTS` allows the compile time choice of including code for performing cubic spline fitting to user supplied refractive index data (perhaps from a preform or fibre profiler; see Section 3). `GCCFLAGS` are special optimization flags for the GNU C compiler. `LDFLAGS` are linker control flags. `LIBS` is used to specify various extra libraries; `-lskit` specifies Saad's *Sparskit* library, `-libcsext` specifies the Boeing library, `-lgcc` specifies the GNU C support library and `-L/usr/physics/lib` specifies that the directory `/usr/physics/lib` be searched for libraries by the link editor. No optimization flags are specified for FORTRAN as the C interface stub modules do not require optimization.

All of the above mentioned parameters are at the user's discretion. In the *drives* distribution they are set for compilation on a Sun residing on the School of Physics network.

There are several reasons why the *drives* executable may not have been made. Many are system dependent and so beyond the scope of this document. The most likely 'simple' reason for compilation failure is the unavailability of the BCSlib-ext library on a particular machine. The School of Physics is Licenced to use the BCSlib-ext library on Sun's, IBM RS-6000's and on the CRAY YMP/EL and the library is available on all these platforms.

Running *drives*

The *drives* program is extremely simple to use once the requisite data file and core description subroutine have been written. The program takes no command line arguments and writes its output to the standard output stream (*stdout* in UNIX jargon—usually the terminal) by default. The output redirection operator > may be used to place the output of the *drives* run into a file on disk. So, `drives`

`> para` will send the output of the run to the file `para` in the current working directory.

Data file format

The *drives* program reads its per run parameters from a file called `data` in the current working directory. The format of the data file is shown below.

Title (string)
Number of grid points (integer)
X-scaling (real)
Y-scaling (real)
Approximation to eigenvalue (not used)
Wavelength (real)
Lower bound of effective index search interval (real)
Upper bound of effective index search interval (real)
Maximum number of eigenvalues to look for (integer)
Number of eigenvalue to output (integer)
File containing data for core 1 (string)
File containing data for core 2 (string)
Core separation (real)
Cladding index (real)
Core 1 radius multiplying factor (real)
Core 2 radius multiplying factor (real)
Core 1 delta multiplying factor (real)
Core 2 delta multiplying factor (real)

The *title* is a descriptive string of at most 80 characters that is passed through unchanged to the output. The *number of grid points* is used to set the order of discretization of the problem. Practical values range from 10 to 300 depending on the hardware. The larger the value the longer the run time and the greater the memory requirements. The *X-scaling* and *Y-scaling* parameters are used to adjust the nonlinear scaling functions. The numbers chosen are dependent on the core geometry and the actual scaling functions. Some experimentation with these parameters is usually required. The *approximation to eigenvalue* parameter is unused in the current implementation. The *wavelength* parameter is specified in microns and is used to set the operating wavelength of the fibre. The *lower bound of effective index search interval* and *upper bound of effective index search interval* set the left and right hand endpoints of the interval where the eigenvalue is expected to lie. The ability to search for eigenvalues only in a particular interval is especially useful since the effective index of a bound modes always lies between the cladding and core refractive indices. The *maximum number of eigenvalues*

to look for sets the number of eigenvalues to seek. In a twin core structure this would be set to 2—the even and odd supermodes. If more than the specified number of eigenvalues lie in the search interval then this parameter specifies the number of eigenvalues that will be output. The *number of eigenvalue to output* is used to select the eigenvalue and corresponding eigenvector that is output when more than one eigenvalue is being sought. The *file containing data for core 1* and *file containing data for core 2* are strings giving the names of files that contain experimental data representing the refractive index distribution of up to two cores (extension to a larger number of refractive index distributions is straightforward—see `readdata.c`). If the file name is `NULL`—note the CAPITALS—then no core data file is assumed to exist. This is useful when all analytic cores are being examined. The *core separation* in microns gives the distance between the two cores in a twin core fibre. The *cladding index* specifies the refractive index of the cladding. The *radius multiplying factors* are used to scale the splined cores to any particular radius. These parameters are useful because often the core radius of an experimentally measured core profile is set to 1. Similarly, the *core delta multiplying factors* are useful for scaling an experimentally core profile to any core-cladding refractive index difference. Note that if both filenames are `NULL` then the lines following them are ignored.

The contents of a typical `data` file are shown below. The text on the right is commentary and not part of the file.

```
Infinite Parabolic Profile      A suitable title
40                              Grid points
28.55993323                     X-scaling
28.55993323                     Y-scaling
2.2420676643                    Unused
0.55                            Wavelength (microns)
1.498                           Lower bound on ev search interval
1.500                           Upper bound on ev search interval
1                               Seek one eigenvalue
1                               And output the one eigenpair
NULL                            No external profile
NULL                            data is used
7.0                             Ignored in this case
1.44691753                      Ignored in this case
4.0                             Ignored in this case
4.0                             Ignored in this case
1.0                             Ignored in this case
1.0                             Ignored in this case
```

Output file format

A sample output file is shown below. The lines `Mesh size is` 40×40 and `Output` are always present. The former is used by the ancillary routines to determine array sizes and the latter to inform the ancillary programs where the eigenvector begins in the output file.

```
Infinite Parabolic Profile
```

```
Mesh size is 40 x 40
Number of rows = 1521
Number of non-zeros = 7449
Percentage of non-zeros = 0.321988%

alpha = 28.5599
beta = 28.5599
free space wavelength = 0.55 microns
free space wavenumber = 11.424x10^6 m^-1

...

 Effective index =  1.498764075625

Output
1 -3.949321945517e-15 0
2 2.553911789833e-13 0
3 -1.481110749609e-12 0
...

1519 -5.04633493526e-13 0
1520 -7.606340695426e-13 0
1521 -6.96488620621e-13 0
```

There are 39×39 output lines of the form:

```
integer real imaginary
```

It should be noted that the above example output has been trimmed extensively in order to save space in this manual. A full output file includes information relating to the eigensolver and other run-time diagnostics such as memory allocation, etc.

Specifying the core geometry—`calcri.c`

The file `calcri.c` is the heart of the *drives* program since it describes the core geometry and refractive index distribution of the optical fibre being analysed. The routine is written in C. However, only a very rudimentary knowledge of the C programming language is required in order to write new core description subroutines. Much of the file is common to all core descriptions. The lines preceding the comments should remain unchanged by the user. A typical `calcri.c` is shown below.

```
#include <stdio.h>
#include <math.h>
#include "sorp.h"
#include "nrutil.h"
#include "proto.h"

PUBLIC double *rho;
PUBLIC double *xi;
PUBLIC double **jacobian;
PUBLIC double wl;
PUBLIC int data_len;
PUBLIC double separation;
PUBLIC double multiplier01;
PUBLIC double multiplier02;

/*
** calcri(size): Compute refractive index profile.
**     Inputs:  size - rank of the matrix
**     Returns: nn - array containing the
**           (squared) refractive index * Jacobian
*/

#define N_0 2.25                                        <------
#define DELTA 1.e-4                                     <------

double **
calcri(int size)
{
    int i, j;
    double x_t, y_t;
    double **nn;
    double R;
    double free_k = 2*M_PI/wl;
    double RHO = 1.0;                                   <-------

    RHO *= free_k;                                      <-------
    RHO *= RHO;                                         <-------

    nn = dmatrix(1,size,1,size);

    for (i=2; i<size; i++)
        for (j=2; j<size; j++) {

/*
** It is easier to see whether the grid point is in the core if
** we go back to x,y - co-ordinates
*/

            sb_transform(&x_t,&y_t,rho[i],xi[j]);
```

```
            R = ((x_t*x_t)+(y_t*y_t))/RHO;          <-------

            nn[i][j] = N_0*(1-2*DELTA*R);           <-------

            nn[i][j] *= jacobian[i][j];
        }
    return(nn);
}
```

The lines marked <-------- must usually be changed for every refractive index profile. In particular, the format of the file when using a splined core is quite different. The reader is referred to the file `calcri.c.spline` for details. A concrete example of how to modify the *calcri* function is given below.

Suppose that a step index profile of radius 2μm, cladding index 1.457 and profile height 0.005 is required. Following the description above only the marked lines need to be changed. The double loop is shown in its entirety in order to make the code fragment more readable.

```
#define N_0 1.457                                   <------
#define DELTA 0.005                                 <------

    double RHO = 2.0;                               <-------

    RHO *= free_k;                                  <-------
    RHO *= RHO;                                     <-------

    for (i=2; i<size; i++)
        for (j=2; j<size; j++) {

/*
** It is easier to see whether the grid point is in the core if
** we go back to x,y - co-ordinates
*/

            sb_transform(&x_t,&y_t,rho[i],xi[j]);

            R = ((x_t*x_t)+(y_t*y_t));              <-------

            if (R <= RHO)
                nn[i][j] = N_0+DELTA;;              <-------
            else
                 nn[i][j] = N_0;

            nn[i][j] *= nn[i][j];

            nn[i][j] *= jacobian[i][j];
        }
```

Essentially, the code checks to see whether a point lies within 2μm of the origin and sets the refractive index accordingly.

Specifying the scaling functions—`funcs.c`

The non-linear scaling functions are set to the tangent function in the distribution. The `X-scaling` and `Y-scaling` parameters give some control over the amount of scaling but if the core differs radically from circular symmetry (e.g., an elliptical or multi-core fibre) then the tangent function is not acceptable. There is no requirement that the X- and Y-scaling functions have the same form.

The supplied `funcs.c` is shown below.

```
#include <math.h>
#include <values.h>
#include "sorp.h"

PUBLIC double alpha; /* X-scaling */
PUBLIC double beta;  /* Y-scaling */

/*
** funcx(x): Scaling function in X-direction
**     Inputs: x---argument at which function is to be evaluated (double)
**  Returns: function value at x (double)
*/

double
funcx(double x)
{
    return(alpha*tan(M_PI*x));
}

/*
** funcy(y): Scaling function in Y-direction
**     Inputs: y---argument at which function is to be evaluated (double)
**  Returns: function value at y (double)
*/

double
funcy(double y)
{
    return(beta*tan(M_PI*y));
}

/*
** dfuncx(x): Derivative of scaling function in X-direction
**     Inputs: x---argument at which function is to be evaluated (double)
**  Returns: derivative at x (double)
*/

double
dfuncx(double x)
{
    double tmp;

    tmp = cos(M_PI*x);
    tmp *= tmp;
```

```
    return(M_PI*alpha/tmp);
}

/*
** dfuncy(y): Derivative of scaling function in y-direction
**     Inputs: y---argument at which function is to be evaluated (double)
**  Returns: derivative at y (double)
*/

double
dfuncy(double y)
{
    double tmp;

    tmp = cos(M_PI*y);
    tmp *= tmp;
    return(M_PI*beta/tmp);
}
```

The variables `alpha` and `beta` are simply the values of the `X-scaling` and `Y-scaling` parameters from the `data` file.

If the scaling functions are changed then the derivative functions `dfuncx` and `dfuncy` must be changed appropriately.

B.3 Vector Program

B.3.1 Description

The program *drivev* is a computer code for solving the vector wave equation

$$\nabla^2\mathbf{E} - \nabla(\nabla\cdot\mathbf{E}) = -\omega^2\mu_0\varepsilon_0\bar{\varepsilon}_r\mathbf{E} \tag{B.2}$$

in an optical fibre. The reciprocal of the effective index and the electric field vector components (and optionally the magnetic field vector components) are provided as output and may be further processed by the user as required. The program produces the reciprocal of the effective index from a user supplied at a user supplied wavelength and initial guess at the modal effective index.

The user is required to write a subroutine that describes the (anisotropic) permittivity distribution of the fibre being analysed and also provide a file containing various program control parameters. There is an extensive range of command line arguments that may be used with *drivev* and these will be described fully below.

The *drivev* program is a finite difference code with three degrees of freedom per mesh point. The discretization is carried out in a similar manner to the scalar program and the resulting large, sparse, generalised eigenproblem is solved using Rayleigh quotient iteration (RQI). The inhomogeneous systems that arise at each step of RQI are explicitly solved by the program using a direct sparse (indefinite) matrix solver. The problem sizes are typically three times larger than in the scalar case so the fact that various arrays are written out to disk is even more important in the vector case. Practically, a 150×150 system can be solved on a SUN 4/690MP with 128 Mb of real memory and 512 Mb of swap space.

The vector program is arranged in twenty-five C source files, three C header files and one FORTRAN source file. A list appears below together with a brief description of the contents of the file.

- `calcperm.c`—compute permittivity tensor.
- `drive.c`—main program.
- `etime_.c`—provides missing etime and dtime FORTRAN subroutines.
- `funcs.c`—the transformation function.
- `gensubsid.c`—various ancillary routines.
- `h_field.c`—compute magnetic field.
- `invit.c`—eigensolver.

- `io.c`—input/output functions.
- `itoa.c`—provides missing integer-to-ascii function.
- `misc.c`—miscellaneous routines.
- `nrutil.c`—modified *Numerical Recipes* code.
- `smooth.c`—contains rarely used smoothing routines.
- `sort.c`—contains routines to sort matrix elements.
- `spline.c`—initializes cubic spline routine.
- `splint.c`—performs cubic spline interpolation.
- `term1.c`—compute matrix elements.
- `term2.c`—compute matrix elements.
- `term3.c`—compute matrix elements.
- `term4.c`—compute matrix elements.
- `term5.c`—compute matrix elements.
- `term6.c`—compute matrix elements.
- `term7.c`—compute matrix elements.
- `term8.c`—compute matrix elements.
- `term9.c`—compute matrix elements.
- `transform.c`—carries out transformations to and from real space.
- `nrutil.h`—C prototype declarations for functions in nrutil.c
- `proto.h`—C prototype declarations for other functions.
- `vp.h`—global variable declarations, global macro setup, etc.
- `inter.f`—interface to BCSlib routines.

The user is referred to the comments in the individual source files for details.

A `Makefile` is provided to automate the compilation process. The files `calcperm.c` and to a lesser extent `funcs.c` are problem dependent. A full discussion of `calcperm.c` is given below. The file `funcs.c` is identical to the scalar case and the reader is referred to section B.2.2 above.

B.3.2 Compiling and Running *drivev*

Compiling *drivev*

This section is concerned with the layout of the `Makefile` used for controlling compilation of the *drivev* program. More details on *make* and `Makefiles` may be found in section B.2.2 above.

The definition section of the `Makefile` for *drivev* is shown on the following page.

```
#
# Makefile for vector finite difference program
#

# GNU make uses FFLAGS AT&T make uses FCFLAGS
FFLAGS = $(FFLAGS) $(FCFLAGS) $(G) $(FOPT)
.f.o:
    $(F77) -c $(FFLAGS) $<

EXTRAS = -DTEST                     # just construct the operator
EXTRAS = -DNO_SCALE                 # no scaling
EXTRAS = -DPRINT_OP                 # print out the operator
EXTRAS = -DSMOOTH
EXTRAS = -DFULL                     # off diagonal permittivity
EXTRAS =
EXTRAS = -DMEMUSE -I/usr/physics/include       # memory debugging
EXTRAS = -DSPLINE_DATA -DSMOOTH -DQUIN

ELIB = -L/usr/physics/lib -lbcsext -lskit -lgcc

MALLOC_OBJ = -ldbmalloc
MALLOC_OBJ = /usr/lib/debug/malloc.o /usr/lib/debug/mallocmap.o
MALLOC_OBJ = /usr/physics/lib/gmalloc.o

CC = cc                             # MUST be ANSI
CC = gcc                            # GNU C
CC = acc                            # Sun ANSI compiler

F77 = xlf                           # AIX
F77 = f77                           # everyone else

G = -g                              # symbolic debugging
G =

COPT =
COPT = -O

FOPT =
FOPT = -O

CCFLAGS = -Q -Daix                  # AIX
CCFLAGS =                           # No options

CFLAGS = $(CCFLAGS) $(EXTRAS) $(G) $(COPT)

FPPFLAGS = -P -Wp,-eaj2478          # AIX; fpp
FPPFLAGS =                          # AIX; no fpp
```

```
FOLAGS = -Q -u                          # f77 (f2c) under AIX
FOLAGS = -u -qextname -qextchk          # AIX
FOLAGS = -u

FFLAGS = $(FOLAGS) $(G) $(FOPT) $(FPPFLAGS)

LOFLAGS = -s                            # strip symbol table
LOFLAGS = -Bstatic                      # load statically on SUN's
LOFLAGS =

LDFLAGS = $(LOFLAGS) $(G)

LIBS = -lf2c -lm                        # f2c on SUN
LIBS = -lmalloc                         # Better on some machines
LIBS =                                  # everything else

LINK = $(CC)                            # Genix, Ultrix, SUN with -Bstatic
LINK = $(F77)                           # everyone else
```

One of the nice features of `make` is that the last definition read is the one that is used. So in the cases above where multiple definitions for particular parameters are listed only the last one is used. Practically, this means that the order of the parameters can be changed to give different compiler or linker directives.

Simply typing `make` in the directory containing the *drivev* source files will result in the `drivev` executable being built. The main reason for compilation failure is described in Section B.2.2.

Running *drivev*

The *drivev* program takes several command line arguments. A UNIX style synopsis is:

```
drive [-o outfile] [-m memory] [-p polarisation] [-M] [-l] [-s]
```

The arguments in square brackets are optional. The above line of output is obtainable from the drive program by typing `drive -
? ` if using the C shell or `drive -?` if using the Bourne shell will reproduce the synopsis line above.

The command line parameters are used to select runtime behaviour of the *drivev* program.

The `-o` option is used to select the root of the output file name. The remainder of the file name is constructed from the `mesh size` parameter in the data file. For example if the `mesh size` parameter is set to 40 then the command `drivev -o outf` would result in the output being placed in the file `outf.040`. If the `mesh size` parameter is greater than 100 no leading zero is appended to the extension. If the `-o` option is omitted then output is sent to standard output and may be redirected using the > operator. The `-m` option is used to select the amount of memory used by the sparse linear equation solver in megabytes. The default value is 24 Mb. The `-p` option is used to select the field polarisation to calculate. The choices for `polarisation` are `x` and `y`. The default value is `x`. The `-M` option instructs the program to compute the magnetic field vectors as well as the usual electric field vectors. This option only has an effect if the `-o` flag has also been chosen. When this flag is in effect an additional output file is created with its name constructed from the root with the letter 'm' appended followed by the extension constructed using the rule

given above. The `-l` option is used to select the Lanczos algorithm instead of RQI. The `-s` option is used to select code that uses symmetry to separate the polarisation degenerate modes of the fibre being analysed.

Data file format

The *drivev* program reads many of its per run parameters from a file called `data` in the current working directory. The format of the data file is shown below.

Title (string)
Maximum number of RQI steps (integer)
Number of grid points (integer)
X-scaling (real)
Y-scaling (real)
Initial guess at eigenvalue (real)
Epsilon (unused)
Wavelength (real)
Effective index (real)
Data file for core (string)
Multiplier (real)

The parameters have the same meaning as for the *drives* except as noted in the following. The user is required to supply an `Initial guess at eigenvalue` in order to seed the RQI method. The `Effective index` must be supplied and is used in conjunction with the `Wavelength` parameter to compute β which is used as the length scaling parameter.

The contents of a typical `data` file are shown below. The text on the right is commentary and not part of the file.

```
Infinite Parabolic Profile       A suitable title
40                               Grid points
28.55993323                      X-scaling
28.55993323                      Y-scaling
0.445                            Initial eigenvalue guess
1e-7                             Unused
0.55                             Wavelength (microns)
1.4824                           Effective index
NULL                             No external profile data is used
7.0                              Ignored in this case
```

Specifying the permittivity—`calcperm.c`

The file `calcperm.c` is used to specify the permittivity tensor and core geometry of the fibre being analysed and is analogous to the routine *calcri* used in the

scalar case. The routine is written in C. However, only a few lines need to be changed when defining a new problem. The lines preceding the comments should remain unchanged by the user. A typical `calcperm.c` is shown below.

```
#include <stdio.h>
#include <stdlib.h>
#include <math.h>
#if defined(UNDERSTANDS)
#include <values.h>
#endif
#include "vp.h"
#include "proto.h"
#include "nrutil.h"

dcomplex **eps11;
dcomplex **eps22;
dcomplex **eps33;
dcomplex **eps12; /* == transpose(eps21) */

sparset *epsilon;

/*
** calcperm - compute the permittivity tensor
**
** Input: size
** Returns: none
**
** The permittivity is available in the arrays eps[1-2][1-2]
*/

#define N_0 2.25                                        <------
#define DELTA 1.e-4                                     <------

void
calcperm(size)
int size;
{
    int i,j;
    double x_t, y_t;
    double R;
    int t;
    int cnt1 = 0;
    double free_k = 2*M_PI/wl;
    double Beta = neff*free_k;
    double RHO = 1.0;                                   <------

    RHO *= Beta;

    fprintf(stderr, "calcperm called\n");
```

```
    eps11 = zmatrix(0,size+1,0,size+1);
    eps22 = zmatrix(0,size+1,0,size+1);
    eps33 = zmatrix(0,size+1,0,size+1);
    eps12 = zmatrix(0,size+1,0,size+1);

    epsilon = (sparset *)calloc(8*size*size+3, sizeof(sparset));

    for (i=1; i<=size; i++)
        for (j=1; j<=size; j++) {
            sb_transform(&x_t, &y_t, rho[i], xi[j]);

            R = ((x_t*x_t)+(y_t*y_t))/(RHO*RHO);    <------

            eps11[i][j].r = N_0*(1-2*DELTA*R);      <------
/*
** Multiply by the jacobian
*/
            eps11[i][j].r *= jacobian[i][j];        <------
            eps33[i][j] = eps11[i][j];              <------
            eps22[i][j] = eps11[i][j];              <------
#ifdef FULL
            eps12[i][j].r *= eps12[i][j].r;
#endif

            t = i + (size - j) * size;

            cnt1++;
            epsilon[cnt1].row = t;
            epsilon[cnt1].col = t;
            epsilon[cnt1].val = eps11[i][j];

#ifdef FULL
            cnt1++;
            epsilon[cnt1].row = t;
            epsilon[cnt1].col = t+(size*size);
            epsilon[cnt1].val = eps12[i][j];

            cnt1++;
            epsilon[cnt1].row = t+(size*size);
            epsilon[cnt1].col = t;
            epsilon[cnt1].val = eps12[i][j];
#endif

            cnt1++;
            epsilon[cnt1].row = t+(size*size);
            epsilon[cnt1].col = t+(size*size);
            epsilon[cnt1].val = eps22[i][j];
```

```
            cnt1++;
            epsilon[cnt1].row = t+(2*size*size);
            epsilon[cnt1].col = t+(2*size*size);
            epsilon[cnt1].val = eps33[i][j];
        }

        sort_eps(epsilon,cnt1);

    free_zmatrix(eps11,0,size+1,0,size+1);
    free_zmatrix(eps22,0,size+1,0,size+1);
    free_zmatrix(eps33,0,size+1,0,size+1);
    free_zmatrix(eps12,0,size+1,0,size+1);

    return;
}
```

The lines marked <------ must usually be changed for each new permittivity profile. An example of such changes is given below for the same core geometry as in the example in Section B.2.2, *viz.* a step profile of radius 2μm, cladding index 1.457 and profile height 0.005.

```
#define N_0 2.25                                          <------
#define DELTA 1.e-4                                       <------

    double RHO = 1.2;                                     <------

    for (i=1; i<=size; i++)
        for (j=1; j<=size; j++) {
            sb_transform(&x_t, &y_t, rho[i], xi[j]);

            R = ((x_t*x_t)+(y_t*y_t));                    <------

            if (R <= RHO)                                 <------
               eps11[i][j].r = N_0 + DELTA;               <------
            else                                          <------
               eps11[i][j].r = N_0;                       <------

            eps11[i][j].r *= eps11[i][j].r;               <------

            eps33[i][j] = eps11[i][j];                    <------
            eps22[i][j] = eps11[i][j];                    <------
```

The beginning of the main loop is shown for clarity.

The example given is for an isotropic permittivity distribution in which case `eps12` and `eps21` are zero (this is taken care of by zmatrix). In the more general case of an anisotropic distribution `eps11 != eps22 != eps33` and `eps12 == eps21` would have to be assigned values.

B.4 Ancillary Programs

In addition to *drives* and *drivev* three output postprocessing programs are provided including an output 'pretty' printer and a program for processing output from the York Technologies P102 preform profiler. Both plotting programs are based on the plplot library available from the University of Texas.

B.4.1 Plotting programs

There are two plotting programs available; *pl*, a surface plotter and *cpl*, a contour plotter. Both are able to plot arbitrary data provided it is on a regular square grid. The format of a file that can be plotted is identical to the output format of *drives* and *drivev* programs, *viz*,

> arbitrary number of lines
> ...
> **Mesh size is** $n \times n$
> ...
> arbitrary number of lines
> ...
> **Output**
> integer real real
> ...
> **At least** $(n-1) \times (n-1)$ **lines of data**
> **and at most** $3 \times (n-1) \times (n-1)$ **lines of data**.
> ...

The synopsis for *pl* is

```
pl [-f file] [-A [-2]] [-x] [-y] [-z] [-P] [-n] [-i]
[-1] [-a az] [-e el] [file].
```

The options have the following meanings. The `-f` option is used to set the file from which the data is read. If this option is omitted then *pl* expects the name of a data file to be the last item on the command line. The `-A` option specifies that all vector components and the intensity are to be shown on the one plot. The suboption `-2` which must occur with the `-A` option specifies that only two plots are to appear per page. The `-x`, `-y` and `-z` option are used to select which vector component to plot. The `-i` option specifies that the intensity be plotted. The `-n` option specifies that all values comprising the plot be multiplied by -1 (the eigenvalue is only specified up to sign). The `-1` option specifies that field components be normalized to have maximum value unity. The `-a` and `-e` options are used to select the azimuth and elevation of the viewpoint respectively.

The *cpl* program has the following synopsis.

```
cpl [-f file] [-A] [-n] [-x] [-y] [-z] [-P] [-l lev] [file]
```

The options have the same meaning as for *pl*. The unique options `-P` and `-l` are used to change the page orientation to portrait and to set the number of contour levels respectively.

The default behaviour of both programs is to plot the x-component in the case of a vector computation and the scalar field in the case of a scalar computation.

When either program is run with valid options (invalid options elicit a usage message) then the following menu appears allowing the user to select a plot device.

```
Plotting Options:
 < 1> (xwin)     X-Window Screen (Xlib)
 < 2> (xterm)    Xterm Window
 < 3> (tekt)     Tektronix Terminal
 < 4> (dg300)    DG300 Terminal
 < 5> (plmeta)   PLPLOT Native Meta-File
 < 6> (tekf)     Tektronix File
 < 7> (ps)       PostScript File
 < 8> (xfig)     Xfig file
 < 9> (ljii)     LaserJet II Bitmap File (150 dpi)
 <10> (hp7470)   HP 7470 Plotter File (HPGL Cartridge, Small Plotter)
 <11> (hp7580)   HP 7580 Plotter File (Large Plotter)
 <12> (imp)      Impress File
 <13> (null)     Null device

Enter device number or keyword:
```

B.4.2 Processing preform profiler data

The program *york* is used to extract and plot data from the P102 preform profiler. The program is based on a FORTRAN program by K. M. Lo but has been greatly extended. The format of the preform profiler output file is described in the 'P102 Preform Profiler Operator's Manual'.

The synopsis for *york* is

```
york [-n num] [-o outfile] [-i infile] [-p].
```

The program automatically detects polar and Cartesian format data files.

The `-n` option is used to select the projection to extract if the file being processed is in polar format. This flag is silently ignored in the case of Cartesian data. If this flag is omitted and polar data is detected then the first slice will be extracted. The `-o` flag is used to set the name of the file where the extracted data will be written. The default is to write the data to standard output. The `-i` flag is used to set the name of the file containing the raw data from the preform profiler. The default is to read from standard input. The `-p` flag is used to obtain a 2-d

plot of a Cartesian format data file. This option is silently ignored in the case of a polar format data file.

When *york* is run some useful information is printed to the screen (actually the standard error stream). An example is shown below.

```
Processing polar data
P1237aP
Measured on Mon Nov  8 14:38:28 1993

TACKED TCF SIMILAR CORE
Measurement step was 5 microns over 14 mm
Integration ratio = .5
```

The main purpose of the *york* program is to extract preform profiler data for subsequent use as input to *drives* or *drivev*.

B.4.3 Extrapolating

The program *extrap* is used to carry out a Richardson style extrapolation on the eigenvalues collected from a sequence of *drives* or *drivev* runs on the same core profile but at different mesh sizes. The extrapolation process will only work if the refractive index profile is smooth (results from preform profile data are not recommended). The synopsis for *extrap* is

```
extrap filename
```

The output is written to standard output. The input file for *extrap* has the following form.

number of lines
mesh eigenvalue
...
mesh eigenvalue

A typical input file is shown below.

```
4
90 0.46957799413724
100 0.46957919821504
110 0.46958008381053
120 0.46958075410745
```

These data are collected manually from the output files produced by *drives* or *drivev* using the UNIX utility *grep* and a suitable text editor.

The output from the *extrap* program for the above input is shown below.

```
Extrap output created on Mon Jan 17 09:52:51 1994

Triple core x-polarisation fundamental mode

Number of data items: 4
90 0.469577994137239995708910
100 0.469579198215040016783917
110 0.469580083810530013455065
120 0.469580754107449982459599

90 100 0.469590034915240317481278
100 110 0.469588939765430535278057
110 120 0.469588127373569363953720

90 110 0.469584011591286543119139
100 120 0.469584065414263562843189

90 120 0.469584226883194566504187

Extrapolated eigenvalue is 0.469584226883194566504187
```

The program *tabtex* is a pretty printer for the output of the *extrap* program. The output of the *tabtex* is designed to be included in a LaTeX document. The output of the *tabtex* program when used to process the data above is shown below.

```
\begin{table}[htb]
\begin{center}
\begin{tabular}{ccccc} \hline
{\sc N} &\multicolumn{4}{l}{\hskip4.5ex$B^2$} \\ \hline
 90 & {\tabf 0.46957799413} & &  &   \\
 &  &  {\tabf 0.46959003491} & &   \\
 100 & {\tabf 0.46957919821} & &  {\tabf 0.46958401159} &  \\
 &  &  {\tabf 0.46958893976} & &  {\tabf 0.46958422688}   \\
 110 & {\tabf 0.46958008381} & &  {\tabf 0.46958406541} &  \\
 &  &  {\tabf 0.46958812737} & &   \\
 120 & {\tabf 0.46958075410} & &  &   \\ \hline
\end{tabular}
\caption{Triple core x-polarisation fundamental mode}
\label{tbl:ADD A LABEL}
\end{center}
\end{table}
```

The LaTeX document must include a definition for the `tabf` font.